

Příloha I:

EBERLOVA, Lada, Vaclav LISKA, Hynek MIRKA, Zbynek TONAR, Stanislav HAVIAR, Milos SVOBODA, Jan BENES, Richard PALEK, Michal EMINGR, Jachym ROSENDORF, Patrik **MIK**, Sarah LEUPEN a Alois LAMETSCHWANDTNER, 2017. The use of porcine corrosion casts for teaching human anatomy. *Annals of Anatomy - Anatomischer Anzeiger* [online]. 213, 69–77. ISSN 0940-9602. Dostupné z: doi:10.1016/j.aanat.2017.05.005. **IF₂₀₁₆=1,864, Q1**(Anatomy & Morphology).



ELSEVIER

Contents lists available at ScienceDirect

Annals of Anatomy

journal homepage: www.elsevier.com/locate/aanat



The use of porcine corrosion casts for teaching human anatomy*

Lada Eberlova^{a, b, *}, Vaclav Liskov^{b, c}, Hynek Mirkov^{b, d}, Zbynek Tonar^{b, e}, Stanislav Haviar^f,
Milos Svobodag^g, Jan Benes^g, Richard Palek^{b, c}, Michal Eminger^{b, c}, Jachym Rosendof^{b, c},
Patrik Mik^h, Sarah Leupen^h, Alois Lametschwandtnerⁱ

^a Department of Anatomy, Faculty of Medicine in Pilsen, Charles University, Karlovska 48, 301 66 Pilsen, Czech Republic

^b Biomedical Center, Faculty of Medicine in Pilsen, Charles University, Alej Svobody 76, 12300 A Pilsen, Czech Republic

^c Department of Surgery, University Hospital in Pilsen, Alej Svobody 8, 301 60 Pilsen, Czech Republic

^d Department of Imaging Methods, University Hospital in Pilsen, Alej Svobody 80, 30460 A Pilsen, Czech Republic

^e Department of Histology and Embryology, Faculty of Medicine in Pilsen, Charles University, Karlovska 48, 301 66 Pilsen, Czech Republic

^f Department of Physics and NTJS-European Centre of Excellence, Faculty of Applied Sciences, University of West Bohemia, Univerzity 8, 30614 Pilsen, Czech Republic

^g New Technologies-Research Centre, University of West Bohemia, Univerzity 8, 306 14 Pilsen, Czech Republic

^h Department of Biomedical Science, University of Maryland Baltimore County, 1000 Hilltop Circle, Baltimore, MD 11250, USA

ⁱ Department of Cell Biology and Physiology, University Salzburg, Hellbrunner Str. 34, A-5020 Salzburg, Austria

ARTICLE INFO

Article history:

Received 22 December 2016

Received in revised form 14 April 2017

Accepted 4 May 2017

Keywords:

Corrosion casting

Anatomy

Biodur E20 Plus

Microcomputed tomography

Pig

ABSTRACT

Integrating and learning human anatomy, anatomical autopsy and prosected specimens have always been indispensable. However, alternative methods must often be used to demonstrate particularly delicate structures. Corrosion casting of porcine organs with Biodur E20 Plus is valuable for teaching and learning both gross anatomy and, uniquely, the micromorphology of cardiovascular, respiratory, digestive, and urogenital systems. Assessments of casts with stereomicroscope and/or scanning electron microscope as well as highlighting cast structures using color coding help students to better understand how the structures that they have observed as two-dimensional images actually exist in three dimensions and students found using the casts to be highly effective in their learning. Reconstructions of a stoma structures from (micro)-computed tomography scans and videos facilitate detailed analyses of branching patterns and spatial arrangements in cast structures, aid in the understanding of clinically relevant structures and provide innovative visual aids. The casting protocol and teaching manual we offer can be adjusted to different technical capabilities and might also be found useful for veterinary or other biological science classes.

© 2017 Elsevier GmbH. All rights reserved.

1. Introduction

Corrosion casting is an established method for the visualization of the morphology of hollow structures. It is based on the filling of the cavity with solidifying material, after which the surrounding tissue is removed with use of a corrosion agent after its polymerization. Although the first attempts are often attributed to Leonardo da Vinci (Hermiz et al., 2011; OeSordi et al., 2014), who filled the ox brain ventricles with wax and scraped off the overlying tissue between 1504 and 1507 (Paluzzi et al., 2009), casting was per-

formed earlier and can be divided into the "pre-corrosion" and "corrosion" periods (Aharinejad and Lametschwandtner, 1992a). The oldest recorded attempts to fill the human blood vessels date back to 14th century and Alessandra Giliani (1307–1326), the first woman anatomist and prosector, professor of medicine at the University of Bologna. Giliani developed a technique to make blood vessels visible by filling them with colored, hardening liquids. However, the first notes of injection of a solidifying material followed by parenchymal corrosion were recorded by Dutch anatomist Govert Bidloo (1649–1713), the author of the anatomical atlas *Anatomia Humani Corporis*, who used melted metal to inject trachea and bronchi and boiled the specimen to remove connective tissues (Davies, 1973). Since then, casting materials and procedures have been gradually improved. At present, the casting media available which are suitable for corrosion range from low-viscosity, hard and brittle materials, such as methyl methacrylates, to pliable the r-

* Abbreviations: CC, corrosion; st, standard deviation.

This paper belongs to the special issue Medical Education 2018.

Corresponding author at: Department of Anatomy, Faculty of Medicine in Pilsen, Charles University, Karlovska 48, 301 66 Pilsen, Czech Republic.

E-mail address: la.da.eberlova@lfp.cun.ia. (L. Eberlova).

Tú l < t

Resin suitable for corrosion casting.

Group	Resin	Citation	Miaowssel permeability	Radio pacity	Official price per liter
Acrylic resins	Mercox 0-28	Lametschwandtner <i>et al.</i> (2004)	Yes	Yes	Out of product
	Mercoxi kit	Eberlova <i>et al.</i> (2015)	Yes	Yes	<n/n
	Bacson's #17 kit	Oebbaudet <i>et al.</i> (2014)	Yes	Yes	€ 329
Epoxyresins	Biodur E2d Plus	Eberlova <i>et al.</i> (2015)	Yes	Yes	€ 40
Polyurethanes	Souda-foam*	OeSordiet <i>et al.</i> (2014)	No	Yes	€ 20
	Polyurethane Elastomer (PU4ii) kit	Twt'fves <i>et al.</i> (2012)	No	Yes	€ 954

* AsOTI April, 2017.

mostable polyurethane or epoxy resins to flexible silicone rubber (Haenssger *et al.*, 2014: Table 1). Each of the agents has its pros and cons, and choosing the optimal one is always a balance between the research purpose and the specimen quality. For example, for the high volume vascular corrosion cast resin with a sufficient processing time must be chosen. And if we intend to examine the cast with the use of X-ray, the resin must be also radiopaque.

Since the 1960s, corrosion casts have been studied using light microscopy.

Nowell and Tyler (1971) and Murakami (1971) first applied scanning electron microscopy (SEM) in CC assessment. With recent advances in high-resolution computed tomography (CT) technology, a pixel resolution close to 1 µm allows for morphometry of microvessels comparable with classical light microscopy. CT scanning provides new data from the microvascular tree that can be used both for the mathematical modeling (Debbaut *et al.*, 2014) or quantitative purposes (Jiríček *et al.* 2016).

CCs enable the study of three-dimensional (3-D) arrangement of (micro)vascular systems, including angiogenesis (Gerlach *et al.* 2014). In combination with SEM, vascular CCs provide information about structures that protrude from the wall and cause imprints, e.g., the endothelial cell nuclei, valves, and constrictions. These replicates help to differentiate arterial from venous vessels and to identify different parts of the vascular bed (Lametschwandtner *et al.* 1990; Aharinejad and Lametschwandtner, 1992). Human vascular CCs are usually not suitable for ultrastructural studies and need to be substituted by other mammals (Cope, 2008; Hermiz *et al.*, 2011) as the fully filled corrosion cast requires a fresh heparinized specimen, irrigated vasculature and surgery preventing gas embolization.

Our goal at the very beginning was purely scientific- we needed to obtain three-dimensional data of human liver microvasculature for mathematical modeling of the blood perfusion. Due to ethical concerns and the practical impossibility of obtaining fresh and healthy human livers, we focused on the use of porcine livers. Given its size, morphology and function, the porcine liver is frequently used as a large-animal liver model, e.g., for testing surgical techniques (Bedoya *et al.* 2014), liver transplantation (Okada *et al.*, 2015), regeneration (Mortensen and Revhaug, 2011; Avritscher *et al.* 2013), mathematical modeling (Fuand Chui, 2014), gene therapy (Carreño *et al.*, 2013) and pharmacology (Gnutzmann *et al.*, 2015). After testing different resins, we optimized the protocol of hepatectomy and high-volume corrosion casting with Biodur E20 Plus (Eberlova *et al.*, 2015). Of all resins tested, Biodur E20, Plus (Biodur products, Heidelberg, Germany) exhibited the

best handling qualities: it passes with minimal leakage through

the capillaries, its processing time enables high volume filling, it is slightly flexible and alcohol resistant after hardening, and it is radio-opaque. Because of the high quality and high teaching potential of the resulting preparations as well as easy organ accessibility- pigs are bred in our biomedical center and are sacrificed for a variety of research topics- we decided to prepare other parenchymal organs that otherwise would be wasted for use in

The aims of our study were (1) to evaluate the suitability of Biodur E20 Plus for corrosion casts for teaching human anatomy; (2) to enhance students' understanding of macro- and microvascular structures of clinical relevance; (3) to interconnect the macro- with the microanatomy with cast assessment by light microscopy and scanning electron microscopy; (4) to create original, innovative visual aids useful for lectures and projections.

2. Methods and results

The experimental surgical and anesthesia procedures and the use of piglets in this study were certified by the Commission for Work with Experimental Animals at the Pišens Medical Faculty of Charles University, Prague, and were under the control of the Ministry of Agriculture of the Czech Republic. All procedures were prepared and performed under the law of the Czech Republic, which is compatible with the legislation of the European Union.

2.1. Surgery

The detailed protocols for surgery and casting were published by Eberlova *et al.* (2015). Briefly, healthy Prestice Black-Pied pigs (Vrtková, 2015), N=7, age 16-18 weeks, weight 35-45 kg, both sexes, were premedicated, and intravenous anesthesia was administered continuously. For organ casts, see Table 2. After myorelaxation, the pigs were intubated and mechanically ventilated. Heparin (30,000 UI i.v.) and volume-substituting infusions were administered. Before hepatectomy, the vascular bed of the liver was flushed with SL of heparinized (10,000 U.) Hartmann's solution administered via a tube inserted into the suprahepatic portion of the caudal caval vein. Then, the organ under consideration was disconnected from blood circulation and the vascular tree of liver, kidney and/or spleen was flushed with heparinized solution (dilution 10,000 UI of heparin per 1 L of cold Hartmann's solution) via the suprahepatic portion of the inferior caval vein (liver), renal arteries (kidney) or splenic artery (spleen). The hepatic portal vein (PV) and hepatic artery (HA) or renal veins or splenic vein remained unligated to drain the perfused solution. The bronchial tree was harvested together with the lungs.

2.2. Casting procedure

All vessels were cannulated while submerged in water to prevent aspiration of air into vessels. Biodur E20 (Biodur Products, Heidelberg, Germany) for injection was mixed at a ratio of 100g

Biodur E20 Plus/45g of catalyst E2(0). The PV was filled using

teaching anatomy.

manual injection pressure. For injecting the hepatic, splenic and renal arteries, the cannula was held and guided by a micromanipulator (Aharinejad and Lametschwandtner, 1992b). After filling, specimens were submerged in tap water (20°C; 24 h). For hardening, they were transferred to 15% potassium hydroxide for tissue removal (40°C; 2-3 days), rinsed in tap water, and either stored in 70% denatured alcohol, or, for higher resolution imaging, frozen in distilled water to be subsequently cut into 1 cm³ ice cubes with a belt saw.

Table 1

Porcine organ sets with Biodur E2d Plus.

Organ	Method of filling	Volume of Biodur E2d Plus
Liver (H+2)	Porta! vein (MP)	500 ml
Liver (H+2)	Porta! vein (M,P) hepatic artery (MMP)	500 ml. 150 ml
Liver (H+2)	Porta! vein (M,P) hepatic artery (MMP). bile duct: (MP)	500 ml. 150 ml. 70 ml
Spleen (N+2)	Splenic artery (MMP)	180 ml
Spleen (N+2)	Splenic artery (MMP). splenic vein (MMP)	180 ml. 70 ml
Kidney (N+4)	Abdominal aorta (MP)	300 ml
Kidney (N+2)	renal artery (MMP). renal vein (MMP)	130 ml. 70 ml
Kidney (N+2)	renal artery (MMP). ureter (MP)	130 ml. 70 ml
Bronchial tree (N+2)	Trachea (MP)	800 ml

MP- manual pressure; MMP- micromanipulator; total number of animals, N=7 (different combinations of organs recorded individually half of the total).

2.3. Casting and data processing

Although even the gross CC can be very educational (Fig. 1) - the students can see the nature and density of the vasculature even with the naked eye - various devices can be used to see the details of the vascular tree. The liver CC, owing to its size, can be examined with the common multi-slice human CT scanner (Fig. 2A), and any cast can be examined with a stereomicroscope (Fig. 3(D)).

To provide the students morphological details in ascending resolution, our casts were analyzed first with the stereomicroscope (Olympus 5ZX7; Tokyo, Japan). Liver casts were then scanned in 90% dehydrated alcohol (provides higher contrast than water) with a multi-slice human CT scanner (Somatom Sensation64, Siemens, Forchheim, Germany; slice thickness: 0.6 mm; voxel size: 4 x 0.4 x 0.6 mm). For high-resolution imaging, a lobe (liver) or lobule (bronchial tree) was dissected, whereas whole kidneys or spleens were frozen in distilled water and randomly cut with a belt saw into pieces (size - 1 cm). Indomylchosen prisms were then immersed in 5% formic acid for 5 min (Lametschwandtner et al., 1990) rinsed in distilled water, air dried, mounted, sputter coated with gold (1 min) and examined using the scanning electron microscope in a Stereoscan 250 instrument (Cambridge, UK) at 10 kV or in a SU-70 (Hitachi, Japan) at 1 kV accelerating voltage (Figs. 4, SB).

Liver, spleen, kidney and Jung casts were scanned in air with a μ -CT scanner (Xradia μ -XCT400, Pleasanton, CA, USA). Samples were first scanned using the Macrodetector (pixel size: 47 μ m/px. 1024 x 1024 px resolution) to display the overall liver cast structure. Then, the most interesting parts were scanned again with a high-resolution detector using the following parameters: source voltage 40 kV, source power 4W, pixel size 4.1 μ m, detector resolution 1024 x 1024 pixels (binning 2), rotation angle 360°, number of images 1500, overall scanning time 3 h, and temperature 28°C. After scanning, recorded images were used for 3-D reconstruction using specialized software supplied with the Xradia machine. Then, reconstruction scans were filtered and semi-automatically segmented using the software Avizo 7.2 (vsg) and FIJI Image 1.50f (National Institutes of Health, USA). Salt-and-pepper noise was removed by filtering. Image segmentation was performed by thresholding and manually controlled flooding. Skeletonization was used to extract topological information (Fig. 28, D).

For the 3-D reconstructions and brief data processing, the data from μ -CT scanner can be used for the volume rendering technique and thin-slab maximum intensity projection, software commonly available in human CT scanners (Fig. 2).

2.4. Use of corrosion casting in elective anatomical classes - the schedule

Basic knowledge of general anatomy and histology were prerequisites to be accepted for elective anatomical classes. The schedule for the second-year medical students (Table 3) is outlined below: Week 1: In collaboration with surgeons, the instructors obtain

a fresh organ that is immediately cannulated and injected with resin as described in the Materials and Methods. Students only watch this procedure, which is performed by an instructor, and wear protective glasses. The room is ventilated to prevent exposing students and staff to toxic fumes. The injected organ is left submerged in tap water for approximately 24 h at 20°C for hardening. In the next 3 days, the organ is macerated (corroded) and rinsed in running tap water. Week 2: Students inspect casts with the stereomicroscope and select the part of the cast they want to analyze in the SEM. This part is frozen in distilled water and cut into - 1 cm³ ice cubes. Ice cubes are allowed to thaw in distilled water and casts are cleaned from any debris under binocular control (Lametschwandtner et al., 1990). Clean casts are then placed onto filter paper and air dried. Week 3: Students are introduced to theoretical principles of SEM and prepare specimens for SEM observation; i.e., mounting of dry casts on to specimen stubs and sputter coating specimens with gold. Finally, students together with the instructor watch images of selected areas of vascular casts on the SEM display and discuss the displayed structures in terms of cast quality, vascular patterns, normal versus pathological, and true structure versus artifact.

2.5. Feedback questionnaire

To examine the contribution of the CCs to better understanding of anatomy and histology, students (N=15) of the elective course Corrosion Casts in Anatomy were asked in a questionnaire to choose the most fitting mark on a Likert scale (scale: 5- Strongly Disagree, 4- Disagree, 3- Not Sure, 2- Agree, 1- Strongly Agree) for the following statements:

- Viewing the corrosion casts with use of the following devices (stereomicroscope, SEM, micro-CT and video) helped me to learn the 3-D anatomy of the liver, spleen, kidney and Jung.
- Viewing the corrosion casts helped me to interconnect histology with gross anatomy.
- Viewing the corrosion casts helped me to better understand 2-D histological specimens I knew from histological classes.
- Using the corrosion casts is valuable in studying the clinical condition of these organs.

Following administration of the questionnaire, means and standard deviations were calculated for each response item.

3. Results

Regarding the questionnaire, students were very positive about the use of corrosion casts when learning anatomy and histology. On average, students agreed or strongly agreed that all methods by which they experienced the corrosion casts helped them learn the 3-D anatomy of that organ (Table 4). Comparing the average results for each organ and device, the best marked was the liver

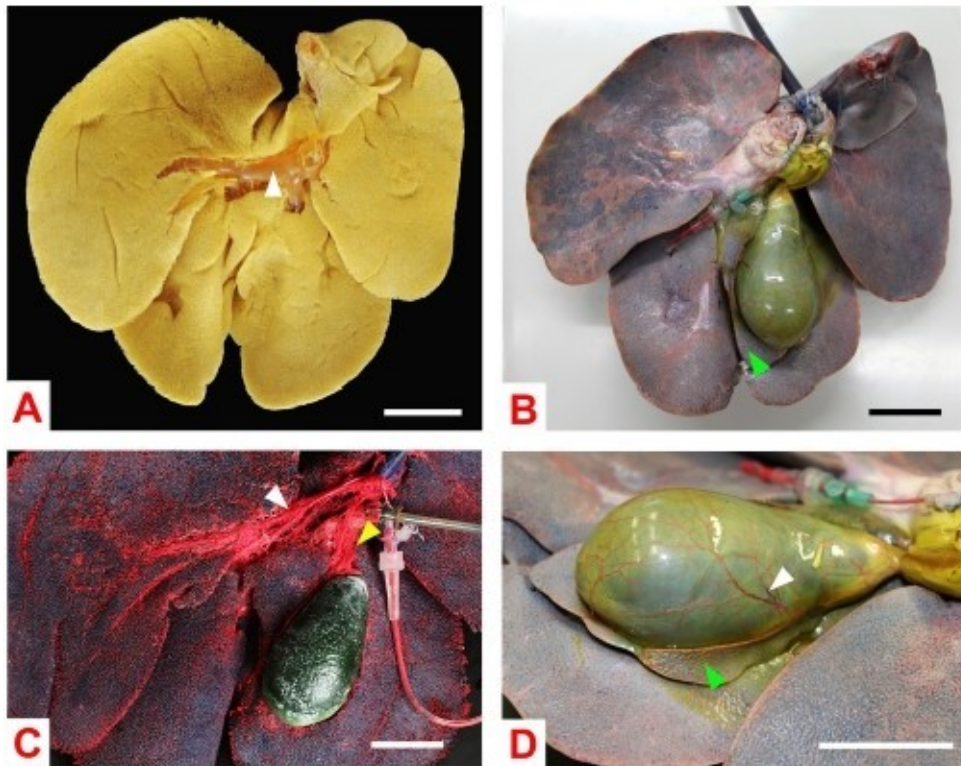


Fig. 1. Corrosioncasts of pig liver. (A) Filling with colored Biodur E20 Plus via the hepatic portal vein (white arrowhead). (B, C) Casts of liver and gallbladder (uncorroded) filled via the hepatic artery (red) and portal vein (blue). (D) Liver cast (after corrosion). Note the vasasorum of the portal vein (white arrowhead) and vessel of cystic duct (yellow arrowhead). (E) Gall bladder with cystic artery and vein (white arrowhead), quadrate lobe (green arrowhead). Scale bars 4 mm. (For interpretation of the references to color in this figure legend, the reader is referred to the web version of this article.)

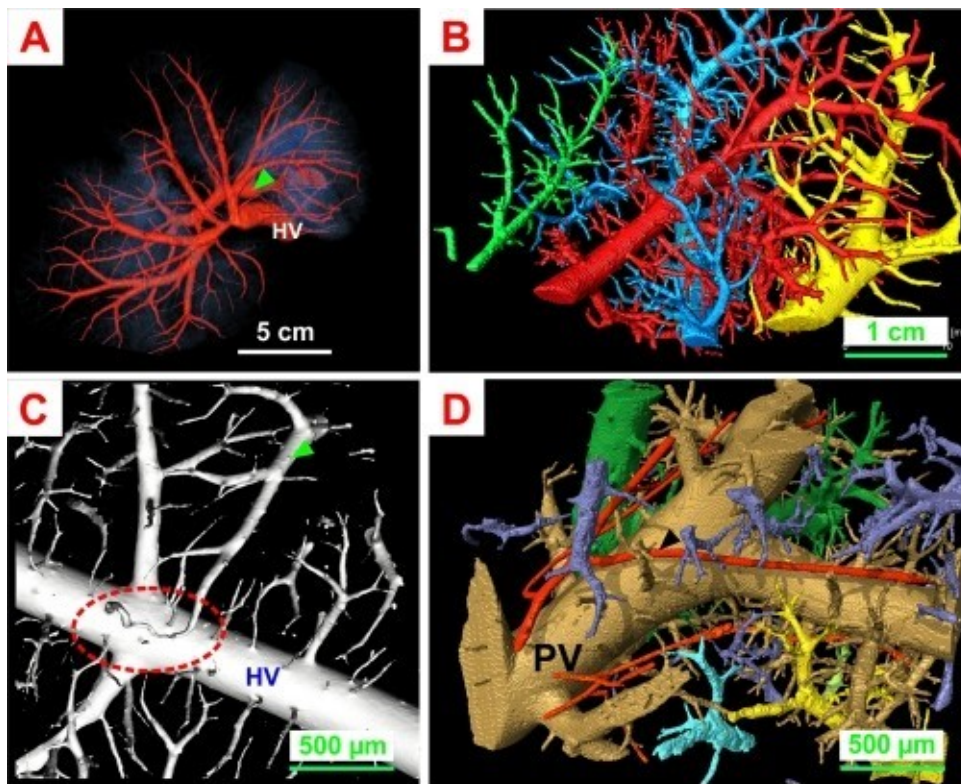


Fig. 2. Computed tomography of porcine liver corrosion cast. (A) Macroscopic view of portal and hepatic vein systems: hepatic vein (HV), portal vein (arrowhead). (B) μ -CT, 3D reconstruction, cast filled via the portal vein. (C) μ -CT, volume rendering technique. Demarcation of portal systemic anastomosis (nodules), tributary of hepatic vein (green arrowhead), and tributary of hepatic vein (HV). (D) Micro-CT, 3D reconstruction, cast filled via the portal vein (PV) and the hepatic artery (black arrowhead). (For interpretation of the references to color in this figure legend, the reader is referred to the web version of this article.)

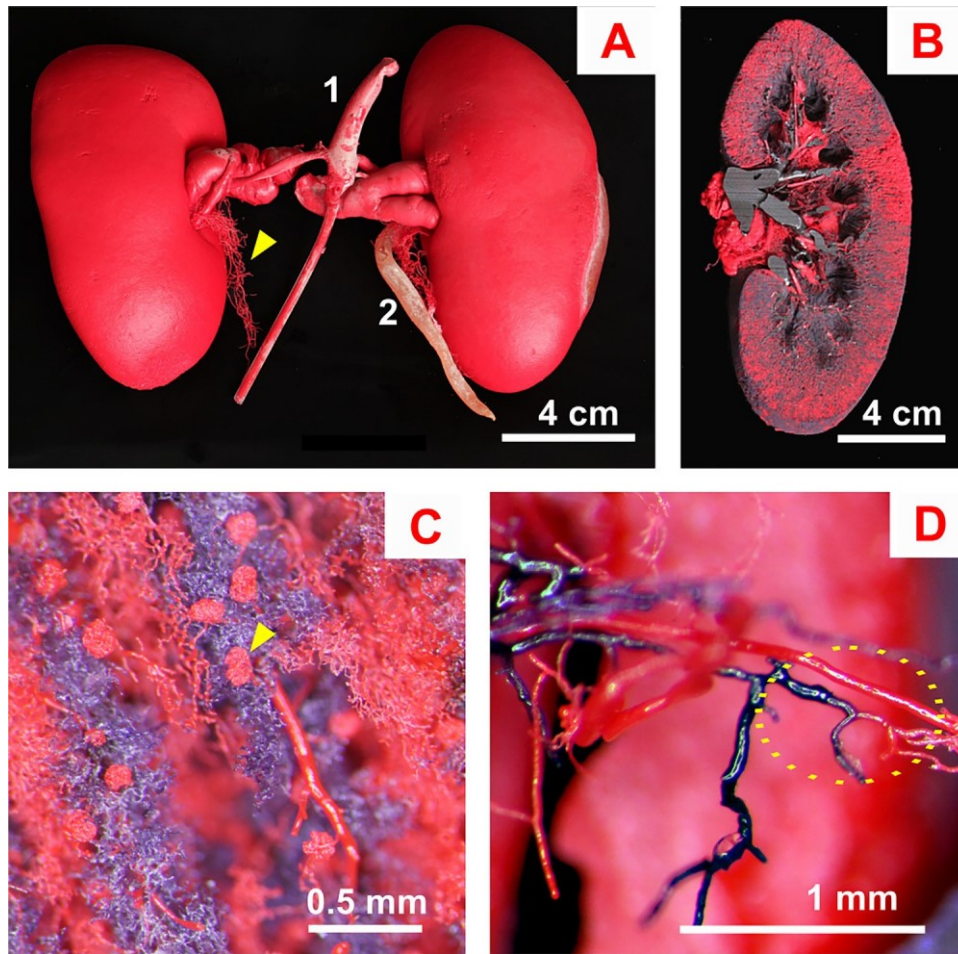


Fig. 3. Pig kidney cast with Biodur E20[®] Plus. (A) Cast filled via the abdominal aorta (1), left kidney also via the ureter (2), ureteric branches (yellow arrowhead). (B, C, D) Filling via the renal artery (red) and the renal vein (blue). (B) Frontal section. (C) Renal cortex with glomerulus (yellow arrowhead). (D) Arterio-venous anastomosis (yellow ellipse). (For interpretation of the references to color in this figure legend, the reader is referred to the web version of this article.)

Table 3

Schedule of elective anatomical classes.

	Practical session (150 min)	Subsequent week activities	Essential student aids
Week 1	Organ cannulating, resin injecting	Cast hardening, corrosion, rinsing	Protective glasses, lab coat, surgical gloves, respiratory mask
Week 2	Stereomicroscopy, cast freezing	Specimen cutting and cleaning for SEM	Stereomicroscope
Week 3	Scanning electron microscopy		Scanning electron microscope

Table 4

Results of the questionnaire, statement 1: "Viewing the corrosion casts with use of the following devices helped me learn the 3-D anatomy of the kidney, liver, lung and spleen."

Organ	Stereomicroscope	SEM	MicroCT	Video
Liver	1.5, SD 0.7	1.3, SD 0.7	1.5, SD 0.9	1.4, SD 0.8
Spleen	2.1, SD 1.1	1.4, SD 0.8	1.3, SD 0.7	1.7, SD 1.0
Kidney	1.5, SD 0.9	1.4, SD 0.8	1.4, SD 0.8	1.8, SD 1.0
Lung	2.0, SD 1.0	1.4, SD 0.7	1.3, SD 0.7	–

SD – standard deviation.

Table 5

Results of the questionnaire, statements 2–4:

Statement	Mean	SD
Viewing the corrosion casts helped me to interconnect histology with gross anatomy	1.5	0.7
Viewing the corrosion casts helped me to better understand 2-D histological specimens I knew from histological classes	1.4	0.7
Using the corrosion casts was useful when studying the clinical condition of these organs	1.8	0.8

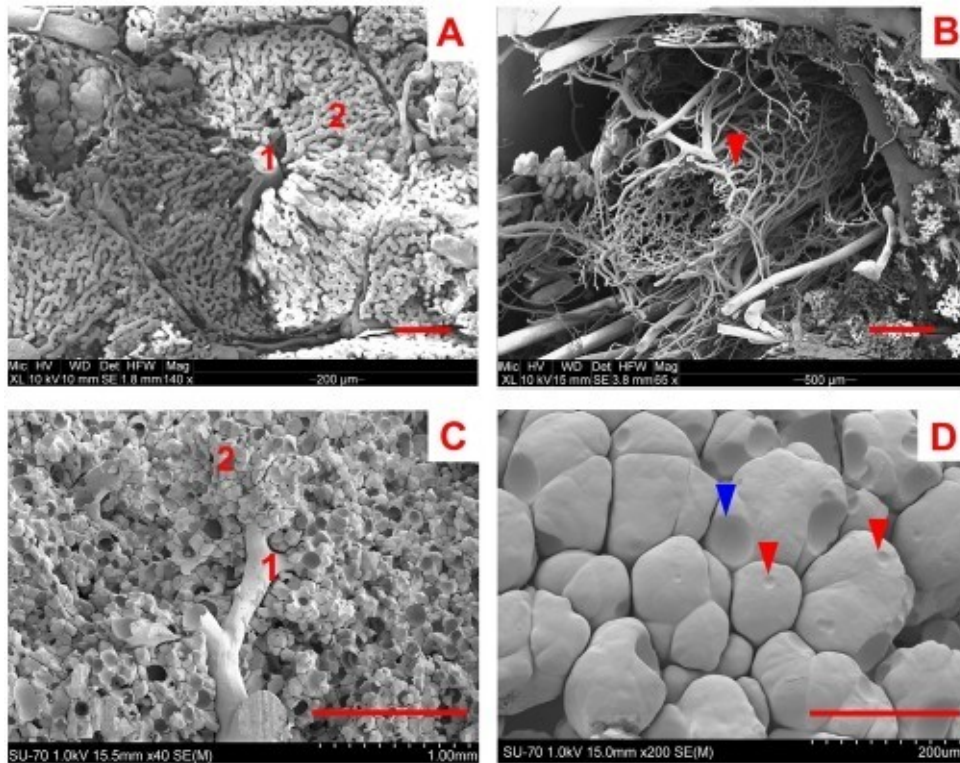


Fig.4. Vascular corrosion casts of porcine liver and lung. SEM. (A) Liver: central vein (1), sinusoids (2). (B) Periphery: penicillar artery (blue arrowhead), peripheral pulmonary sinusoids (red arrowhead). (C) Terminal bronchiole (1) and alveoli (2). (D) Pulmonary alveoli. Note nuclear imprints of pneumocytes (red arrowheads) and a capillary wall (blue arrowhead). Scale: (A), 200 μm ; (B), 1 mm; (C), 200 μm ; (D), 200 μm . (For interpretation of the references to color in this figure legend, the reader is referred to the web version of this article.)

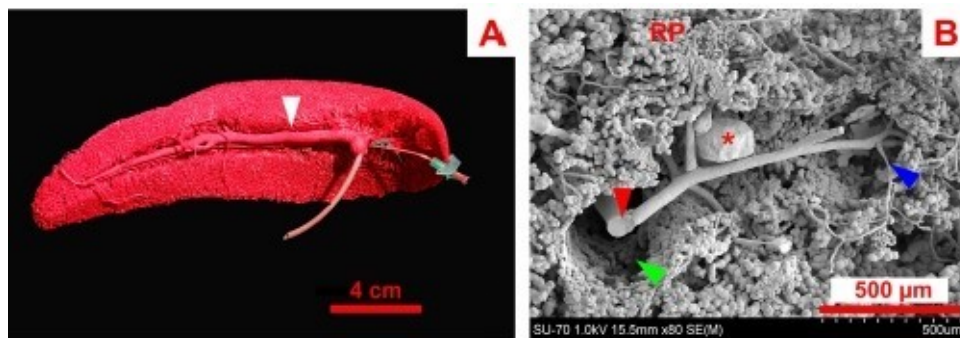


Fig.5. Vascular corrosion cast of the porcine spleen. (A) Filling with red-colored BiodurE2F via the splenic artery and vein (white arrowhead). (B) SEM. Note central artery (red arrowhead), missing perianterial lymphatic sheath (green arrowhead), penicillar artery (blue arrowhead) and nodal pulp (RP). Asterisk marks extravasated Biodur. (For interpretation of the references to color in this figure legend, the reader is referred to the web version of this article.)

(Mean 1.4, 50.0.7) and $\mu\text{-CT}$ (Mean 1.4, 50.0.8). 5 students also positively viewed the role of the casts in helping them connect histology with anatomy, understand the previously seen 2-0 specimens, and understand clinical conditions of those organs (Table 5).

4. Discussion

In teaching anatomy, the importance and merit of anatomical autopsy have not been and probably will not be overcome in the near future. Nevertheless, prosected specimens do not always provide the student with a clear picture of particular, delicate anatomical structures. This gap can be partly bridged by corrosion casts, which represent a 3-0 replica of hollow structures. As CCs represent real specimens, they support the learning process con-

siderably more than textbooks or even computer-based 3-0 models (Preece et al., 2013).

The idea of engaging students in active learning by letting them work with CCs is not new: CCs of bronchial trees have been used in classes previously (Cope, 2008; Hermiz et al., 2011; De Sordi et al., 2014). However, given that casting media were too viscous and did not fill tiny spaces, the casts only exhibited gross structures, such as the basic branching pattern, and they lacked detailed information on the terminal tree (Klawns and Tillmann, 1993). In contrast, BiodurE2F Plus passes through rough capillary-sized tubules and can fill (cast) large-sized spaces (high volume filling). This resin is a two-component, temperature-tolerant and chemically resistant resin that is suitable both for freezing and corrosion. It is relatively cheap (Table 1) and suitable for macro- and $\mu\text{-CT}$ scanning (Fig. 2). Its slightly flexible consistency is also advantageous for comfort-

et al. 2016), the extrahepatic porto-caval anastomoses (PC shunts)

are relevant structures in human medicine and play an extremely important role in cases of portal hypertension. PC shunts are found in the rectum, esophagus, abdominal wall, and retroperitoneum. They are valveless and serve as bypasses that open in cases that the blood cannot flow through the liver. When a large volume of blood circumvents the liver, varicose veins develop at the sites of porto-systemic anastomoses. They protrude, may rupture and, in

combination with the lack of coagulation proteins caused by the accompanied hepatopathy, cause life-threatening bleeding.

4.2. Spleen, kidney and bronchial tree corrosion casts

With respect to shape and position, the kidney is one of the most variable organs in humans. The prevalence of vascular variations is high (Mar and Tilkvatan, 2016). Nevertheless, there are many similarities between the human and pig kidney (Table 7), e.g., in parenchyma stratification, microangiarchitecture, and nephron morphology (Friis, 1980). The porcine kidney is a widely used animal model in experimental medicine (Tonar et al., 2009; Nath et al., 2014; Yang et al., 2015). The adult organ has a similar weight, size and number of nephrons as that in humans (Rytand, 1938). Of note,

there are 4 renal segments in pigs. In 91% of pigs, the renal artery bifurcates at or before the hilum into upper and lower polar arteries, each of which branches off into an anterior and a posterior segmental artery. The avascular plane is transverse in swine (Evan et al., 1996) but longitudinal in humans (Dyer et al., 2002). Pig kidney vascular CCs clearly demonstrate the difference between the texture of the cortex and medulla. The dotted cortex contains the glomeruli, whereas the striped medulla contains the straight arterioles. The outlines of renal pyramids are also distinct (Fig. 3B,C). The ureteric branches supplying the renal pelvis and upper ureter are clearly visible in the casts filled via the renal artery (Fig. 3A).

Similar size and anatomy to the human lung make the pig lung a beneficial model for biomedical research (Nishikawa et al., 2013; Judge et al., 2014). The lobar anatomy in pigs is similar to that of the human left lung, which consists of cranial and caudal lobes. The right lung is divided into four lobes: the cranial, middle, accessory and caudal. Interlobar fissures are incomplete. The right cranial lobar bronchus arises directly from the lateral wall of the trachea, whereas the other lobar bronchi ramify from the main

bronchi at the hilum. In the pig, the segmentation and bronchial ramification is more indented compared with humans, e.g., the left caudal lobar bronchus divides into 4 ventral and 4 dorsal segmental bronchi (Nakakuki, 1994). Porcine airways are more cartilaginous

but exhibit a similar number of bronchial generations (N=23) as humans (Maina and van Gils, 2001). In contrast to humans, the porcine branching pattern is monopodial (Neble et al., 2010). In addition, the secondary lobules are completely separated by con-

Table 7
Similarities between the porcine and human organs relevant for vascular corrosion casting.

Organ (Pig)	Macroanatomy	Microanatomy
Liver	Similar size, hilum with PV, HA proper and right and left hepatic ducts; 8 segments	Hepatic lobule, portal triad in portal spaces, sinusoids, central vein
Spleen	Segmental arteries are end arteries	Red pulp (vascular sinus) and white pulp (central arteriole, periarteriolar lymphoid sheath, lymphoid follicles)
Kidney	Similar size, smooth surface, medulla and cortex; renal pyramids, minor (approximately 10) and major (2–3) calices end in renal pelvis; segmental arteries are end arteries	Renal corpuscle and convoluted tubules in cortex, straight tubules, loop of Henle and collecting ducts in medulla
Bronchial tree and lung	Similar size; 2 lobes in the left lung	Similar number of bronchial generations

nective tissue septa; i.e., they are clearly demarcated in the CC after soft tissue digestion. Toward the periphery, the respiratory bronchioles give rise to alveolar ducts that end in alveoli (Fig. 4C, D).

The shape of the porcine spleen is significantly different from the human spleen. Splens obtained from our Prestice Black-Pied pigs aged 16–18 weeks were approximately 20 cm long and 6 cm wide (Fig. 5A). The splenic artery divides close to the hilum into 2 segmental branches, which supply two independent splenic segments (Pereira-Sampaio and Marques-Sampaio, 2006). According to a Web of Science search (April 2017, key words “pig spleen histology”); the ultrastructure of the porcine spleen has been studied mainly in connection with experiments and histopathology (Palzer et al., 2015; Suzuki et al., 2016). To understand the spleen’s functions; it is important to have knowledge of the 3-D structure of the microvasculature; the tissue compartments and the cell distribution. Given that mammalian splens have an open circulation; corrosion casting is not an ideal method for studying the red pulp. Nevertheless; in the white pulp Biodur E20[®] CCs clearly demonstrate the central and penicillar arteries and indicate the presence of the periarteriolar lymphoid sheaths (Fig. 5B).

4.3. Useful tips for easy teaching

- Highlight cast structures by color-coding, e.g., using differently colored Biodur E20[®] Plus for arteries (e.g., red Biodur) and veins (e.g., blue Biodur). It enables the ability to distinguish the two vascular beds (Figs. 1, 3). For this purpose, either the colored Biodur E20[®] dye can be used, or the clear Biodur E20[®] can be dyed with different dye pastes.
- As the fresh organs are not always available, an organ filled with Biodur E20[®] can be stored in 50% alcohol and corroded later.
- It is also useful for the anatomy classes for the instructor to demonstrate the vascular density showing the students the organ before and after corrosion (Fig. 1A, B).
- Looking at the CCs, students do not often understand what they see. The instructor should ask questions dealing with the structures on the cast to train the students’ imagination; point out that there is not any soft tissue present and that the students are seeing the filling of the former vessels (cavities); and relate the corrosion casts to clinical conditions (for example, the instructor can ask students how the cast would look different in a cirrhotic liver).

5. Conclusions

Pigs are frequently used as large-animal models. Corrosion casts of porcine organs with Biodur E20[®] Plus appeared to be valuable for teaching human anatomy of cardiovascular, respiratory, digestive, and urogenital systems. We present a manual for the corrosion casting and the cast analysis in the elective anatomical classes. Our casting protocol and the range of CC assessment offer different variations adjustable to the particular technical demands. Biodur E20[®] passes through capillary-sized tubes and

enables both gross anatomy and microstructural research. Highlighting structures using different color-coded Biodur allows for a clear demonstration of gross arterial supply and venous drainage as well as different kinds of anastomosis and microvascular patterns. Assessments of casts enable instructors to demonstrate particular structures of clinical importance, using a stereomicroscope and/or scanning electron microscope together with 3-D reconstructions based on CT scans. They also enable the creation of original visual aids, and involve the students directly in the active learning process, helping them to better understand 2-D images they know from textbooks or histological specimens. Students find the use of these corrosion casts useful for their learning, across a variety of tissues and visualization methods. Finally, Biodur E20[®] Plus corrosion casting might also be a valuable teaching tool in veterinary anatomy or other biological science classes.

Role of funding source

This study was supported by Ministry of Education Youth and Sports of the Czech Republic and the National Sustainability Programme [Grant Numbers LO1503, CENTEM CZ.1.05/2.1.00/03.0088, CENTEMPLUS (LO1402)]; Charles University in Prague [Grant Numbers SVV-2017 No 260392, IP 2016–18, GAUK No. 1206417] and Research Fund (Progres Q39). S. Leupen was supported by J. William Fulbright Commission.

Acknowledgments

Many thanks to Dr. Örs Petnehazy, Ph.D. and Dita Gharabaghi for sharing their valuable experience.

Appendix A. Supplementary data

Supplementary data associated with this article can be found, in the online version, at <http://dx.doi.org/10.1016/j.aanat.2017.05.005>.

References

- Aharinejad, S.H., Lametschwandtner, A., 1992. *Microvascular Corrosion Casting in Scanning Electron Microscopy*, first edition. Springer, Berlin-Heidelberg-Wien, pp. 3–9 (a), p. 58 (b).
- Avritscher, R., Abdelsalam, M.E., Javadi, S., Ensor, J., Wallace, M.J., Alt, E., Madoff, D.C., Vykoukal, J.V., 2013. Percutaneous intraportal application of adipose tissue-derived mesenchymal stem cells using a balloon occlusion catheter in a porcine model of liver fibrosis. *J. Vasc. Interv. Radiol.* 24, 1871–1878.
- Bedoya, M., del Rio, A.M., Chiang, J., Brace, C.L., 2014. Microwave ablation energy delivery: influence of power pulsing on ablation results in an ex vivo and in vivo liver model. *Med. Phys.* 41, 123301.
- Carreño, O., Sendra, L., Montalvá, E., Miguel, A., Orbis, F., Herrero, M.J., Noguera, I., Aliño, S.F., Lopez-Andujar, R., 2013. A surgical model for isolating the pig liver in vivo for gene therapy. *Eur. Surg. Res.* 51, 47–57.
- Christo, M.C., DiDio, L.J., 1997. Anatomical and surgical aspects of splenic segmentectomies. *Ann. Anat.* 179, 461–474.
- Çinar, C., Türkvatán, A., 2016. Prevalence of renal vascular variations: evaluation with MDCT angiography. *Diagn. Interv. Imaging* 97, 891–897.
- Cope, L.A., 2008. Tracheobronchial cast production and use in an undergraduate human anatomy course. *Anat. Sci. Educ.* 1, 23–26.

- Couinaud, C., 1954. Liver lobes and segments: notes on the anatomical architecture and surgery of the liver. *Presse Med.* 62, 709–712.
- Court, F.G., Wemyss-Holden, S.A., Morrison, C.P., Teague, B.D., Laws, P.E., Kew, J., Dennison, A.R., Maddern, G.J., 2003. Segmental nature of the porcine liver and its potential as a model for experimental partial hepatectomy. *Br. J. Surg.* 90, 440–444.
- Davies, A., 1973. The evolution of bronchial casts. *Med. Hist.* 17, 386–391.
- De Sordi, N., Bombardi, C., Chiocchetti, R., Clavenzani, P., Trerè, C., Canova, M., Grandis, A., 2014. A new method of producing casts for anatomical studies. *Anat. Sci. Int.* 89, 255–265.
- Debbaut, C., Segers, P., Cornillie, P., Casteleyn, C., Dierick, M., Laleman, W., Monbaliu, D., 2014. Analyzing the human liver vascular architecture by combining vascular corrosion casting and micro-CT scanning: a feasibility study. *J. Anat.* 224, 509–517.
- Dyer, R.B., Regan, J.D., Kavanagh, P.V., Khatod, E.G., Chen, M.Y., Zagoria, R.J., 2002. Percutaneous nephrostomy with extensions of the technique: step by step. *Radiographics* 22, 503–525.
- Eberlova, L., Liska, V., Mirka, H., Gregor, T., Tonar, Z., Palek, R., Skala, M., Bruha, J., Vycital, O., Kalusova, K., Haviar, S., Kralickova, M., Lametschwandtner, A., 2015. Porcine liver vascular bed in Biodur E20 corrosion casts. *Folia Morphol. (Warsz)* 75, 154–161.
- Elias, H., Petty, D., 1953. Terminal distribution of the hepatic artery. *Anat. Rec.* 116, 9–17.
- Evan, A.P., Connors, B.A., Lingeman, J.E., Blomgren, P., Willis, L.R., 1996. Branching patterns of the renal artery of the pig. *Anat. Rec.* 246, 217–223.
- Friis, C., 1980. Postnatal development of the pig kidney: ultrastructure of the glomerulus and the proximal tubule. *J. Anat.* 130, 513–526.
- Fu, Y.B., Chui, C.K., 2014. Modelling and simulation of porcine liver tissue indentation using finite element method and uniaxial stress-strain data. *J. Biomech.* 47, 2430–2435.
- Gerlach, N., Minnich, B., Lametschwandtner, A., 2014. Microvascularization and histomorphology of lateral line organs in adult *Xenopus laevis*. *J. Morphol.* 275, 497–503.
- Gnutzmann, D.M., Mechel, J., Schmitz, A., Köhler, K., Krone, D., Bellemann, N., Gockner, T.L., Mokry, T., Kortcs, N., Sommer, C.M., Kauczor, H.U., Radeleff, B.A., Stampfl, U., 2015. Evaluation of the plasmatic and parenchymal elution kinetics of two different irinotecan-loaded drug-eluting embolics in a pig model. *J. Vasc. Interv. Radiol.* 26, 746–754.
- Haenssger, K., Makanya, A.N., Djonov, V., 2014. Casting materials and their application in research and teaching. *Microsc. Microanal.* 20, 493–513.
- Hermiz, D.J., O'Sullivan, D.J., Lujan, H.L., DiCarlo, S.E., 2011. Constructivist learning of anatomy: gaining knowledge by creating anatomical casts. *Anat. Sci. Educ.* 4, 98–104.
- Hytioglou, P., 2011. Hepatitis C. In: Saxena, R. (Ed.), *Practical Hepatic Pathology, A Diagnostic Approach*. Elsevier Saunders, Philadelphia, pp. 229–231.
- Jiřík, M., Tonar, Z., Králíčková, A., Eberlová, L., Mirka, H., Kochová, P., Gregor, T., Hošek, P., Svobodová, M., Rohan, E., Králíčková, M., Liška, V., 2016. Stereological quantification of microvessels using semiautomated evaluation of X-ray microtomography of hepatic vascular corrosion casts. *Int. J. Comput. Assist. Radiol. Surg.* 11, 1803–1819.
- Judge, E.P., Hughes, J.M., Egan, J.J., Maguire, M., Molloy, E.L., O'Dea, S., 2014. Anatomy and bronchoscopy of the porcine lung. A model for translational respiratory medicine. *Am. J. Respir. Cell Mol. Biol.* 51, 334–343.
- Klawns, G.R., Tillmann, B., 1993. From the specimen workstation. Injection of synthetic materials of arteries using a four color technique – with an example of head and neck blood vessels. *Ann. Anat.* 175, 221–224.
- Lametschwandtner, A., Lametschwandtner, U., Weiger, T., 1990. Scanning electron microscopy of vascular corrosion casts – technique and applications: updated review. *Scanning Microsc.* 4, 889–940.
- Maina, J.N., van Gils, P., 2001. Morphometric characterization of the airway and vascular systems of the lung of the domestic pig, *Sus scrofa*: comparison of the airway, arterial and venous systems. *Comp. Biochem. Physiol. A: Mol. Integr. Physiol.* 130, 781–798.
- Mortensen, K.E., Revhaug, A., 2011. Liver regeneration in surgical animal models – a historical perspective and clinical implications. *Eur. Surg. Res.* 46, 1–18.
- Mulligan-Kehoe, M.J., Simons, M., 2014. Vasa vasorum in normal and diseased arteries. *Circulation* 129, 2557–2566.
- Murakami, T., 1971. Application of the scanning electron microscope to the study of the fine distribution of the blood vessels. *Arch. Histol. Jpn.* 32, 445–454.
- Nakakuki, S., 1994. Bronchial tree, lobular division and blood vessels of the pig lung. *J. Vet. Med. Sci.* 56, 685–689.
- Nath, J., Guy, A., Smith, T.B., Cobbold, M., Inston, N.G., Hodson, J., Tennant, D.A., Ludwig, C., Ready, A.R., 2014. Metabolomic perfusate analysis during kidney machine perfusion: the pig provides an appropriate model for human studies. *PLoS One* 9, e114818.
- Nishikawa, H., Oto, T., Otani, S., Harada, M., Iga, N., Miyoshi, K., Miyoshi, S., 2013. Unilateral lung transplantation using right and left upper lobes: an experimental study. *J. Thorac. Cardiovasc. Surg.* 146, 1534–1537.
- Noble, P.B., McLaughlin, R.A., West, A.R., Becker, S., Armstrong, J.J., McFawn, P.K., Eastwood, P.R., Hillman, D.R., Sampson, D.D., Mitchell, H.W., 2010. Distribution of airway narrowing responses across generations and at branching points, assessed in vitro by anatomical optical coherence tomography. *Respir. Res.* 11, 9.
- Nowell, J.A., Tyler, W.S., 1971. Scanning electron microscopy of the surface morphology of mammalian lungs. *Am. Rev. Respir. Dis.* 103, 313–328.
- Ohtani, O., Murakami, T., Jones, A.L., 1982. Microcirculation of the liver, with special reference to the peribiliary portal system. In: Motta, P.M., DiDio, L.J.A. (Eds.), *Basic and Clinical Hepatology*. Martinus Nijhoff Publishers, Hague/Boston/London, pp. 85–96.
- Okada, N., Mizuta, K., Oshima, M., Yamada, N., Sanada, Y., Ihara, Y., Urahashi, T., Ishikawa, J., Tsuji, T., Hishikawa, S., Teratani, T., Kobayashi, E., 2015. A novel split liver protocol using the subnormothermic oxygenated circuit system in a porcine model of a marginal donor procedure. *Transplant. Proc.* 47, 419–426.
- Paluzzi, A., Belli, A., Bain, P., Viva, L., 2007. Brain 'imaging' in the Renaissance. *J. R. Soc. Med.* 100, 540–543.
- Palvanov, A., Marder, R.L., Siegel, D., 2016. Asymptomatic intrahepatic portosystemic venous shunt: to treat or not to treat? *Int. J. Angiol.* 25, 193–198.
- Palzer, A., Austin-Busse, R.L., Ladinig, A., Balka, G., Zoels, S., Ritzmann, M., 2015. Histopathologic lesions in conventional pigs experimentally infected with *Haemophilus parasuis* serovar 5. *Tierarztl. Prax. Ausg. G Grosstiere Nutztiere* 43, 91–96.
- Pereira-Sampaio, M.A., Marques-Sampaio, B.P., 2006. Anatomical study and proportional analysis of the pig spleen arterial segments. *Cells Tissues Organs* 182, 32–34.
- Preece, D., Williams, S.B., Lam, R., Weller, R., 2013. Let's get physical: advantages of a physical model over 3-D computer models and textbooks in learning imaging anatomy. *Anat. Sci. Educ.* 6, 216–224.
- Rytand, D.A., 1938. The number and size of mammalian glomeruli as related to kidney and to body weight, with methods for their enumeration and measurement. *Am. J. Anat.* 62, 507–520.
- Suzuki, R., Shin, D., Richards-Kortum, R., Coghlan, L., Bhutani, M.S., 2016. In vivo cytological observation of liver and spleen by using high-resolution microendoscopy system under endoscopic ultrasound guidance: a preliminary study using a swine model. *Endosc. Ultrasound* 5, 239–242.
- Tonar, Z., Janáček, J., Nedorost, L., Grill, R., Báca, V., Zátura, F., 2009. Analysis of microcracks caused by drop shatter testing of porcine kidneys. *Ann. Anat.* 191, 294–308.
- Tonar, Z., Tomášek, P., Loskot, P., Janáček, J., Králíčková, M., Witter, K., 2016. Vasa vasorum in the tunica media and tunica adventitia of the porcine aorta. *Ann. Anat.* 205, 22–36.
- Twelves, D., Nerurkar, A., Osin, P., Ward, A., Isacke, C.M., Gui, G.P., 2012. The anatomy of fluid-yielding ducts in breast cancer. *Breast Cancer Res. Treat.* 132, 555–564.
- Vrtková, I., 2015. Genetic admixture analysis in Prestice Black-Pied pigs. *Arch. Anim. Breed.* 58, 115–151.
- Wang, J.Z., Liu, Y., Wang, J.L., Lu, L., Zhang, Y.F., Lu, H.W., Li, Y.M., 2015. Sequential vs simultaneous revascularization in patients undergoing liver transplantation: a meta-analysis. *World J. Gastroenterol.* 21, 7036–7046.
- Xu, J., Lu, X., Shi, G.P., 2015. Vasa vasorum in atherosclerosis and clinical significance. *Int. J. Mol. Sci.* 16, 11574–11608.
- Yang, H., Weng, G., Yao, X., Tang, C., Shan, Y., 2015. Arterial injury during percutaneous nephrostomy: angiography findings from an Isolated Porcine Kidney Model. *Urol. J.* 12, 2396–2399.

Příloha II:

EBERLOVA, Lada, Anna MALECKOVA, Patrik **MIK**, Zbynek TONAR, Miroslav JIRIK, Hynek MIRKA, Richard PALEK, Sarah LEUPEN a Vaclav LISKA, 2020. Porcine Liver Anatomy Applied to Biomedicine. Journal of Surgical Research [online]. 250, 70–79. ISSN 0022-4804. Dostupné z: doi:10.1016/j.jss.2019.12.038. **IF₂₀₁₉=1,841, Q3**(Surgery).



ELSEVIER

Available online at www.sciencedirect.com

ScienceDirect



E

journal homepage: www.JournalofSurgicalResearch.com

Research review

Porcine Liver Anatomy Applied to Biomedicine

Check for updates

**Eberlova Lada, MD, PhD^{a, b} • Maleckova Anna, MD^{b, c} Mik Patrik, MA^{a, c}
Tonar Zbynek, MD, PhD^{b, c} Jirik Miroslav, MA, PhD^b Mirka Hynek/d
Palek Richard, MD/e • Leupen Sarah, BA, PhD/
and Liska Vaclav, MD, PhD^b**

^aFaculty of Medicine in Pilsen, Department of Anatomy, Charles University, Pilsen, Czech Republic

^bFaculty of Medicine in Pilsen, Biomedical Centre, Charles University, Pilsen, Czech Republic

^cFaculty of Medicine in Pilsen, Department of Histology and Embryology, Charles University, Pilsen, Czech Republic

^dDepartment of Imaging Methods, University Hospital in Pilsen, Pilsen, Czech Republic

^eDepartment of Surgery, University Hospital in Pilsen, Pilsen, Czech Republic

^fDepartment of Biological Sciences, University of Maryland Baltimore County, Baltimore, Maryland

ARTICLE INFO

Article history:

Received 4 May 2019

Received in revised form

16 October 2019

Accepted 28 October 2019

Available online xxx

Keywords:

Biomedical research

Domestic pig

Liver

Anatomy

Histology

ABSTRACT

Currently, there are at least 70 pure domestic pig breeds, but only certain breeds are used in biomedical research. The domestic pig liver is suitable for preclinical research because its size, physiology, and anatomy are similar to that of the human liver; in addition, there is a high degree of genetic similarity between the two species. For planning experiments and identifying improvements in both invasive and noninvasive methods of liver disease management, the morphological similarities and dissimilarities of the pig liver to its human counterpart must be taken into consideration along with sexual dimorphism and interindividual and interspecific variability. Retrospective histological evaluations based on stereological methods enable precise quantitative morphological estimates and guarantee their unbiased accuracy. The results thereof are crucial for revealing and assessing histological changes and can contribute to the optimization of study designs. New trends in computed tomography data processing have also been introduced. This review article summarizes the newest trends and findings in the field of porcine liver anatomy and histology as applicable to preclinical research.

© 2020 Elsevier Inc. All rights reserved.

Declaration of conflict of interest: none.

Photographs used in the text are original and the pigs from which the liver was obtained were treated in accordance with EU directive for animal experiments. The surgical and anesthesiological procedures were certified by the Commission for Work with Experimental Animals at the Pilsen Medical Faculty of Charles University, Prague, and were under the control of the Ministry of Agriculture of the Czech Republic.

Corresponding author: Faculty of Medicine in Pilsen, Department of Anatomy, Charles University, Karlovarska 48, DI 66 Pilsen, Czech Republic. Tel.: +4203775933; fax: +4203 77593309

E-mail address: lada.eberlova@fp.cuni.cz (E. Lada).

0022-4445/\$ - see front matter © 2020 Elsevier Inc. All rights reserved.

<https://doi.org/10.1016/j.jss.2019.12.038>

Introduction

The domestic pig (*Sus scrofa domestica*) is an even-toed ungulate

mammal. Genetic evidence indicates that this species

developed from the wild boar in Southeast Asia approximately 5 million years ago, and domestication began in Eurasia approximately 10,000 years ago.¹ Hence, there is a general consensus that all variations of pigs (including mini/micro miniature) descend from the Eurasian wild boar. Swine were first used in biomedical research (BMR) in the 1940s, and their use has increased since the 1960s.² More recently, molecular biology and genetics have been applied to the breeding process to enhance selection for valuable traits. At present, the number of pig breeds is uncertain, but a review of more than 70 pure domestic pig breeds from all over the world is maintained on

The Pig Site.³ Most of these breeds are primarily used for consumption, but certain small breeds are also used for BMR.⁴ Because the porcine genome, which consists of 18 autosomes and 2 sex chromosomes, has been sequenced and its extensive

homology to humans has been demonstrated,⁵ genetically

modified pigs have played an important role in translational studies focused on numerous disease areas, including cancer, diabetes mellitus, Alzheimer's disease, cystic fibrosis, and Duchenne muscular dystrophy.⁶ In addition, because the

structure and function of the porcine cardiovascular, renal,

and gastrointestinal organs are similar to those of humans,⁷ these organs are extensively used in experimental surgery to test surgical techniques and experimental therapies... before their use in humans (table 1). In addition, the swine can live up to 10 years, thereby allowing these researchers long-term follow-up after experimental procedures.

The small pigs used in BMR, from an anatomical and

physiological perspective, are similar to the domestic swine. The advantages of their small size are obvious: these pigs are easy to handle and house, and they require less food and test substances than larger pigs. Therefore, certain small breeds are predominantly used in pharmacology and toxicology studies for the testing of new drugs and medical devices^{4,2} (table 1). Nevertheless, the availability of small breeds is

limited.

Porcine liver gross anatomy

In terms of gross anatomy, from four to six liver lobes have

been described in pigs (Table 2), and the right and left hepatic lobes are separated by a deep notch for the round ligament (Fig. 1A and B). The number and size of the lobes (segments) reported varies and thus may be breed-specific. Only the

Table 1. Porcine liver applications in biomedical research

Objects of research	References	Breed
Ablation, resection	•	OJ. angxi e. ama. mi. ni. pig
	""	Wuzhushan pig
	"	Not mentioned
Biomechanics	u	Not mentioned
	""	Ecol. ogically bred animals of various origins
Gene therapy	""""	HSDIIBI-transgenic pig
	u	Duroc, Pietrain, Landrace, large white pig
	"	e. ama. miniature pig
Innovation of surgical techniques	""	Lan drace pig
	""	Landrace pig
Liver transplantation	""	e. ama. miniature pig
	""	Micromini pigs (Fuji Micro Line, Sluzuoaka, Japan)
	""	Lan drace pig GalT-KO pig
Liver traumatology	25	Yorblure-1. andrace pig
	""	Cermandestic pig
Material testing	""	Not mentioned
	""	Oline experimental hybrid pigs
Mathematical modeling, quantification	""	Cerman Landrace pigs
	""	Not mentioned
Morphology, physiology	""	Prestice Black:-Pied pig
	""	Prestice Black:-Pied pig
	""	Prestice Black:-Pied pig
Pathogenesis, liver failure	ss	White pig
	""	Prestice Black:-Pied pig
	""	Prestice Black:-Pied pig
Pharmacology, toxicology	""	Specific pathogen-free piglet
	""	Sama experimental miniature pig
Pharmacology, toxicology	""	Sama experimental miniature pig
	""	Prestice Black:-Pied pig

following 6ve Jobs are invariably present the left lateral, left
media rightlater right media!, and the caudate Jobe. From

Landrace x largewlute pig

our experiencewiththe Prestice Black-Pied pigbreed,.. which

Regeneration

"

Not mentioned

is in agreement with the veterinary anatomical text'books⁴⁹
the quadrate lobe is present occasionally (Fig. 1B and D).
There also seems to be interbreed variability in the Jobe pro-
portions. Court *et al.*⁵⁰ found the left lateral lobe to be the

"
"'"'

Polishwlute pig

Prestice Black:-Pied pig

largest, whereas Bekheit *et al.*,³⁵ based on computed tomog-
raphy (CT) volumetry, assessed the right media! Jobe to be the
mostvoluminous.

In the pig, eight segments roughly similar to those in the
human liver havebeen desmbesd ..s, (Tables 2 and 3; Fig.1A
and B). However, both the differences between pigs and

Table 2 Liver segmental anatomy, literature review

Breed	No of lobes	Name of the lobes	No of segments	Reference
Not mentioned	5	Rightlateral, rightmedial, leftlateral, left med.ial, caudate	8	55
Not mentioned	5	Right, left, right media!, left media!, caudate	8	55
Prestice Black:-Pi ed pig	5 (6)	Rightlateral, right med.ial, leftlateral, left med.ial, caudate, quadrateoccasionally	Not mentioned	• •
Not mentioned	4	Right, left, right paramedian, leftparamedian	8	55
Prestice Black:-Pi ed pig	6	Rightlateral, rightmed.ial, leftleateral, left med.ial, caudate, quadrate		• •
Not mentioned	3	Notnamed	8	52
Not mentioned	5	Right, left, rightmiddle, left middle, caudate	8	53

humans and among breeds of pigs must be taken into account in extrapolating from porcine to human liver surgery. Unlike in the human liver, the so-called Rex-Candieline that divides the embryological and morphological right and left hemiliver is well marked in pigs by the deep notch for the round ligament, flossura ligament teretis (Fig. 1A and B). This line can be seen after ligation of the right or left lobar branch of the porta!

vein (PV). However, owing to the intraparenchymal thin-

walled caudal vena cava (Fig. 10), resection of the right lateral lobe in the pig liver is extremely difficult. The liver hilum is located dorsally on the visceral surface, and the PV ramifies a few centimeters outside the parenchyma out to the right lobe.^{50, 3} The hepatic artery, the porta! vein, and the common hepatic duct branch are accompanied by considerable connective tissue (Fig. 18) that derives from the

perivascular fibrous capsule (of Glisson) and forms pedicles very similar to the ones found in the human livers.⁵⁵ The gallbladder lies within the substance of the right medial lobe, if present, and it separates this lobe from the quadrate lobe⁴⁹ (Fig. 1880).

Although the PV supplies up to 90% of the blood volume and up to 2/3 of the oxygen supply to the liver, the hepatic

artery proper is irreplaceable for its supply of the biliary tree

(Fig. 1 q). In experimental studies, embolization or ligation of a PV branch was used to stop the blood flow throughout a part of the liver. In this procedure, the part of the liver with restricted blood flow atrophies, whereas the rest of the tissue hypertrophies. This method is also used in human subjects, for example, in patients with colorectal carcinoma metastasis in the right liver lobe; after intestinal surgery and also most often

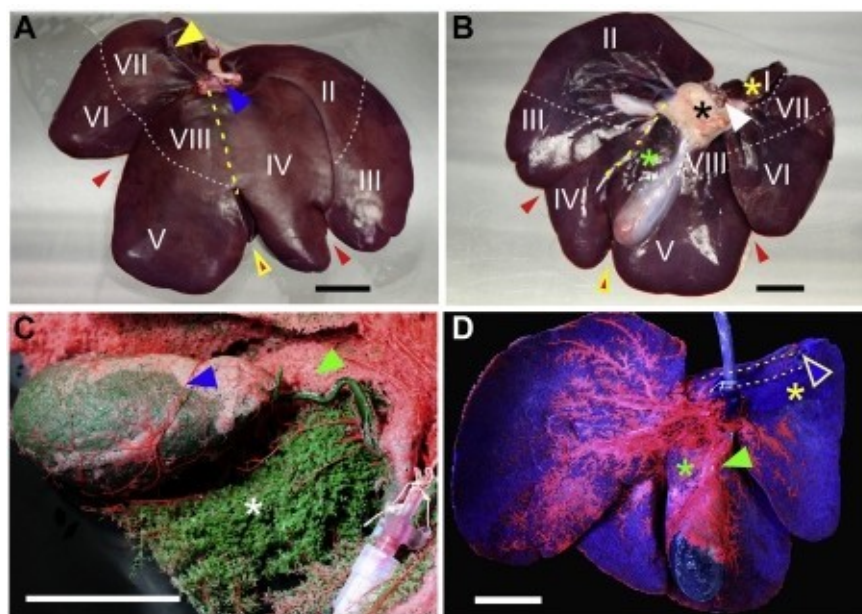


Fig. 1 Porcine liver gross anatomy and corrosion casts, Prestice, Black-Pied breed. (A, B) Segmental anatomy, claspbragmatic (A) and viscerosurface (B). Intercalated notches (reclapbragmatic), notch for the ligamentum teretis (yellow-red arrowheads), Rex-Candieline (yellow lines), coronary ligament (yellow arrowhead), caudal vena cava (blue arrowhead), porta! vein (white arrowhead), hepatoduodenal ligament (black asterisk), caudal lobe (yellow asterisk), and quadrate lobe (green asterisk). (C, D) Vascular corrosion cast, filling with colored Biodur E20 Plus (Heidelberg, Germany) via the hepatic portal vein (blue), hepatic artery (red) and biliary duct (green). Caudal lobe (yellow asterisk), quadrate lobe (green asterisk), cystic artery (blue arrowhead), biliary network of the cystic duct (green arrowheads), biliary ductules (white asterisk), caudal vena cava (blue arrowhead).

Table 3 Porcine liver lobes and segments according to Court *et al.*⁵³ and Zancbet and Monteiro⁵³
Corresponding parenchyma Segment

Caudate lobe	S I
Left lateral lobe	sn, m
Left medial lobe	S IV
Right medial lobe	sv, vm
Right lateral lobe	SVI, VII

after chemotherapy, embolization of the right PV is performed (the arterial supply is preserved to avoid necrosis.) The lobe with metastasis atrophies, whereas the contralateral lobe

undergoes compensatory hypertrophy, which, after several

weeks (provided that the parenchyma is functionally sufficient), allows for the resection of the part with the malignant deposit. Unfortunately, the growth of the nonoccluded liver is not always sufficient to avoid liver failure. Therefore, experimental studies using the porcine liver model for testing various occlusive methods and/or pharmacological treatments have been designed.^{46, 57}

Porcine liver microanatomy

For studies of human liver diseases using the porcine liver model, detailed knowledge of liver microanatomy is necessary. The tissue structure of the porcine liver is similar to that

of the human liver.⁷ The parenchymal architecture is organized into well-defined, polygonal lobules centered around the central vein with portal triads at its corners (Figs. 2A and C,

3AeC). The portal lobules are demarcated by fibrous septa containing variable amounts of connective tissue (Fig. 3AeE). Three-dimensional (3-D) reconstruction of the porcine liver has revealed that the morphological lobule is pentagonal rather than hexagonal as it is described in humans.⁵⁸ However, the exact size and shape of portal lobules in the porcine liver and their spatial organization remain unknown.

The functional acinar concept, first described in the human liver by Rappaport,⁵⁹ divides the parenchyma into three concentric zones based on the perfusion of the liver: the classical lobule, portal lobule, and sinus. As per this scheme,

metabolic zonation refers to the differences in expression of

the key metabolic genes in hepatocytes (HEPs) within different zones of the liver lobule; this zonation corresponds, to some degree, to the zones of the hepatic sinus.⁶⁰ However, this set of concepts is not sufficient to explain all the physiological and pathological processes in the liver.⁶¹

The morphometry and distribution of HEPs within the porcine liver was assessed by Unat et al.³⁶ In healthy pigs of the Prestice Black-Pied breed, each lobe contained HEPs of a comparable size, nuclearity, and density. However, the size and density were not uniformly distributed when comparing the different regions of the liver in relation to the hepatic vasculature (peripheral, paracaval, and periportal regions.) The reported fraction of binuclear HEPs, possibly linked to liver regeneration, was 4%. Interestingly, the number of nuclei

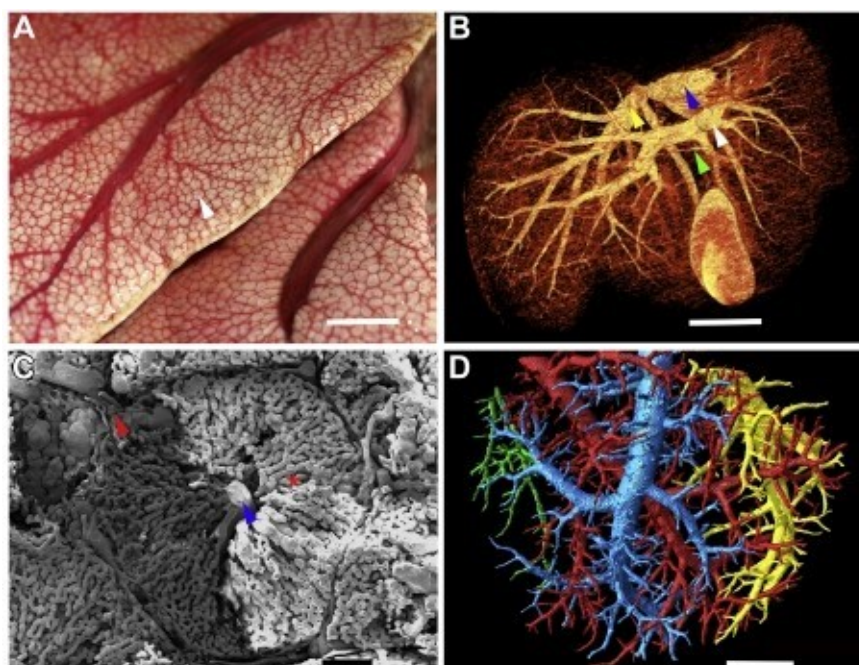


Fig. 2 a Vascular morphology of pig liver, Preslice Black-Pied breed. Filling with colored Biodur E20 via the hepatic artery (A-C) and portal vein (B-D). (A) Classical hepatic lobule (white arrowhead) before corrosion. (B) Macm-CT, volume rendering technique. Syntopic view of portal and hepatic venous systems; hepatic vein (yellow arrowhead), portal vein (white arrowhead), hepatic duct (green arrowhead), and caudal vena cava (blue arrowhead). (C) Classical hepatic lobule in scanning electron microscopy. Portal triad in porta (red arrowhead), sinusoids (red asterisk), and central vein (blue arrowhead).

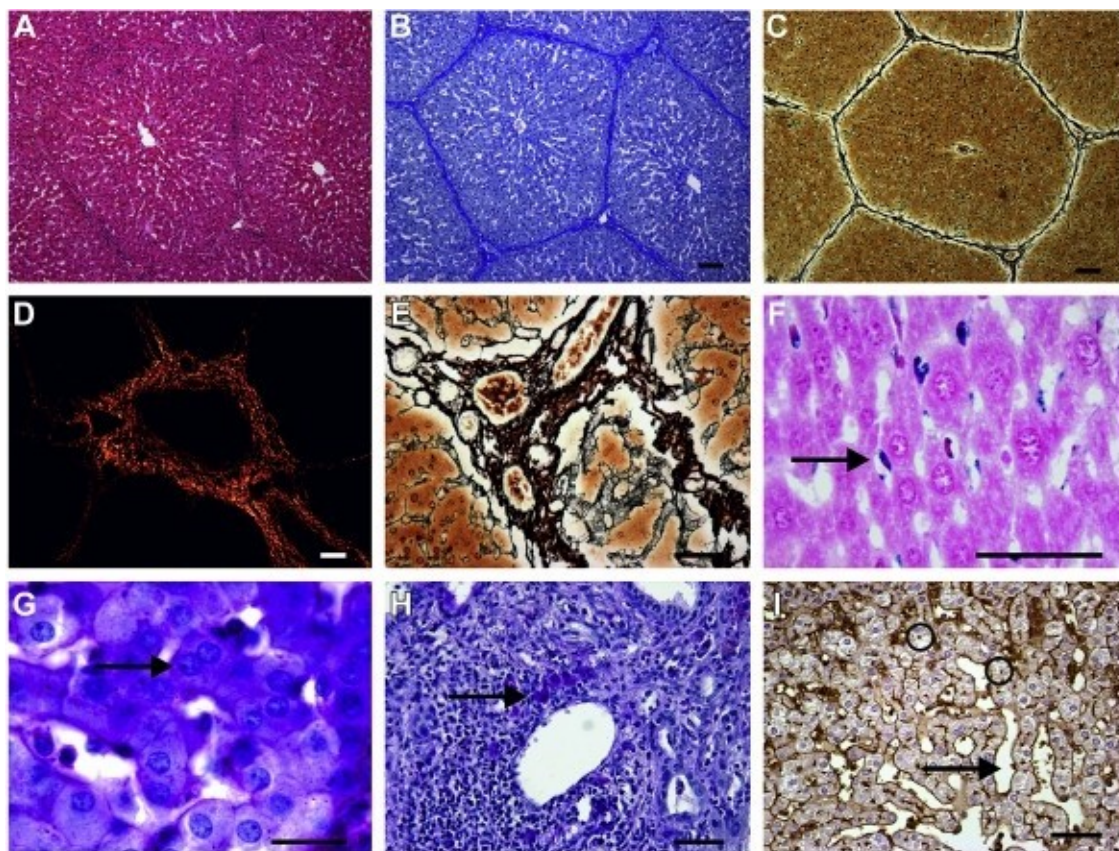


Fig. 3 - Pig liver histology in various histological staining methods. Hematoxylin and eosin staining (A), anilin blue counterstain with nuclear fast red: detection of collagen (B), Gomori reticulin staining: detection of reticular fibers (C, E), picrosirius red staining in polarized light: detection of collagen I and III (D), Periodic acid-Schiff staining (G, H), lectin histochemistry staining using Ricinus communis Agglutinin lectin I, (A-C) Demonstration of hepatic lobules clearly demarcated by connective tissue. (D, f.) Detail of portal space containing bile ducts and branches of hepatic artery and portal vein surrounded by connective tissue. (E, f.) Detail of portal space containing bile ducts and branches of hepatic artery and portal vein surrounded by connective tissue. (1) Hepatic stellate cells (arrow). (G) Binuclear hepatocyte (arrow). (H) Cluster of Kupffer cells after phagocytosis of cellular debris (arrow), a typical hallmark of hepatitis. (I) Discontinuous endothelium of hepatic sinusoids (arrow) and bile canaliculi formed by apical membrane of adjacent hepatocytes (arrows). Scale bars: 100 μ m. (A-C), 50 μ m. (D-I). (Color version of figure is available online.)

does not always correspond with the ploidy of HEPs.⁶² However, the morphometry and distribution of HEPs was not mapped with respect to their position within the classical morphological hepatic lobules and liver acini.⁶³ Data on lobular and acinar distribution would provide valuable information concerning the role of HEPs in pathological processes, which predominantly involve the acinar zones. In addition, an estimation of the total number of HEPs within the different lobes⁶⁴ would serve as a powerful tool for comparing the functional capacity and regenerative potential of the hepatic lobes after a partial hepatectomy.⁴⁷

The exocrine function of the liver, bile production, is morphologically represented by a delicate intralobular network of channels, bile canaliculi (Fig. 3I), which drain the bile into the interlobular bile ducts. Hepatic sinusoids (Figs. 2C and 39) are low-pressure vessels that lie between plates of HEPs and are lined by specialized endothelial cells and fixed macrophages called Kupffer cells (KCs) (Fig. 3H). The integrity of KCs has been linked to hepatocellular proliferation and

thus presumably plays a role in liver regeneration.⁶⁶ A recent study on the rat liver revealed that female rats have a greater number of HEPs and KCs and a larger fraction of binuclear cells than males.⁶³ These findings indicate a higher regenerative potential of the female liver. The stellate cells (Fig. 3F), which are also called Ito cells or fat-storing cells, are located in the perisinusoidal space (of Disse) between the HEPs and the sinusoids. They contain lipids that are involved in vitamin A metabolism and also play a leading role in fibrogenesis.⁶

In the pig, design-based stereology⁶⁴ (Fig. 4) has been demonstrated to be a powerful tool for assessing numerous morphological characteristics, namely, the number of HEPs and the amount of connective tissue within the porcine liver.^{36,37} Generating data on the morphometry and distribution of liver cells, together with the 3-D architecture of the vascular and biliary systems, could be the next step in understanding of liver function and pathophysiology and could increase the potential of successful xenotransplantation.⁶⁹ The evidence indicating that the liver is a sexually

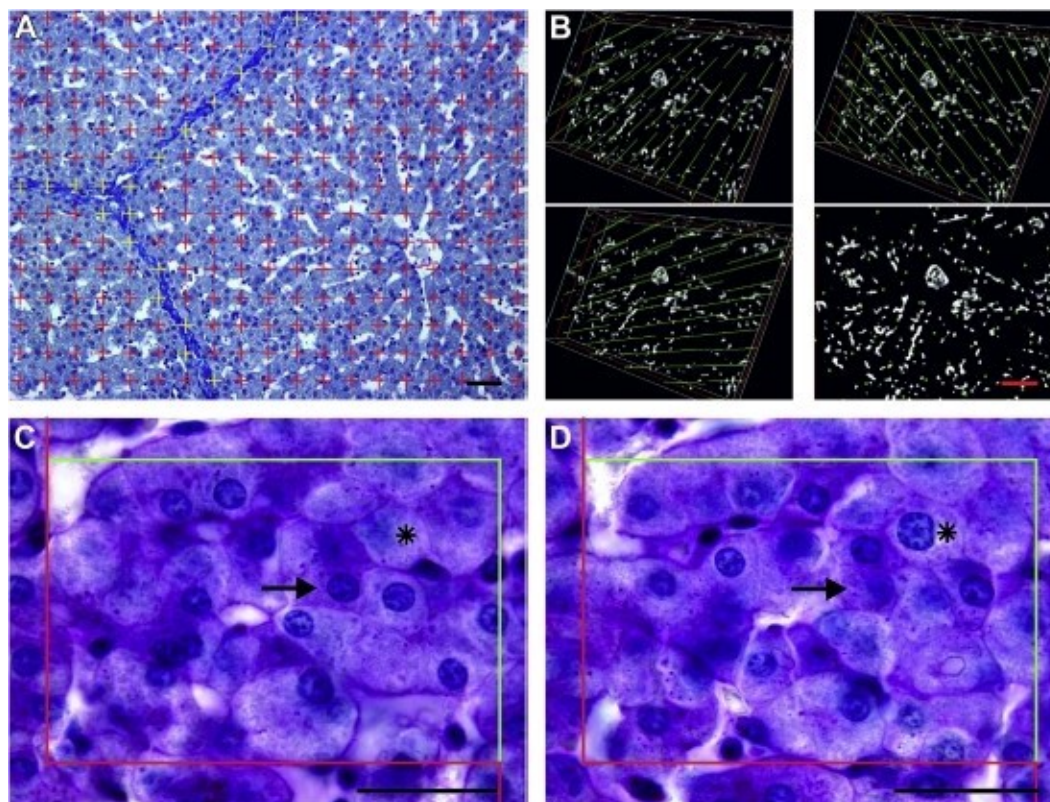


Fig.4 - Demonstration of stereological methods for quantitative assessment in porcine liver. Point grid⁶⁸ used for the quantification of the connective tissue & action, aniline blue with nuclear fast blue stain. Dig. A: points over the connective tissue within the predetermined area are highlighted in yellow (A). (B) Estimating the surface area of vessel in a series of μ -CT scans of vascular corrosion cast using the Fakir probe consisting of an isotropic grid with three differently oriented, perpendicular series of beams with random initial orientation. Length of the probe intersections with the microvessel profile is proportional to the surface area (B). Demonstration of optical disector for estimating the numerical density of hepatocytes in two optical sections (C, D). The cell profile with nucleus in focus in the bottom reference plane (C) and absent or out of focus in the look-up plane (D) that lies inside the counting frame at touch the green allowance bottom but do not touch the red forbidden border are counted (black arrow). The hepatocyte in focus in the look-up plane is not counted (marked with asterisk.) Scale bars: 50 μ m (A), 100 μ m (B); 20 μ m (C, D). (Color version of figure is available online.)

dimorphic organ warrants consideration in the planning of experiments."⁶³ Sufficient and systematic sampling is crucial for detecting the biological differences in liver tissue when studying liver regeneration, the pathophysiological mechanisms of liver diseases or the toxicity of drugs.⁶⁴

Liver connective tissue

Most types of chronic liver diseases lead to liver fibrosis and/or eventually to cirrhosis, that is, to the excessive accumulation of extracellular matrix, including fibrillar collagen. Staging and grading of liver fibrosis is a significant histopathological evaluation.⁶⁵ In the human, six specific foci of liver fibrogenesis have been proposed for scoring. Namely, the portal, pericellular (perisinusoidal), pericentral (perivenular), centrilobular, ductal (periductal), and ductular fibrosis can be distinguished.⁶¹ The type and extent of fibrosis describes both the architecture of connective tissue and its amount and

measures how far the liver disease has progressed to its end stage- liver cirrhosis. In addition, the grade of the liver disease reflects the speed at which the disease will progress to its end stage. The amount and the architecture of connective tissue in the human liver is usually estimated during routine analysis of liver biopsies, usually as part of the three most widely used scoring systems.⁶⁶ However, the subjectivity and hence the lack of reproducible results of this routine biopsy scoring have been articulated.

For the study of the mechanisms of origin and spread of fibrosis, and also to assess the liver regenerative capacity, both small and large animals are widely used. However, small animal models have limitations due to their size and differential susceptibility to toxic agents or pathogens.¹¹⁻¹⁵ A challenge in evaluating fibrosis using this model is that the normal rodent liver microscopically resembles fibrosis in the human; porcine liver lobules are clearly demarcated by the interlobular connective tissue septa that meet in the portal area (Fig. 3A-D). Moreover, according to the quantitative studies,

the distribution of intralobular and interlobular connective tissue in the healthy domestic pig varies with respect to sex and location within the liver.³⁷ In addition, the mean area fraction of the interlobular connective tissue is greater in male pigs; significant differences have also been found among individuals and liver lobes. Owing to the quantitative methods that provide us with objective and reproducible data, when both the sex of specimen and the position of the harvested tissue block are taken into account, more precise quantitative estimates can be achieved.^{31,44,45}

Corrosion casting

Perfusion is a key element to understand the physiology and regeneration of any organ. Because of having two blood inputs, liver perfusion is very complicated, and research is based on the analysis of the geometrical model of the vascular tree. To obtain the highest authenticity model of the 3-D vascular bed, vascular corrosion casts (VCCs) have been

used for many decades.^{52,53} Current casting materials are

able to fill the entire vascular bed, which needs to be preserved free from gas and blood clots. As it is almost impossible to obtain a human liver with these characteristics,¹⁸ the porcine liver model is irreplaceable.⁷⁹ The gap between 2-D histological studies and 3-D microarchitecture can be bridged using X-ray microtomography and micro-CT.³ Micro-CT data of liver VCC represent another source to provide microvascular morphometry.³³ Using differently colored resins in the VCC (Figs. 1C and O, 2A) is also useful for teaching anatomy, as it enables the student to distinguish the vascular (biliary) beds and differentiates fine structures that cannot otherwise be demonstrated.^{34,47}

Computer vision algorithms in pig liver research

To model liver anatomy and the processes in the liver parenchyma, it is necessary to create macroscopic and microscopic models of the vascular bed. Obtaining imaging data with the required resolution from human patients are not possible for technical reasons, so the porcine liver model is often used. Many kinds of software have been designed to

analyze images from 3-D imaging devices; most of them were developed with regard to clinical practice. For the specific requirements of pig liver anatomy research, however, special software needed to be developed.^{37,48}

To extract the shape of the liver parenchyma and the macroscopic model of the vascular system, macro-CT with a resolution of 1 mm was performed using pig liver corrosion casts (Fig. 28). Segmentation of the liver parenchyma by the macro-CT was performed interactively by the modified graph-cut algorithm⁴³ available in the Lisa application.^{37,112} The pre-processing was carried out by resampling to a voxel size of 2 mm. Voxels representing the subject of interest (e.g., liver parenchyma) and background (other tissues) were selected. Of these, an intense Gaussian mixture model with three foreground and background components was created. Vascular bed segmentation was performed by a modified connected threshold algorithm. In postprocessing, binary morphological operations were applied. Extraction of the microvascular bed geometry was performed using the image data acquired from micro-CT with a resolution of 211 μm (Fig. 20). For the flow

modeling and the vascular bed quantitative description, the

software Quantan can be used.³³ To estimate the radius, length, tortuosity, and branching angles. The application also enables the evaluation of the number of microvessel segments, the volume fraction, as well as the surface and length densities. Semiautomatic subtraction facilitates the evaluator's work and allows for more precise estimates.

Challenges and pitfalls of pig liver utilization in biomedical research

The domestic pig as an experimental animal was critical to many of the key shifts in research on serious human diseases. Although the detailed knowledge of (micro) anatomy is crucial both for designing and evaluation of most experiments, it is interesting that very few breed-related and/or gender-sensitive studies have been published on the anatomy of porcine organs yet. For this reason, we found useful to summarize the current knowledge of (micro) anatomy of the porcine liver to point out critical points in planning and assessment of studies conducted in this animal model (Table 4). Given the size of porcine organs and vast biological

Table 4 Morphological differences between the normal porcine and human liver, based on Prestige Black-Pied pig breed.⁴⁸ and sometimes IV.⁸⁵

Gross anatomy

Pig: Deep 6ssures marking well-marked lobation, right and left hemiliver divided by the notch for ligamentum teres.⁷⁹
Human: External lobation does not correspond to the functional (i.e. surgical) anatomy: three main 6ssures are not visible on the surface and contain three main hepatic veins; they divide the liver into four porta! sec tors; right and left: hemiliver divided by Cantlie's line.

Pig: Superficial, extraparenchymal portal vein (PV) lobar branching visible from the visceral surface (Fig. 10), the caudal caval vein runs through the left lateral lobe.
Human: PV divides into the right and left branches at the hilum; only the left PV invariably gives extraparenchymal branches to segment I

Histo logy

Pis Inegular, rather pentagonal hepaticlobules{Fig. 2A} clearly demarcated by connective tissue septa{Fig. 3AeC}.
Caution, normal porcine liver microscopically resembles fibrosis in the human; more connective tissue in males.³⁷

Hum.an: Roughly hexagonal hepaticlobules,⁶¹ no interlobular septa, connective tissue found in interlobular space.⁸⁵

variability, it is clear that morphological studies cannot be carried out without the use of stereological procedures.⁶⁸ Unbiased stereology also allows for setting up sampling optimization—the latest studies revealed different tissue struc-

ture depending on the sampling location.^{3, 1.M} These

procedures can be advantageously used also for evaluation in imaging methods such as (micro)CT or magnetic resonance imaging.¹¹

In experimental medicine, the pig liver is preferably used as a large animal model of acute liver disease and/or liver failure as it is suitable for extracorporeal circulation, repetitive blood sampling, and training of surgical techniques applicable to humans, for example, partial hepatectomies, orthotopic liver transplantation, or PV arterialization.⁸⁷ Unlike small animals, experiments on pigs and other large animal models

are limited because of technically demanding treatment and higher financial costs that result in smaller cohorts, which due to considerable interindividual variability makes statistical evaluation and interpretation of results difficult.

Conclusions

A variety of modern pig breeds are available today, and they have been increasingly used in biomedical research. Despite recent efforts to obtain detailed knowledge of pig liver macroanatomy and microanatomy, very little is still known in accordance with biological variability, and certain issues need to be addressed for the appropriate translation of animal observations to clinical testing. Quantitative results based on stereology guarantee unbiased estimates that are able to reveal even subtle histological changes, and it is also possible to optimize the algorithm for study designs in accordance with sex, breed, or position of the harvested tissue block. Newly developed software is able to process data obtained from (micro)CT for 3-D reconstructions, quantitative estimations, and morphometrics, which is highly consistent with manual counting techniques. Volumetric data extracted from computer imaging methods can be used to model liver perfusion and optimal liver resection.

Acknowledgment

Funding sources: This work was supported from European Regional Development Fund, European Union-Project "Application of Modern Technologies in Medicine and Industry" [grant number CZ.02.1.01/0.0/0.0/17_048/0007280], by Charles University in Prague, Czechia [grants SvV number 260390 and 260392 and GAUC number 1206417]; Research Fund Progress [grant Q39] and by the Center of Clinical and Experimental Liver Surgery [grant UNCF/MED/006]. Micro-CT scanning was supported by the Ministry of Education, Youth and Sports under the National Sustainability Program I [projects CENTEM number CZ.1.05/2.1. March 00, 0088, CENTEM PLUS number L01402 and L01503 and Program I (NPU I) No. L01503).

Author contribution: Eberlova Lada contributed the main

Mik Patrik cowrote the article; and Tonar Zbynek provided critical revision and helped shape the manuscript. Palek Richard carried out literature research and analysis; Sarah Leupen performed language proofreading; Jirik Miroslav co-

wrote the article; Mirka Hynek provided CT scans and hel-

ped shape the manuscript; and Liska Vaclav provided critical revision and helped shape the manuscript.

Disclosure

The authors reported no proprietary or commercial interest in any product mentioned or concept discussed in this article.

REFERENCES

conceptual idea and wrote most of the article; Malec.kova Anna cowrote the article and provided histological figures; 1.

- Larson C, Dobney K, Albarena U, et al. **Worldwide phylogeography of wild boars reveals multiple centers of pig domestication.** *Science*. 2005; 307:1618-1621.
2. **Bustad LK, McClellan RO.** Swine in biological research. *Science*. 1966; 152:1526-1531.
 3. **Born, eds.** The Pig Site. Available at: <https://thepigsite.com/>. Accessed March 21, 2019.
 4. **Swindle MM.** Swine in the laboratory: surgery, Anesthesia, imaging, and experimental techniques. 3rd ed. Boca Raton, FL: CRC press; 2016.
 5. **Groenen MAM, Anilubald AL, Uenishi H, et al.** Analyses of pig genome, provides insight into porcine demography and evolution. *Nature*. 2012; 491:393-398.
 6. **Pearleberg C, Kind A, Schinabel A.** Genetically engineered pigs as models for human disease. *Dis Model Mech*. 2018; 11. <https://doi.org/10.1241/dmm030783>
 7. **Lossi L, D'Angelo L, O. Girolamo P, Morigi A.** Anatomical features for an adapted cholelithiasis in the small laboratory rodents, rabbit, and pig. *Ann Anat*. 2016; 204:11-28.
 8. **Liska V, ed.** Experimental Surgery. **Pfizer**: Nava Publishing; 2016.
 9. **Jiang K, Chen J, Liu Y, et al.** Heat-irrigation effect of radiofrequency ablation on relevant regional hepatocyte in living swine liver-initial study on pathology. *Cell Biochem Biophys* 2015; 72:37-41.
 10. **Dong J, Geng X, Yang Y, et al.** Dynamic imaging and pathological changes in pig liver after MR-guided microwave ablation. *BMC Cancer*. 2018; 18:397.
 11. **Smolock AR, Cristescu MM, Vlaisavljevich E, et al.** Robotically assisted sonar-guided noninvasive nonthermal ablation modality: proof of concept in a porcine liver model. *Radiology*. 2018; 287:485-493.
 12. **Wax C, Ston A, Frohlich M, Arndts, Lippert H.** How precise is time change, the linear viscoelastic properties of porcine liver. *Biorheology*. 2013; 50:115-131.
 13. **Wax C, Ston A, Frohlich M, Arndts, Lippert H.** Mechanics of fresh, frozen, thawed and heated porcine liver tissue. *Int J Hypertension*. 2014; 30:271-283.
 14. **Camacho O, Sandoval L, Montalva E, et al.** A surgical model for isolating the pig liver in vivo for gene therapy. *Surrg Res*. 2013; 51:47-57.
 15. **Kang HY, Choi Y-K, Jeong YI, et al.** Immortalization of porcine 11beta-hydroxysteroid dehydrogenase type 1-transgenic liver cells using SV40 large T antigen. *Int J Mol Sci*. 2017; 18:2625.
 16. **Xiberta P, Boada I, Bardera A, Font-i-Furnols M.** A semi-automatic and an automatic segmentation algorithm to remove the internal organs from live pig CT images. *Comput Electron Agric*. 2019; 140:290-302.


- V. L--T, Xu D-X, Tian C, et al. Value of two-dimensional shear wave elastography for assessing acute liver congestion in a bama mini-pig model. *Di9 Ois Sá.* 2018;63:1851- 1859.
18. Court R.; Laws P, Morrison CP, et al. Subtotal hepatectomy: a porcine model for the study of liver regeneration. *J Sllr9 Res.* 2004;116:181- 186.
19. Clowka TR, Standop J, Paschenda P, Czaplik M, Kalff JC, Tolba RH. Argon and helium plasma coagulation of porcine liver tissue. *J Int Mal Res.* 2017; 45:1505- 1517.
20. Vrochides D, Kardassis D, Ntinias A, et al. A novel liver parMchyma transection technique using locking straight rigid ti<,s. M experimental study in pigs. *J Inuest Sur9.* 2014;27106- 113.
21. Zhang Z-B, Gao W, Liu L, Shi Y, Ma N, Shen Z-Y. Development and assessment of nonthohennic machin!! pl.rfu.sion preservation for e.xtracorporeal splitting of pig liver. *Ann 'l)-4nspldnt.* 20V ;22:507-5 17.
22. Okada N, Mlzuta K, Oshima M. et: al A novel split liver protocol using the subnonothtmk:oxygi!nat circuit system in a porcine model of a marginal donor pr ure. 'l)-4nspldnt Proc. 2015;47:419-4 26.
23. Vogel T, Broclanann JG, Pigott O, et al. Suca,ssful transplantation of pordne liver grafts fi:>llowing 48.hour nonthohtm.ic precseNation. *PLoS One.* 2017;12:e<188494.
24. Louras N, Patel M, Shah J, Sachs O, Vage J P. Biochemistry profile, s following pig.to.nonhuman primate liv« xe.notransplanta tion. *AmJ Transplanta nt* 2018;18:763- 764.
25. Detennan C, And«son R. Beck« A, et al. F state prior to h orrhagicshod: andpolytrauma in a porcine model recsults in altered livitt transcriptom.ic response. *PLoS Orte.* 2014 :e10008&
26. Fröhlich M, Hildebrand F, Weuster M, et al Induced hypothennia re,duces the hepatic inflammatory response in a @ multipl@ tr.luma mod@l. *Jn-auma kutt Cdrt SUR9.* 2014;76:1 425- 1432.
27. E:schbach D, Horst K, Sassen M, et al. Hypothermia does not infuene liv« damagi!and function in a porci.ne polytrauma modol. *Te<hno! Health Cdre.* 2018;26:209- 221.
28. Mylonas AI, Orfanos NF, Karmanioliou O, et al. Th• effects of h orrhagicshod: secondary to hepatectomy in a swine modol. *J SUR9 Res.* 2015;195:228- 234.
29. Tao L, Li Q, Ren H, et al. Repair of extrahepatic bile duct defe<:t using a collagen patch in a Swine model *Arti/ Orga.ns.* 2015;39352- 360.
- D. Tana.ta H, Fuku.shima K, Srinivasan PK, et al. Dñcacy of the novel med.kal adhesi!l1, MAR·VIV0·107, in an acute porcine liver resection model *Surg tnnou.* 2017;2423-431.
31. FU VB, Chul CK. **Mod.Oing** and simulation of pon:in• liver tissue indentation using finiteelement method and uniaxial stre,ss-strain data. *J Biomedt.* 2014;47:2430- 2435.
32. Krlillčl:ová A, Eberlová L, Kalusová K, et al. Q.uantification of liver microci.rculation using x.ray microtomography of vascular corrosion casts. *Key tn9 Mater.* 2014;592:505- 508
33. Jifll: M, Tonar Z, Krállčl:ová A, et al. Ste,eological quantification of microvessels using se.m.iautomat evaluation of x.ray microtomogra.phy of hepatic vascular corrosion casts. *Int)Comput Assist R4di.ol SURg.* 2016;1119:>3- 1819 .
34. Eberlova L, Liska V, Mirka H, et al Th• use of pon:in• corrosion casts fi:>reacŧung human anatomy. *Ann Anat.* 2017;21369- 77.
35. Bekheit M, Bucur PO, Wartenbe,g M, Vibert E. Computeritt tomography-based anatomic description of the porcine liv« . *J Sur9 Res.* 2017;210:223- 23:l.
36. Junatas KL, Tonar Z, Kubll:ová T, et al. Ste,eological analysis of size and den.sity of hepatocytes in the porcine liver. *J Ana.t.* 2017;230575- 588
37. Mik P, Tonar Z, Malečková A, et al. Distribution of coMect.ive tissue in the male and female porcine live.r: histological mapping and re<:ommendations fi>r sa mpling . *J Comp Pathol.* 2018;162:1- 11
38. **Rogée S, Le Cali M, Chafey P, et al.** Quantitative proteom.ics identine, s host factors modulatu.ring acute hepatitis E: virus infection in the swine model *J Vlrol.* 2015;89129- 143.
39. Wang J, Sun Z, Jiang J, et al. Proteomic signarure of acute liver failure: f.rom discove ry and veri.fication in a pig model to confi.rmat ion in humans. *Mol CeD Prot a:>mics.* 2017;161 188- 1199.
40. tiska V, fуска V, Mirka H, et al. Inhlbition of transforning growth factor beta •l augments liverre,generation after partial porta! vein ligation in a porcine e.xperimetal model *Hepa09astroentero09y.* 2012;59235- 240
41. Yu R, Zhang Y, Lu Q, et al Differentially expn,ssed genes in n,spn,sto cyadox in swine liver analyzed by OORT-PCR. *Res Vet Sá.* 2018;118:72- 78.
42. Swindle MM, Malcin A, Herron AJ, Clubb FJ, Frazier KS. Swine as models in biomedical research and toxicology testing. *Vet Pnthol.* 2012;49:344- 356.
43. **IH KS, Santagostino SF, Li o, et al.** Catheter-<irected intr. lportal delivery of endothelial cen therapy for liver re,generation: a feasibility study in a large animal vodel of clrrhosis. *R<diol 09y.* 2017;28514- 123.
44. Bartas M, CeNen J, Oppelt J, et al. liv« regen«ation du.ring the associating liv« partition and porta! vein ligation for stagi!d hepatectomy procedure in *Sus scrofa* is positively modulated by stem c.Os. *Onool Lett* 2018;156309- 6 321.
45. m.ipponi F, Leoncini C, Campatelli A, et al segmental organization of the pig liver: anatom.ical basis of controUed partition for@xperimetal gmlting. *IUI Surg RIIS.* 1995;27 :151- 157.
46. Liska V, Tn>ska V, Mirka H, et al. Interleucin-6au ents activation of l.iver regi!neration in porcine model of partial porta! ve.in ligation *Antica.ncer Res.* 2009;9:2371 2377.
47. Bruha/, Vycital O, Tonar Z, Mirka H, Haidingerova L. Monodonal antibody against transforming growth factor beta 1 does not influence liv«iecg!neration after re,section in large animal experiments. *tn Vluo.* 2015;340:327- 340.
48. Vrtková I. C.netic admixture analysis in pn,stic•black-pied pigs. *Arch Anim Breed.* 2015;58:115- 121.
49. K Onig Ha Liebich HC, eds. Anatomie doma. Och *sauc-u, 2. díl.* Bratislava : H & H; 2013:70- 76.
50. Court FC, Wemyss- Holden SA, Morrison CP, et al. S.gmental naru..re of the porcine liv« and its potential as a model fi>rexperimetal partial hepatectomy. *Br J Sur9.* 2003;90:440-444.
51. Witter K, Tonar Z, SChOpp« H. How many la'!l.rs has the adventitia? Structu.re of the artttial runicae.xterna revisited. *Mdt Hi.stol Embryo!* 2017;46110- 120.
52. Lehmann KS, Ritz J-P, **Valdeig S, et al.** Porta! vein segmentation of a 30.planning sy-stem fi:>r l.iver sur gery- in vivo evaluation in a porcine model *Ann SURg Onc-ol.* 2008.15:1899- 1907.
53. Zanehet OJ, Montero E:F. Pig liv«ecrorization and segmentation and virtual reality depiction. *Arta Cir Bras.* 2002;17:381- 387.
54. Couinaud C. (Liver lobes and segments: notes on the anatom.ical architecture and surgi!ry of the live.r. *J. Presse Med.* 1954;62 :709- 712.
55. Martins AC, Machado MA, Fena.z M. Porcine live.r: experimental model for the intra,hepatic glissonian approach . *kfl!l Cir BrdS.* 200!;23:204- 207.
56. Nykonenko A, Vavra. P, Zonca P. Anatomie peculiaritiec of pig and human liver. *Clin Trd Idnt* 2017;25- 26

57. D'Inys A, Prior J, Bize P, et al. Portal vein embolization: what do we know? *Cardiovasc Intervent Radiol*. 2012;35:999-1008.
58. E'kata.ksin W, Wa.ke K. Liver units in three dimensions: I. Organization of argyrophilic connective tissue skeleton in porcine liver with particular reference to the "compound hepatic lobule". *Am J Anat*. 1991;191:113-153.
59. Rappaport AM, Wilson WD. The structural and functional unit in the human liver (liveracinus). *Anat Rec*. 1958;130:673-689.
60. Lamers WH, Hilberts A, Furt E, et al. Hepatic enzymic zonation: a reevaluation of the concept of the liveracinus. *Hepatology*. 1989;10:72-76.
61. Saxe R. *Practical Hepatic Pathology: A Diagnostic Approach* 2nd ed. Philadelphia, PA: Elsevier; 2018.
62. Tanami S, Ben Moshe S, Elkayam A, Mayo A, Sahar Halpern K, Itzkovitz S. Dynamic zonation of liver ployploidy. *Cell Tissue Res*. 2017;368:405-410.
63. Marcos R, Lopes C, Malhó F, et al. Stereological assessment of sexual dimorphism in the rat liver reveals differences in hepatocytes and Kupffer cells but not hepatic stellate cells. *J Anat*. 2016;228:996-1005.
64. Marcos R, Montanari RAF, Rocha E. The use of design-based stereology to evaluate volume, mass and number in the liver: a review with practical guidelines. *J Anat*. 2012;220:303-317.
65. Liška V, Treska V, Mirka H, et al. Preoperative use of biological therapy does not influence liver regeneration after large resection - porcine experimental model *Tumor Biol*. 2012;33:102-103.
66. Yang K, Du C, Cheng Y, Li Y, Cong J, Liu Z. Augmentation of liver regeneration promotes hepatic regeneration depending on the integrity of Kupffer cells in rat small for size liver transplantation. *J Surg Res*. 2013;183:922-928.
67. Puche JE, Saiman Y, Friedman SL. Hepatic steatosis and liver fibrosis. *Compr Physiol*. 2013;3:1473-1492.
68. Mouton PR. *Principles and Practice of Unbiased Stereology: An Introduction for Biologists*. Baltimore, MD: Johns Hopkins University Press; 2001.
69. Cooper DKC, Ayares D. The immense potential of xenotransplantation in surgery. *Int J Surg*. 2011;9:12:2-129.
70. Toosi A, K. Liver fibrosis: causes and methods of assessment, a review *Rom J Intern Med*. 2015;53:304-314
71. Sattis KP, Ludwig J. Chronic hepatitis. An update on terminology and reporting. *Am J Surg Pathol*. 1995;19:1409-1417.
72. La dossa P, Dargère D, Paradis V. Sampling variability of liver fibrosis in chronic hepatitis C. *Hepatology*. 2003;38:1449-1457.
73. D'Angelo L, Lossi L, Merighi A, de Cirolamo P. Anatomical features for the adequate choice of experimental animal models in biomedicine: I. Fishes. *Ann Anat*. 2016;205:75-84.
74. O. Jin, B. Starke! P, Leden: q I. Animal models for fibrotic liver diseases: what we have, what we need, and what is under development. *J Clin Transl Hepatol*. 2015;3:53-6.
75. Starke! P, Uelen: q IA. Animal models for the study of hepatic fibrosis. *Seest Pract Res Clin Gastroenterol*. 2011;25:319-333.
76. Tschanz S, Schneider JP, Knudsen L. Design-based stereology: planning, volumetry and sampling are crucial steps for a successful study. *Ann Anat* 2014;196:3-11.
77. Lametschwandtner A, Lametschwandtner U. Historical review and technical survey of vascular casting and scanning electron microscopy. In: *Scanning Electron Microscopy of Vascular Casts: Methods and Applications*. Electron Microscopy in Biology and Medicine. Boston, MA: Springer; 1992:1-11.
78. Debbaud C, Sagers P, Comillie P, et al. Analyzing the human liver vascular architecture by combining vascular corrosion casting and micro-computed tomography: a feasibility study. *J Anat* 2014;224:509-517.
79. Eberlova L, Listá V, Mirka H, et al. Porcine liver vascular bed in Biodur E20 corrosion casts. *Biologia Morphol*. 2016;75:154-161.
80. Schladitz K. Quantitative microscopy. *J Microsc*. 2011;243:111-117.
81. Pálek R, Liška V, Eberlova L, et al. [Experimental processing of corrosion casts of large animal organs]. *Rozh. I Oifir*. 2018;97:222-228.
82. Lisa JM. Computer-assisted liver surgery. 2018. Available at: <http://github.com/mjirik/lisa> Accessed July 31, 2018.
83. Boykov VY, Jolly MP. Interacti"saph cuts for optimal boundary and region segmentation of objects in N-D images. In: *Proceedings of the 9th IEEE International Conference on Computer Vision*. ICCV 2001. Vol. 1. 2001:105-112. <http://doi.org/10.1109/ICCV.2001.937505>.
84. Tomášel: P, Tonar Z, Grajciarová M, et al. Histological mapping of porcine carotid arteries - an animal model for the assessment of arterial conduits suitable for coronary bypass grafting in humans. *Ann Anat*. 2019;228:151434.
85. Bech), Clud AN, Sangi D R, et al. The porcine corticospinal decussation: a combined neuronal tracing and tractography study. *Brain Res Bull*. 2018;142:253-262.
86. Standring S. *Cray's Anatomy: The Anatomical Basis of Clinical Practice*. 41st ed. China: Elsevier Limited; 2016:1166-1170.
87. Malea:ová A, Tonar Z, Mil: P, et al. Animal models of liver diseases and their application in experimental surgery. *Rozh. I Chir*. 2019;8:100-109.

Příloha III:

JUNATAS, Khan L., Zbyněk TONAR, Tereza KUBÍKOVÁ, Václav LIŠKA, Richard PÁLEK, Patrik **MIK**, Milena KRÁLÍČKOVÁ a Kirsti WITTER, 2017. Stereological analysis of size and density of hepatocytes in the porcine liver. *Journal of Anatomy* [online]. 230(4), 575–588. ISSN 1469-7580. Dostupné z: doi:10.1111/joa.12585. **IF₂₀₁₇=2,182, Q1_(Anatomy & Morphology)**•

Stereological analysis of size and density of hepatocytes in the porcine liver

Khan L Juna t as,^{1,2} Zbyněk Tonar,³  Tereza Kubíková,⁴ Václav Liška,⁵ Richard Pálek,⁵ Pa t rik Mik,⁶ Milena Krá líčková³ and Kirsti Wi t ter¹

¹ Department for Pathobiology, Institute of Anatomy, Histology and Embryology, University of Veterinary Medicine Vienna, Vienna, Austria

² College of Veterinary Medicine, University of Southern Mindanao, Cotabato, Philippines

³ Department of Histology and Embryology and Biomedical Center, Faculty of Medicine in Pilsen, Charles University in Prague, Pilsen, Czech Republic

⁴ NTIS, European Centre of Excellence, Faculty of Applied Sciences, University of West Bohemia, Pilsen, Czech Republic

⁵ Department of Surgery and Biomedical Center, Faculty of Medicine in Pilsen, Charles University in Prague, Pilsen, Czech Republic

⁶ Department of Anatomy, Faculty of Medicine in Pilsen, Charles University in Prague, Pilsen, Czech Republic

Abstract

The porcine liver is frequently used as a large animal model for verification of surgical technique as well as experimental therapies. Often, a histological evaluation is required that include measurements of the size, nuclearity or density of hepatocytes. Our aims were to assess the mean number-weighted volume of hepatocytes, the numerical density of hepatocytes, and the fraction of binuclear hepatocytes (BnHEP) in the porcine liver, and compare the distribution of these parameters among hepatic lobes and macroscopic regions of interest (ROIs) with different positions related to the liver vasculature. Using disector and nucleator as design-based stereological methods, the morphometry of hepatocytes was quantified in seven healthy piglets. The samples were obtained from all six hepatic lobes and three ROIs (peripheral, paracaval and para portal) within each lobe. Histological sections (thickness 16 μm) of formalin-fixed paraffin-embedded material were stained with the periodic acid-Schiff reaction to indicate the cell outlines and were assessed in a series of 3- μm -thick optical sections. The mean number-weighted volume of mononuclear hepatocytes (MnHEP) in all samples was $3670 \pm 805 \mu\text{m}^3$ (mean \pm SD).

The mean number-weighted volume of BnHEP was $7050 \pm 2550 \mu\text{m}^3$. The fraction of BnHEP was $4 \pm 2\%$. The numerical density of all hepatocytes was $146\,997 \pm 15\,738 \text{ cells mm}^{-3}$ of liver parenchyma. The porcine hepatic lobes contained hepatocytes of a comparable size, nuclearity and density. No significant differences were identified between the lobes. The peripheral ROIs of the hepatic lobes contained the largest MnHEP with the smallest numerical density. The distribution of a larger MnHEP was correlated with a larger volume of BnHEP and a smaller numerical density of all hepatocytes. Practical recommendations for designing studies that involve stereological evaluations of the size, nuclearity and density of hepatocytes in porcine liver are provided.

Key words: animal model; disector; liver surgery; morphometry; nucleator; pig; stereology; swine.

Introduction

Porcine liver in experimental surgery

Human hepatobiliary surgery has achieved substantial progress in previous decades (Kwon et al. 2015; Song, 2015;

Parie et al. 2016). Operations such as extended resections, stage procedures and transplantations would not be possible without previous preclinical research. Procedures necessary for experimental verification of newly developed surgical techniques cannot be evaluated in small animals because they lack anatomical and physiological similarities to the human organism. The porcine liver is currently the best described and most suitable large animal model of the human liver in terms of organ size as well as gross and microscopic morphology and physiology (Court et al. 2003;

Correspondence

Zbyněk Tonar, Department of Histology and Embryology, Faculty of

Medicine in Pilsen, Charles University in Prague, Karlovo náměstí 48/301, 66 Pilsen, Czech Republic. T: +420 37 7593320 E: zbynek.tonar@lfp.cvri.cz

Accepted for publication 22 November 2016
Article published online 19 December 2016

Arkadopoulos et al. 2011). The major difference between the microscopic morphology of porcine and human liver is that porcine liver has much more defined interlobular connective tissue septa. The use of pigs as the last step of pre-

clinical research prior to designing clinical trials is done not only for newly suggested surgical procedures but also in pharmacological research on liver excretory, detoxification and synthetic functions important for liver regeneration following a partial hepatectomy (Liska et al. 2012; Bruha et al. 2015). Similarly, the porcine liver is used in surgical experiments regarding therapy of small-for-size injuries that occur after partial liver transplantation or extended hepatectomy (Kelly et al. 2009; Hessheimer et al. 2014). The porcine model has been demonstrated to be useful when examining histological alterations of the liver during carbon dioxide pneumoperitoneum (Alexakis et al. 2008). Moreover, the porcine liver is used as a model for drug-induced liver failure (Newsome et al. 2010) a model for hepatectomy with portocaval shunt (Iida et al. 2007), or for hepatic electrolyte ablation (Gravante et al. 2012).

The porcine liver has been suggested as a source of hepatocytes for bioartificial liver devices (Nicolas et al. 2016) and xenografts for transplantation (Cooper et al. 2015); however, these applications are controversial (Wang & Yang, 2012). Nevertheless, there is promising research on decellularized porcine hepatic lobes used for liver bioengineering (Hussein et al. 2015) in which porcine tissue scaffolds are supposed to be recellularized by human hepatocytes (Wu et al. 2015). Recently, Bahr et al. (2016) evaluated samples of liver and other organs in transgenic pig that introduced a recombinant protein that may be capable of modifying the T-cell-mediated rejection process, thus controlling cellular rejection in xenotransplantation.

Historical quantification of hepatocytes

Studies on pathophysiological mechanisms of liver diseases, liver regeneration, efficacy and toxicity of drugs, and evaluation of surgical techniques often require quantification. Numerous morphological characteristics may be estimated, preferably using design-based histological techniques (Moutai, 2002; Howard & Reed, 2005) that make no further assumptions regarding the orientation or shape of liver cells and other structures under investigation (Marcos et al. 2012). The quantitative parameters of the liver that have been assessed in the frame of different studies include the whole liver volume, the volume densities of organ constituents (particularly of connective tissue), the mean volume of hepatocytes and other liver cells, the total numbers of liver cells and their numerical density per volume unit (Jack et al. 1990; Karbalay-Doust & Noorafshan, 2009; Marcos et al. 2016). Knowledge regarding the variability of these microscopic parameters within the porcine liver is required for correct histological sampling.

The volume fractions of hepatocytes within the liver and the numerical density of mononuclear hepatocytes (MnHEP) or binuclear hepatocytes (BnHEP) assessed by stereological methods have been published for mice, rats and humans (Altunkaynak & Ozbek, 2009; Karbalay-Doust

& Noorafshan, 2009; Odaci et al. 2009). Marcos et al. (2016) quantified hepatocytes, Kupffer cells and hepatic stellate cells in the rat liver, thereby combining the advantages of stereology with cytometric analysis of cell ploidy. However, other methods and techniques have also been used for the quantification of hepatocytes, namely, automated image analysis, cell proliferation assays, protein concentration measurements, DNA content methods and cytochrome P450 content methods (Carlisle et al. 1997; Stegemann et al. 2000; Haga et al. 2005; Schlenius-Stenbeck, 2006; Oeng et al. 2009; Miyaoka et al. 2012; Garrido et al. 2013; Best et al. 2015; Asaoka et al. 2016). Many of these techniques are based on the use of single cell suspensions or liver homogenates. An unbiased measurement of the fraction of MnHEP and BnHEP is important for correcting methods that estimate the hepatocellularity using DNA or protein contents (Marcos et al. 2007).

Aims of the study

To the best of our knowledge, no published data exist regarding quantitative histological parameters that demonstrate the normal interindividual variability in the size and density of hepatocytes in various macroscopic regions of porcine liver lobes, e.g. peripheral regions vs. the parenchyma located near the porta hepatis or adjacent to the caudal vena cava.

Therefore, our aim was to assess the number-weighted volume of hepatocytes, the numerical density of hepatocyte and the fraction of binuclear hepatocytes (subsequently abbreviated as 'nuclearity') in the porcine liver. These data were compared between the anatomical hepatic lobes as well as between three macroscopic regions with different positions related to the liver vasculature (region of interest, ROI): the peripheral regions of the liver lobe, the regions near the porta hepatis and the regions adjacent to the caudal vena cava.

Materials and methods

Animals

Uterine samples were obtained from seven healthy Prestige Blanc-Pied pigs (Vrtkova, 2015) aged 12 weeks and weighing 25–25 kg (35.7 ± 6.1 kg, mean ± SD). Five piglets were male and two female. The number of animals corresponds to the typical number of individuals in other studies using pig as an animal model in surgery (Damis et al. 2015; Hazelton et al. 2015). The animals received humane care in compliance with the European Convention on Animal Care, and the project No. 27374/2011/30 was approved by the Faculty Committee for the Prevention of Cruelty to Animals. The piglets were pre-medicated intramuscularly with atropine 1.0 mg, ketamine 200 mg (5–10 mg kg⁻¹) and azaperone 160 mg (2–8 mg kg⁻¹). For general anaesthesia propofol and fentanyl were continuously administered through a peripheral or central venous catheter in the following total average doses: propofol (1% mixture

5-10 mg kg⁻¹ h⁻¹ and fentanyl (1-2 µg kg⁻¹ h⁻¹). The piglets received infusion and volume substitution when necessary (Plasmalyte; Baxter, Vienna, Austria, and Gelofusine; B-Braun/Maria Enzersdorf, Austria, respectively). All surgical procedures were performed under aseptic and antiseptic conditions. The animals were sacrificed during deep general anesthesia via an intravenous administration of acardioleptic solution (potassium chloride).

Immediately after sacrifice, the whole liver was removed. The volume of each freshly collected liver was measured using the water displacement method. A large graduated cylinder with a total volume of 3 L was filled with water precisely to the 1-l mark, and the liver was fully submerged in the water. The liver volume was calculated by subtracting the water level before and after submersion. The liver volumes ranged from 640 to 910 ml and the mean ± SD values were 813 ± 85 ml (see Supporting Information Table S1 for details). The liver volume did not correlate with the body weight.

Tissue sample collection

Each liver was sectioned into 1-cm-thick slabs. The slabs were fixed with 10% buffered formalin. From each liver, 36 tissue probes (each approximately 25 × 25 × 25 mm) were sampled. Each of the six hepatic lobes (left lateral, right lateral, right lateral right medial, caudate and quadrate lobes) were represented by six probes. Within each lobe, three ROIs with different positions relative to the liver vasculature were sampled: two probes represented the peripheral region, two probes represented the paracaval region, and two probes represented the parportal region according to Fig. 1. The peripheral regions were defined as located no more than 1 cm from the surface and periphery of each hepatic lobe. The paracaval localization was the region of each lobe immediately adjacent to the openings of the hepatic veins into the caudal vena cava. The parportal (hilar) localization was immediately adjacent to the main branches of the portal vein following from the hilum within each anatomical lobe. In total, 251 tissue probes were collected (one sample was lost during processing).

The orientation of each tissue block was randomized using the orientation scheme (Mattfeldt et al. 1990). The procedure was done according to Nyengaard & Gundersen (2006) and Møhlstedt et al. (2010). In the first step, each tissue block was placed on a circle divided into 100 equal divisions with one edge parallel to the 1-1 direction. A random number between 1 and 100 was generated using the Microsoft Excel RAND function and the tissue block was cut at this angle. In the second step, the freshly cut surface of the block was laid on a rounded disc with cosine-weighted angular divisions. Another random number was generated, and the block was cut parallel to this number. Thus, isotropic uniform random (IUR) histological sections were produced. The newly generated cutting plane was carefully maintained during histological processing and was used as the histological section plane. All housing hepatocytes can be visualized as individual particles and simple cutting would be sufficient for producing isotropic sections (Mandrić & Lacerda, 2003), we decided to randomize the orientation of each tissue block with respect to further use of the same embedded blocks for analyses of hepatoma cells in a future study.

Histological processing

The tissue blocks were embedded in paraffin. From each block, two consecutive histological sections randomly positioned within the

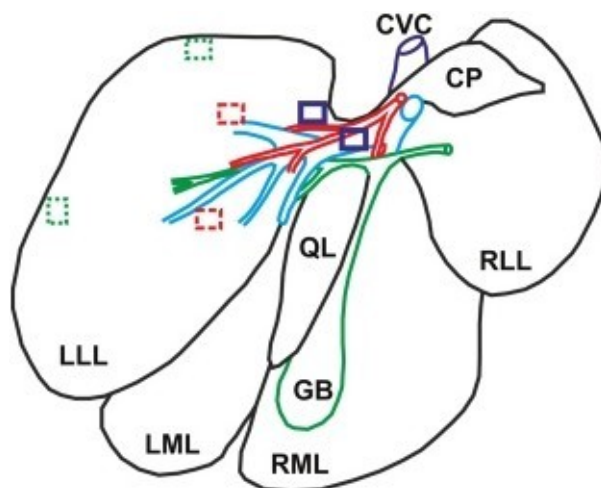


Fig. 1 Collection of tissue samples (rectangles) of the porcine liver for quantitative histology. Schematic drawing of the liver showing the outlines of the left lateral lobe (LLL), left medial lobe (LML), right medial lobe (RML), right lateral lobe (RLL), quadrate lobe (QL) and caudate lobe (nos. 11) hidden behind the vessels, the caudate process (CP), and the gallbladder (GB) and the caudal vena cava (CVC) are also shown. Branding of hepatic arteries is shown in red, branching of portal vein as blue and branching of bile ducts as green. The LLL is used as an example of collection of histological probes from three regions of interest: paracaval region (dashed blue rectangles drawn with a continuous line), parportal region (red rectangles with a dashed line), and peripheral region (green rectangles with a dotted line). Samples of the other lobes were collected accordingly.

blocks were prepared at a thickness of 16 µm and mounted on silanized SuperFrost-Plus slides (Menzel-Glaser, Braunschweig, Germany). Periodic acid-Schiff staining (PAS) was performed according to Romeis (1989) using a commercial PAS staining kit (Morphisto, Frankfurt/Main, Germany) to highlight the contours of the individual hepatocytes.

Micoscopic sampling and quantification

Following the production of two sections for each of the 251 tissue blocks, the analysis was based on 502 randomly orientated histological sections. In each section, four fields of view (FOV) were selected by systematic uniform random sampling (9-JRS) method. The use of a Leica DM2000 microscope (Leica, Wetzlar, Germany) equipped with a Leica DFC42SC camera and an oil immersion objective with 100x magnification (numerical aperture 1.25) resulted in a field of view (FOV) of a photographed size of 94.86 × 63.2 µm. The sampling started on the top left of the first section using two random numbers generated with the Microsoft Excel RAND function as *x*- and *y*-coordinates, which represented the distances of the first FOI from the left and upper borders in µm. The distance interval between the FOVs increased or decreased proportionally, i.e. the sampling step ranged between 1 and 3 mm. The histological sampling strategy is illustrated in Fig. 2A,B.

The next step required focusing of optical sections. The Z-direction feed rate of the fine focus of the Leica DM2000 microscope was verified using a Zeiss Image R2 microscope equipped with an AxioCam MRC camera (Zeiss, Vienna, Austria) and the ZEN PRO2012

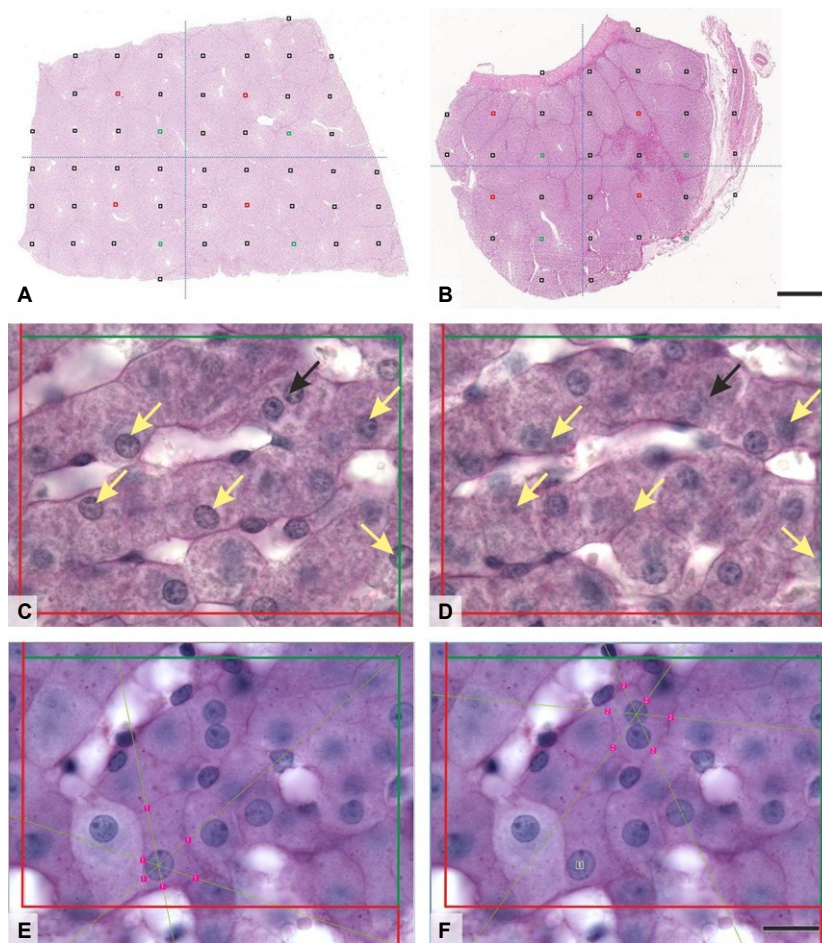


Fig. 2 Sampling of fields of view (FOV) in micrographs of liver tissue, the disector and the nucleator method. (A,B) Systematic uniform random sampling of FOVs based on a randomly positioned first FOV and equidistant placement of further FOVs, four of which were photographed for the first section (red squares) of each tissue block and four further photographed for the adjacent section (green squares). Each quadrant of the section profile was represented by one FOV. Micrographs (A) and (B) represent different shapes of tissue profiles and the necessary adaptation of distances between the FOVs. (C,D) To estimate the numerical density of hepatocytes and the fraction of binuclear hepatocytes, two optical sections from the same FOV illustrate the disector principle as follows: Whole cell profiles that were inside the counting frame or that touched the green allowance borders but not the red forbidden borders were counted, provided that their nuclear profiles were in focus with clearly visible chromatin in the bottom reference plane (C) or two subsequent planes of the disector volume probe and absent or clearly out of focus on the fourth plane (D, the look-up plane of the disector). The nuclei of the counted mononuclear hepatocytes are marked with yellow arrows, whereas the nuclei of counted binuclear hepatocytes are marked with black arrows. (E,F) To estimate the number-weighted mean volume, the cell borders of the hepatocytes previously selected with the disector method were marked with six intersecting isotropically oriented rays of the nucleator probes. This analysis was performed separately for mononuclear (E) and binuclear hepatocytes (F). Periodic acid-Schiff staining: note that cell borders are easy to identify notwithstanding the natural staining variability as shown in (C–D) vs. (E–F). The counting frame size in (C–D) was tested in a pilot study; however, the definitive size shown in (E–F) ($95 \times 63 \mu\text{m}$) was used consistently throughout the main study. Scale bars: 1 mm (A,B) and 10 μm (C–F).

program, allowing precise computed Z-stack measurement. With the 1009 immersion objective of the Leica microscope, the distance between two scale lines indicating 1 μm in the fine focus of Leica DM2000 corresponded to the verified slice thickness of 0.97 μm .

Within each FOV, a series of four optical sections was captured at a resolution of 2592 \times 1944 pixels. The Z-step between the adjacent optical sections was set to 3 μm , which was sufficiently small to not lose the readability of the sequence of the optical sections. This made it possible to follow the continuity between the corresponding cell and nuclear profiles on adjacent optical sections. Starting from the bottom, the first sharp plane of the physical section was focused using the nuclear chromatin and outline of the nucleus and

cell borders as reference points. In total, 8032 optical sections that documented 2008 FOVs were recorded. Using ELLIPSE software (ViDiTo, Kosice, Slovak Republic), the four stereological parameters described in Table 1 were quantified in the optical sections.

Numerical density of hepatocytes

Within each stack of micrographs that documented one FOV, the hepatocytes were counted using the optical disector method as shown in Fig. 2C,D. The nucleus with one or more nucleoli clearly in focus was selected as the decisive counting event (Gardella et al. 2003; Marcos et al. 2016). For the proper identification of the borders of individual hepatocytes and the chromatin of the hepatocyte

Table 1 Stereological parameters assessed for porcine hepatocytes: In the framed study.

Name and unit	Abbreviation and unit	Definition	Stereological technique used for quantification
Number of mononuclear hepatocytes	V_M (MnHEP) (μm^3)	Average volume of hepatocytes that contained one nucleus	Optical disector (Gundersen et al. 1988; Maras et al. 2012)
Number of binuclear hepatocytes	V_B (BnHEP) (μm^3)	Average volume of hepatocytes that contained two nuclei	Optical disector
Fraction of binuclear hepatocytes	f (BnHEP) (- parts of 1)	Relative amount of hepatocytes that contained more than one nucleus among all hepatocytes within the same reference volume	Optical disector
Numerical density of hepatocytes	N_V (HEP) (mm^{-3})	Average number of hepatocytes per volume unit of liver tissue	Optical disector and nucleator (Gundersen 1988; Marcos et al. 2012)

nudei, as well as for reliable measurements in the Z-direction an oil immersion objective with 100 \times magnification and a high numerical aperture (1.25) was used. The optical disector counting rules (Gundersen 1988) were used. The counting in whole cell profiles located inside the counting frame or touching the allowed borders, but not touching the forbidden borders. The cell and nuclear profiles were traced starting from the first (reference) optical plane towards the last (look-up) optical plane. Cells with nuclei visible at any of the planes 1-3 and 10 before reaching the level of the look-up plane were counted. The numerical density of the hepatocytes $N_V(\text{HEP})$ was calculated as follows:

$$Q_V(\text{HEP}) = \frac{P_1(\text{ref})}{a} \cdot \frac{p}{n}$$

where $Q_V(\text{HEP})$ represents the number of hepatocytes

with a clearly visible nucleus counted within the disector, $P_1(\text{ref})$ represents the number of points of the auxiliary grid that hit the i -th reference space, p represents the total number of points of the auxiliary grid, a represents the area of the counting frame, h denotes the height of the disector and n denotes the total number of additions within the mathematical summation of all disectors and reference space points. At least 100 cells were counted in eight disectors applied to the two tissue sections of each sample. The reference space comprised all components of the liver tissue; however, the peripheral areas composed of connective tissue were avoided.

Fraction of binuclear hepatocytes

In each sample, the relative amount of hepatocytes that contained two visible nuclei (BnHEP) was expressed as a ratio of these cells to the total number of all hepatocytes contained within the same reference volume. This assessment involved predominately binuclear hepatocytes. Trinuclear hepatocytes were observed very rarely and none of these was counted according to the disector rules.

Number-weighted mean volume of hepatocytes

The nucleator method was used as a local stereological procedure to

estimate the volume of hepatocytes. This method is based on the use of a unique arbitrary point in every object under study, i.e. in every liver cell provided the sections are isotropic uniform or vertical uniform (Gundersen 1988; Gundersen et al. 1988; Maras et al. 2012). Briefly, in every stack of optical sections investigated, hepatocyte profiles were selected using the previously described disector method. The volume of the selected hepatocyte was estimated in the central region, where the nucleus with nucleoli was visible. Using the Nucleator module of E1.1.PSt software, nucleated cell profiles sampled by the disector in the previous step were measured by marking the intersection of six isotropically oriented rays with the cell borders (Fig. 2E,F). The number of rays was based on a pilot study showing that using five, six or seven nucleator rays do not reduce the variability of measurements when compared with four nucleator rays. An average value independently calculated for the

MnHEP and BnHEP resulted in number-weighted mean volumes V_M of these cells (Table 1). In total 129 054 hepatocytes were counted and evaluated in this study.

Corrections for shrinkage and z-axis compression

estimate the volume of hepatocytes. This method is based on the use of a unique arbitrary point in every object under study, i.e. in

Formalin fixation, dehydration and paraffin embedding are steps that lead to volume shrinkage (Oorph-Petersen et al 2001; Gardella et al. 2003). Marcos et al. (2004) reported 38% shrinkage from fresh

rat liver to mounted sections. As a result of shrinkage, cell volumes appear smaller and numerical cell densities appear larger compared with fresh organs prior to processing. According to Maras et al (2012), two main sources of shrinkage are expected to contribute bias to our study: (i) the volume shrinkage caused by the formalin fixation and paraffin embedding; and (ii) a decrease in the ion thickness (compression) in the z-axis in the thick sections. It is the stretching of sections in the warm tissue flotation water bath. To compensate for the shrinkage, two corrections were applied to the results.

¶ The volume shrinkage caused by the formalin fixation and paraffin processing was estimated as follows: 11 blocks were sectioned from the fresh liver, avoiding the hepatic capsule. Each block had a shape of a precisely shaped cuboid bounded with six quadrilateral faces. The x, y, z dimensions of each tissue block were precisely measured using a caliper with a reading error of 0.5 mm and the volume of each block was calculated. In all samples, the x, y, z directions were preserved consistently to allow for evaluation of the isotropy of the shrinkage as follows: the x-direction was tangential to the liver surface from the periphery of liver lobe towards the hilum of the lobe; the y-direction was tangential to the surface and perpendicular to the x-direction; the z-direction was perpendicular to the liver surface, thus running from the

liver surface into the deeper parts of the lobe. Following routine fixation, dehydration and embedding, the tissue blocks were exhaustively cut into series of consecutive 5- μ m-thick histological sections, and every 10th section was stained with hematoxylin and eosin. The x , y , z dimensions of each processed block were measured using the histological sections and the distance between the first and the last section and the volume of the block was calculated. The mean volume ratio after/before processing (\pm SD) was 0.675 ± 0.058 . The cell volumes and disector volumes were corrected by multiplying the values measured in the paraffin sections by a correction factor of $1/0.675$. Moreover, the mean ratio \pm SD of dimensions after/before processing was calculated as follows: $X/Y = 0.897 \pm 0.071$, $Y/Z = 0.938 \pm 0.043$, and $Z/X = 0.803 \pm 0.033$. When comparing the linear shrinkages in the x -, y -, and the z -directions, the Friedman ANOVA revealed differences ($P = 0.002$), suggesting an anisotropic shrinkage. The *post-hoc* Wilcoxon matched pairs tests showed that the shrinkage in the z -direction (perpendicular to the liver surface) was more prominent than the shrinkage in the x -direction ($P = 0.003$) or the y -direction ($P = 0.003$). No difference was found when comparing the shrinkage in the x - and the y -directions parallel to the liver surface.

- ① The actual thickness of our final sections after stretching in the water bath and staining was measured using the z -stack tool of the AYO IMAGat Z2 light microscope (Zeiss, Vienna, Austria) by manually focusing the first and last sharp optical planes of the sections. The mean distance between these planes was $13 \mu\text{m}$. The microtome produced $16\text{-}\mu\text{m}$ -thick sections; thus, it demonstrated a compression factor $13/16 = 0.8125$. The cell volumes and disector volumes were increased by multiplying the values measured in the thick paraffin sections by a correction factor of $1/0.8125$.

Statistics

The software STATISTICAL PACKAGE (StatSoft, Inc, Tulsa, OK, USA) was used for the statistical analysis. Part of the data did not pass the Shapiro-Wilk's W -test for normality; thus, nonparametric methods were used for further analysis. The Kruskal-Wallis ANOVA and the Mann-Whitney U -test were used to assess the differences between the six lobes. The differences between the ROIs defined within the lobes, and the differences among the individual animals investigated. The relationships between the four stereological parameters were evaluated using the Spearman rank order coefficient. The coefficients of error (CE) estimating the sampling error were calculated according to Gundersen et al (1999) separately on the level of tissue blocks and on the level of individual animals.

Results

The mean number-weighted volume of mononuclear hepatocytes after shrinkage correction in all samples investigated was $3670 \pm 805 \mu\text{m}^3$ (mean \pm SD). The mean number-weighted volume of BnHEP was $7050 \pm 2550 \mu\text{m}^3$. The fraction of BnHEP was $4 \pm 2\%$. The numerical density of all

hepatocytes was $146\,997 \pm 15\,738 \text{ cells mm}^{-3}$. No patho-

logical findings, such as inflammation, necrosis, fibrosis or extensive steatosis, were identified in the animals investi-

gated. The complete stereological results for all samples are provided in Table S1.

Size, nuclearity and density of hepatocytes in the hepatic lobes of the pig

No differences between the hepatic lobes were identified when comparing the values of all four quantitative parameters investigated (Fig. 3A-D).

Size, nuclearity and density of hepatocytes in parportal, peripheral and paracaval ROIs

The greatest number-weighted mean volume of mononuclear hepatocyte, $V_N(\text{MnHEP})$ was identified in the peripheral regions of the liver lobes ($P < 0.05$); however, there was no difference between the parportal and paracaval regions (Fig. 4A). The number-weighted mean volume of binuclear hepatocyte, $V_N(\text{BnHEP})$ (Fig. 4B) and the fraction of binuclear hepatocyte, $f(\text{BnHEP})$ (Fig. 4C) were not different among the ROIs. The numerical density of the hepatocytes $N_V(\text{HEP})$ was smaller in the peripheral region than in the paracaval region ($P < 0.01$) or the parportal region ($P < 0.001$, Fig. 4D).

Size, nuclearity and density of hepatocytes compared among the individual animals

In all four parameters investigated (Fig. 5A-D), significant interindividual differences were identified.

Correlation between the size, nuclearity and density of hepatocytes

The number-weighted mean volume of mononuclear hepatocytes $V_N(\text{MnHEP})$ was moderately correlated (Spearman $R = 0.55$) with the number-weighted mean volume of binuclear hepatocyte, $V_N(\text{BnHEP})$ identified in the same samples. The numerical density of hepatocytes $N_V(\text{HEP})$ exhibited a moderate negative correlation with the number-weighted mean volume of mononuclear hepatocyte, $V_N(\text{MnHEP})$ ($R = -0.52$) as well as with the number-weighted mean volume of binuclear hepatocytes $V_N(\text{BnHEP})$ ($R = -0.33$).

Discussion

The mean number-weighted volume of MnHEP (Table 2) partially corresponds with the number-weighted mean cell volume of MnHEP published in other mammalian species. Using model-based stereology, Rohr et al. (1976) reported

the volume of human hepatocyte, as $11\,305 \mu\text{m}^3$. For a gated. The CE ranged between 0.084 and 0.125 on the level

direct comparison with studies that used similar design based stereological methods applied in histological sections, Jack et al. (1990) reported the number-weighted mean cell

Analysis of size and density of porcine hepatocytes, K. L. J. et al. 579

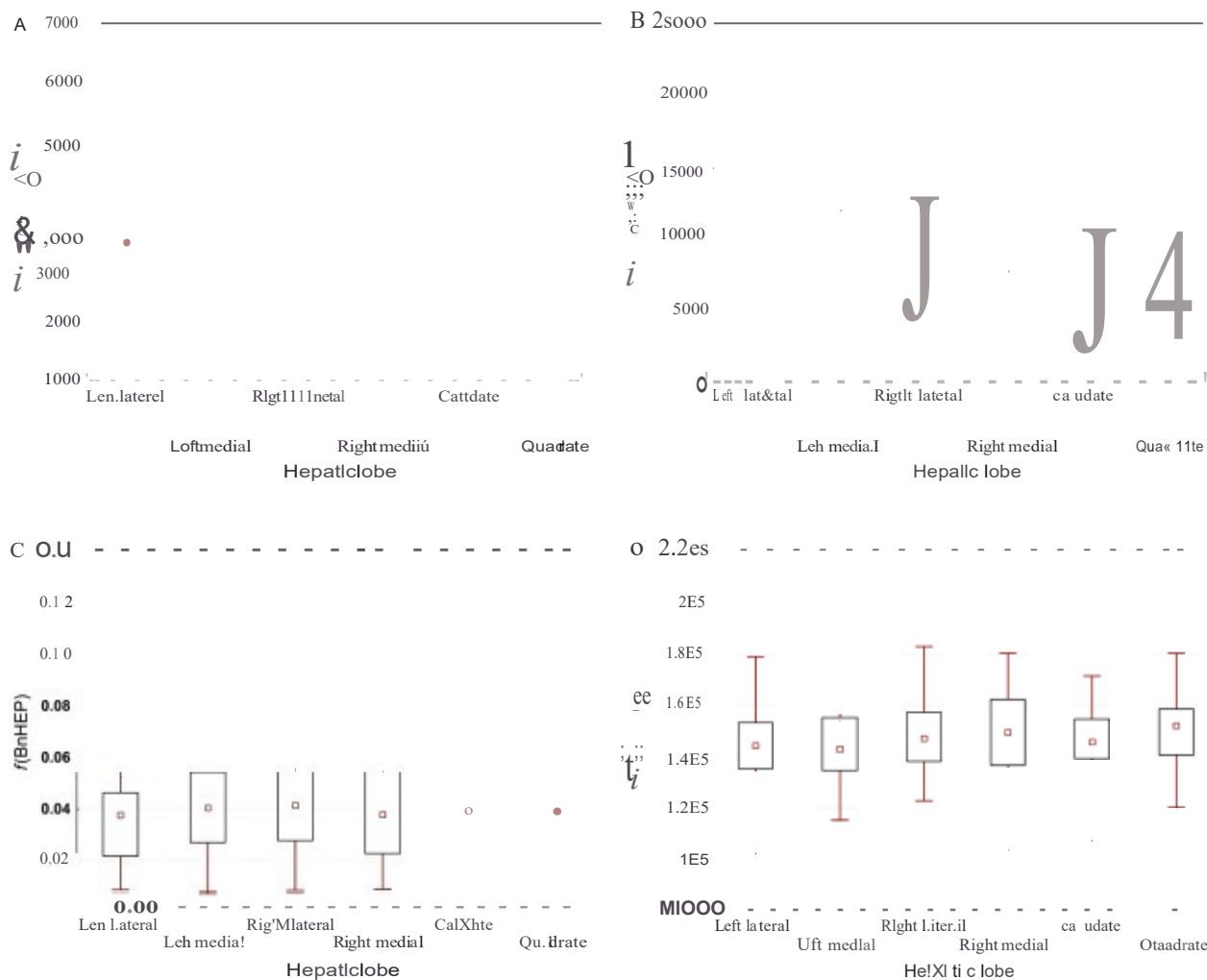


Fig. 3 Estimates of size, number and density of hepatocytes in six porcine hepatic lobes. (A) Number-weighted mean volume of mononuclear hepatocytes: VN(MnHEP) (B) Number-weighted mean volume of binuclear hepatocytes: VN(BnHEP) (C) Fraction of binuclear hepatocytes among all hepatocytes: f(BnHEP) (D) Numerical density of hepatocytes: N(HEP). Kruskal-Wallis test indicated that there were no differences among the lobes in the parameters. Data are displayed as median values with boxes that span the limits of the first and third quartiles and whiskers that span the minimum and maximum values for each lobe.

volume as $4740 \mu\text{m}^3$ in MnHEP and $6930 \mu\text{m}^3$ in BnHEP in female rats. Karbalay-Ooust & Noorafshan (2009) determined the volume, number-weighted mean volume of mice to be $5300 \mu\text{m}^3$. Marcos et al. (2016) determined the number-weighted mean volume of MnHEP to be $6044 \mu\text{m}^3$ in male rats and $4789 \mu\text{m}^3$ in female rats, whereas the number-weighted mean volume of BnHEP was $7530 \mu\text{m}^3$ in male vs. $6565 \mu\text{m}^3$ in female rats. Hammad et al. (2014) determined the mean volume of hepatocytes in mice to be $5128 \mu\text{m}^3$. Moreover, the porcine BnHEP in our study had volumes comparable with BnHEP in the rat liver (Jack et al. 1990; Marcos et al. 2016). We found that BnHEP had almost twice the volume of MnHEP. According to Watanabe & Tanaka (1982) and Peinado et al. (1990), the size of hepatocytes corresponds to the sum of ploidy of all the nuclei and

is also linked to the volume of stored lipid droplets. To date, there is no information published regarding the volume of BnHEP within a tissue context (i.e. not in single cell suspension) in species other than rats and pigs.

Porcine hepatic lobes contain hepatocytes of comparable size, nuclearity and density

Our results (Fig. 3) demonstrated that the six hepatic lobes of the porcine liver have a similar distribution of hepatocytes of various sizes, numbers of nuclei and densities. This finding suggests that individual lobes may be chosen as

technically appropriate for experiments on liver regeneration such as partial lobectomy or hepatectomy (Bruha et al. 2015) even if quantitative histology is applied. The morphology of hepatocytes would remain unbiased by the finding that some tissue probes would originate from various hepatic lobes, provided the sampling of tissue probes is not substantially lower than in the present study.

Peripheral regions of hepatic lobes contain the largest MnHEP with the smallest numerical density

The finding of intralobar differences in the hepatocyte size and density (Fig. 4) clearly demonstrates the

Analysis of size and density of porcine hepatocytes, K. L. Ju, et al. 581

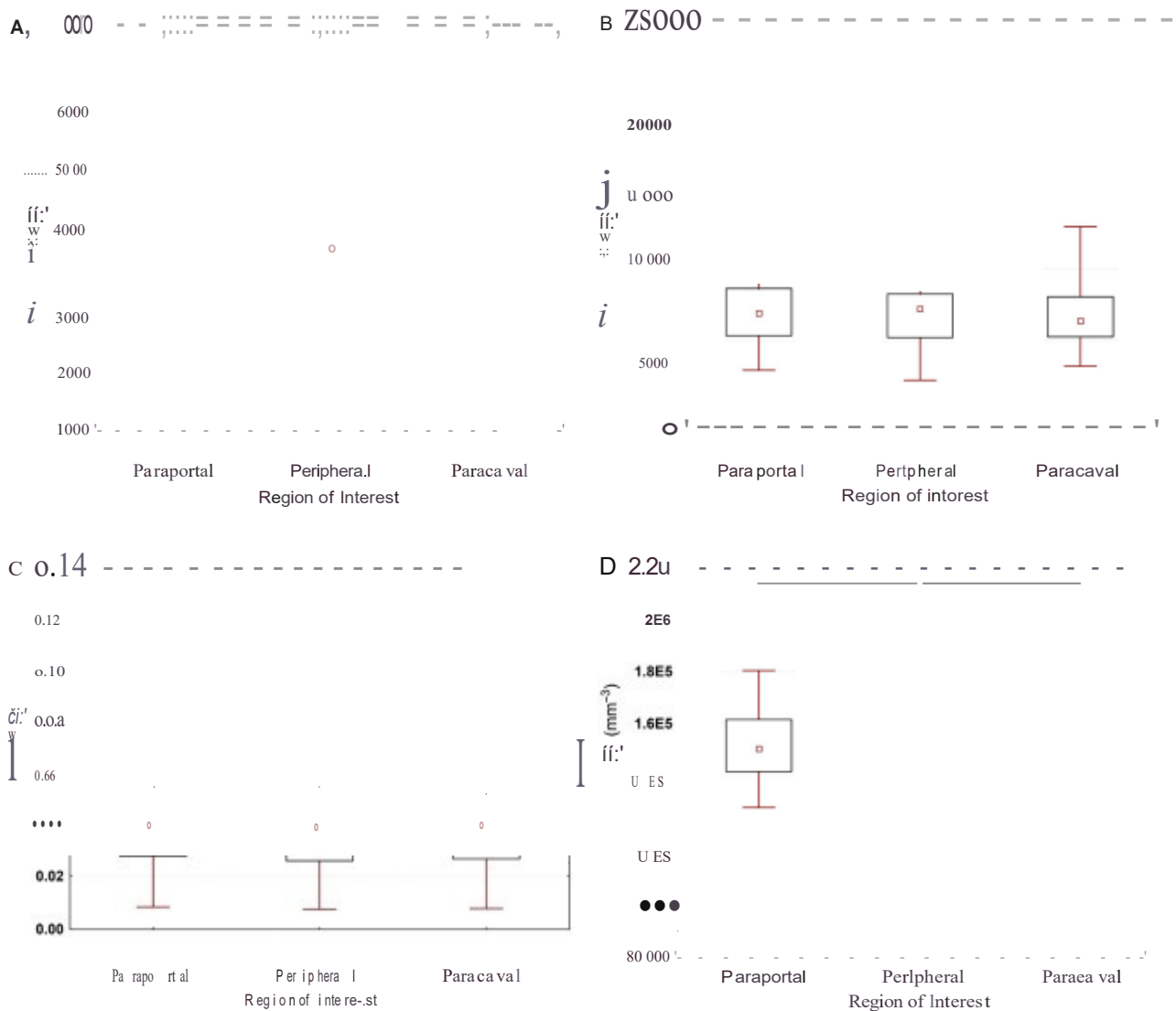


Fig. 4 Estimates of size, number and density of hepatocytes in three macroscopically defined regions with respect to their proximity to the 111.1 portal vein in the pig (A) The largest number-weighted mean volume of mononuclear hepatocytes (MNH) was identified in the periportal region. (B) The number-weighted mean volume of binuclear hepatocytes (BNH) exhibited no differences between the regions (C) The fraction of binuclear hepatocytes among all hepatocytes (BNH/total) exhibited no differences between the regions (D) The smallest numerical density of hepatocytes (NHEP) was identified in the peripheral region. Statistical significance ($P < 0.05$, $P < 0.01$, $P < 0.001$) identified using the Mann-Whitney U-test are presented. Data are displayed as the mean \pm SEM with boxes representing the first and third quartiles and whiskers that span the minimum and maximum values for each group.

importance of systematic sampling when obtaining histological probes from hepatic lobes that exhibit a prominent anatomical hierarchy of blood vessels. However, the biological interpretation of these results is not straightforward. The mammalian cell size is regulated in correlation with the cell cycle progression (e.g. Shen et al. 2000); however, it has been demonstrated that cell growth and cell cycling are separable and thus distinct processes (Fingar et al. 2002). The coordination of cell growth with cell replication has also been suggested for liver regeneration (Fausto & Campbell, 2003). However, it is not known how the hepatocyte volume changes during the cell cycle and

whether the proliferation rate and duration or dynamics of the cell cycle differ with distance from the large branches of the portal vein and hepatic proper artery.

Proteins such as membrane transporters, volume-sensitivity ion channels, and stretch-activated channels, as well as

molecules that function as cellular osmolytes play a crucial role in cell size regulation (Hoffmann & Dunham, 1995). It is not known whether the expression of these proteins differs within the liver lobe, which would provide an explanation for the cell size variability. A specific lobular zonation as described for some hepatic enzymes (Spear et al. 2006) may be expected with differences between periportal vs. pericentral regions.

Polyploidization of hepatocytes increases with age (as seen in rats after stress) and leads to an increased cell volume (Pandit et al. 2013). It may be hypothesized that the peripheral parts of the liver lobes represent the developmentally oldest hepatic regions and thus contain more large polyploid cells. Tanami et al. (2016) mapped the zonation of liver polyploidy in rat, revealing that liver polyploidy proceeds in spatial waves, advancing more rapidly in the mid-lobule zone than the periportal and peripheral zones. The

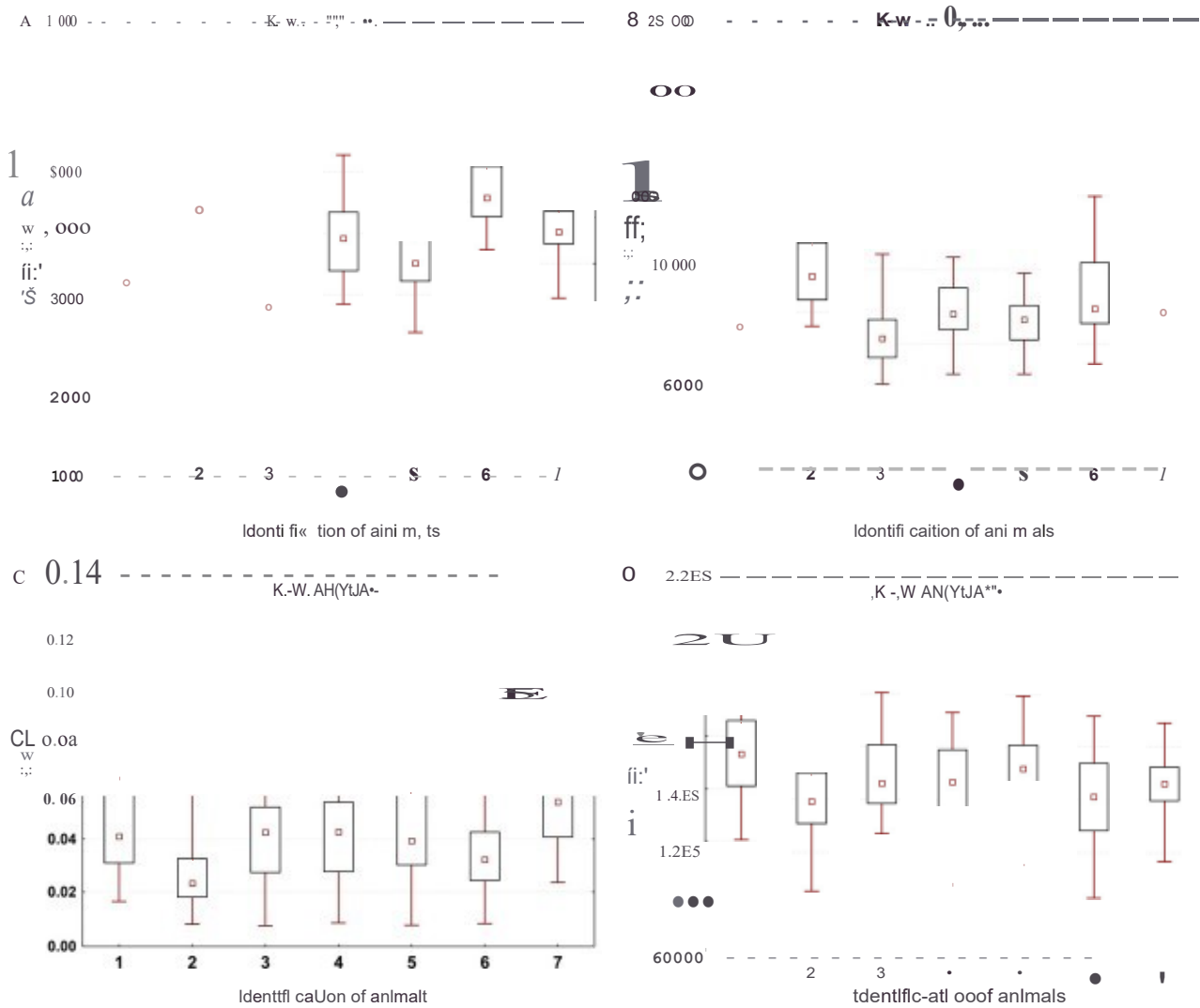


Fig. 5 Estimates of size, nuclearity and density of hepatocytes in seven piglets investigated. All paraffin-embedded investigated exhibited differences among the animals as illustrated in (A) for the number-weighted mean volume of mononuclear hepatocytes (MnHEP), (B) for the number-weighted mean volume of binuclear hepatocytes (BnHEP), (C) for the fractal dimension of binuclear hepatocytes among all hepatocytes (BriHEP) and (D) for the numerical density of hepatocytes (Nv(HEP)). Significant differences ($p < 0.001$) identified using the Kruskal-Wallis test are presented. Data are displayed as median values with boxes that span the middle of the first and third quartiles and whiskers that span the minimum and maximum values for each animal.

Table 2 Estimated number-weighted mean volume of mononuclear hepatocytes (MnHEP) and binuclear hepatocytes (BnHEP), fractal dimension of binuclear hepatocytes among all hepatocytes (BriHEP), and numerical density of hepatocytes (Nv(HEP)) in three macroscopic regions of the porcine liver with respect to their proximity to the liver sinusoidal space. Data are presented as medians and quartile ranges (the value of the 75th percentile minus the value of the 25th percentile, including 50% of the cases).

		Paraportal regions	Peripheral regions	Paracaval regions
ii. (MnHEP) (μm^3)	Median	3536	3880	3593
	Quartile range	841	1277	866
ii. (BnHEP) (μm^3)	Median	7015	7397	6739
	Quartile range	3258	2991	2786
f(BnHEP) (%)	Median	4%	4%	4%
	Quartile range	3%	3%	3%
Nv(HEP) (mm^{-3})	Median	150 776	141 413	148 845
	Quartile range	20 328	20 963	19 693

findings of Gerlyng et al. (1993) suggest that polyploid hepatocytes in rat liver have a greater tendency to replicate; however, they predominantly divide into mononuclear

daughter cells. Diploid and polyploid hepatocyte, originate predominantly through failed cytokinesis (Duncan. 2013; Gentric & Desdouets. 2014) and it was suggested that they

promote liver homeostasis and regenerative turnover (Gentric et al. 2012; Pandit et al. 2013; Wang et al. 2015). Moreover, aneuploid hepatocytes seem to be differentially resistant to chronic liver injury, and regenerate the liver (Duncan, 2013.)

In respect of the cause of intralobar differences in the hepatocyte size and density, it should be noted that the morphometry of hepatocytes *may be* easily biased when samples for quantitative histology are collected from regions with different positions between large vessels and the periphery of liver lobes.

Size, density and fraction of BnHEP exhibit considerable individual differences

As shown in Fig. 5, healthy pigs of the same age and breed with a similar total liver volume of 813 ± 85 ml

(mean \pm SD, see Table S1), and identical diet and handling may have significant interindividual differences at the level of hepatocytes evaluated within their tissue context. How-

ever, Stegemann et al. (2000) demonstrated with sufficient

precision and accuracy that the average size of isolated porcine hepatocytes remained consistent among individuals. The number of animals in our study does not enable a reliable comparison between males and females; hence, we never speculate that sexual dimorphism *may* explain, at least in part, this variability. Nevertheless, the piglets investigated were prepubescent, and the influence of sex hormones could be expected to remain small. Detailed studies on the rat liver (Marcos et al. 2015b, 2016) showed that the female liver contained an increased number of hepatocytes per gram and contained more binucleate cells, thus suggesting an increased regenerative potential in female compared with male rat liver. Moreover, it should be noted that the number of nuclei visible in the optical microscope using routine histological sections is completely different from the cell ploidy of hepatocyte, assessed using advanced methods, such as single molecule fluorescence *in situ* hybridization. Hepatocytes with one or two nuclei *may* contain two, four, eight or even more haploid chromosome sets (Tanami et al. 2016). In contrast to our findings (4% of 8nHEP), Vinogradov et al. (2001) reported in a pig of unknown age that 54% of binuclear hepatocyte had $2 \times 2c$ ploidy. The most probable explanation of this discrepancy is the gradual increase in liver ploidy during aging, which has been reported by Guidotti et al. (2003) and Gentric & Desdouets (2014).

Distribution of larger MnHEP correlates with a larger volume of BnHEP and a smaller numerical density of all hepatocytes

rather than entirely independent. Our study demonstrated that in regions with large MnHEP, the size of BnHEP was also large. Simultaneously, the regions that contained hepatocytes with a large volume had a tendency to contain a smaller ratio of BnHEP. It remains to be determined whether an increased degree of polyploidy, which has been indicated to lead to larger cell sizes and increased occurrence of bi- and multinuclear cells (Pandit et al. 2013), *may* provide an explanation for these correlations.

Regions with a greater volume of hepatocyte, exhibited a smaller density of hepatocyte, per unit of volume. One explanation for this correlation is that if cells grow large, fewer cells fit in the reference space. However, the volume fractions of the hepatic vascular bed and the intralobular connective tissue would have to be taken into account for a correct interpretation of this finding. Mapping of the vol-

ume fractions of the main porcine liver components

remains to be performed. As shown in recent studies (Debaud et al. 2012, 2014b), this *may* be done economically by combining the histological approach with a three-

dimensional analysis and stereological quantification of hepatic

When interpreting the biological meaning of the numerical results of hepatocyte morphometry, it should be noted that the morphological parameters are statistically correlated,

microvessels using high resolution X-ray microtomography of vascular corrosion casts (Eberlova et al. 2016; Jiřík et al. 2016). Moreover, quantitative data regarding the size and density of hepatocyte, may also be combined with multi-level modeling of hepatic perfusion (Debbaut et al. 2014a; Peeters et al. 2015).

Study implications

When evaluating the histomorphometry of hepatocyte, in experiments with porcine livers, a high variability should be expected in interindividual differences. Another major source of variability as demonstrated in our study was the position of the tissue probes with respect to the distance from the major hepatic blood vessels. Moreover, the samples collected from various hepatic lobes exhibited too differences in healthy piglets; hCYt. Never, interobar differences have been reported in various cases of liver alterations (e.g. Richardson et al. 1986; Faa et al. 1995; Regev et al. 2002; Irwin et al. 2005; Palladini et al. 2012). Our findings fully comply with the well-known recommendations of Gundersen & Østerby (1981), who demonstrated that in atypical biological experiment the interindividual biological variability is responsible for up to 70% of the overall observed variance.

As practical suggestions for further studies that involve stereological evaluation of the size, nuclearity and density of hepatocytes in porcine liver, we would recommend the following: the use of sufficient numbers of pigs per study group; a power analysis for estimating the minimum number of animals per study group may be easily calculated from our results. For example, when planning an experiment and expecting the mean numerical density to be decreased by 20% i.e. from 97 500 to 78 000 cells μm^{-3} , the minimum number of animals per group would be

eight, using the typical test power $1 - P^* = 0.8$ (where P is the type I error) and $\alpha = 0.05$ (where α is the type II error) (Chow et al. 2008), systematically obtaining histological probes from both the peripheral parts of the hepatic lobes and the vicinity of the major intrahepatic blood vessels; using the six hepatic lobes of porcine liver independently in experiments that address partial lobectomy or hepatectomy because tissue probes sampled from various lobes yield comparable results provided that the parportal and peripheral regions are sampled accordingly; when analyzing 36 probes per animal, the CE was reasonably low (0.014–0.018); reducing the number of probes to 18 would result in an increased CE of approximately 0.15, which can be derived from the Table S1. Therefore we recommend obtaining at least 20 histological probes per individual. Future studies in the pig would provide important additional information with respect to other quantitative parameters, such as the distribution of intralobular and interlobular connective tissue (Marcos et al. 2015a), as well as the lobular zonality of liver pathologies (e.g. Schwen et al. 2016) and gene expression in hepatocyte, (Schwen et al. 2015).

This study has several limitations. Although none of the samples showed histopathological alterations, no liver biochemical tests were done and the liver function was not assessed in this study. Our study was based on one type of simple PAS staining outlining the glycocalyx of the cell membrane. This approach may also represent an advantage when processing archive samples. However, hepatocyte, laden with PAS-positive glycogen granule, partially lose contrast between the cytoplasm and cell membrane. For some applications, complex staining protocols enable the interpretation of the morphometry of hepatocytes within the context of the liver tissue (Hoehme et al. 2010; Schwier et al. 2013; Hammad et al.

2014.) Moreover, whole-slide imaging (Hoehme et al.

2010; Schwier et al. 2013; Hammad et al. 2014) is a good choice to handle the variability in the level of more histological sections.

Our study generated a number of more detailed questions that, to our knowledge, have not been addressed to date for the porcine liver.

Conclusion The size, nuclearity and density of hepatocyte, will have to be mapped with respect to the position of the hepatocytes within the classical morphological hepatic lobules (Marcos et al. 2016), as well as within the zones of the liver acini. The identification of the lobular and acinar distributions of the stereological characteristics of hepatocytes would contribute to understanding their role in pathological processes that preferentially involve zones of a liver lobule, such as demonstrated during centrilobular necrosis as a result of passive congestion, after poor oxygenation of hepatocyte, (Saxena, 2011), in drug-induced porcine

a porcine model of small-for-size syndrome (Kelly et al. 2009) or in a porcine hepatectomy model with a portocaval shunt (Li da et al. 2007). Similarly, portal inflammation was found to be present in a porcine model of acid aspiration (Heuer et al. 2012) and in toxin-induced fulminant hepatic failure (Collins et al. 1994).

Discussion Sexual dimorphism of the hepatocyte size and density (Marcos et al. 2016) examined together with enzyme activity (Bode et al. 2010) may elucidate the regenerative potential of male vs. female porcine livers.

1 It remains unknown how the size, nuclearity and density of hepatocyte, are associated with their proliferation rate.

2 From a stereological point of view, the total amounts of hepatocytes within the lobes of the porcine liver remain to be estimated using the fractionator sampling scheme (Marcos et al. 2012). This parameter is not biased by shrinkage and is therefore useful when comparing the functional capacity of the lobes.

Conclusion

The mean number-weighted volume of porcine mononuclear hepatocyte, was $3670 \pm 805 \mu\text{m}^3$ (mean \pm SD, corrected for shrinking during histological processing). The mean number-weighted volume of binuclear hepatocytes was $7050 \pm 2550 \mu\text{m}^3$. The fraction of binuclear hepatocyte, was $4 \pm 2\%$. The numerical density of all hepatocytes was $146997 \pm 15738 \text{ cells mm}^{-3}$. Porcine hepatic lobes contained hepatocyte, of a comparable size, nuclearity and density without significant differences between the lobes. Peripheral ROIs of hepatic lobes contained the largest

number of hepatocytes with the smallest numerical density. The hepatocyte

models of liver failure (Newsome et al. 2010), in

size and density, as well as the fraction of
BnHEP exhibited considerable interindividual
differences even in healthy young animals. The
distribution of larger M nHEP was correlated with a
larger volume of BnHEP and a smaller numerical
density of all hepatocytes. The complete primary
stereological data in the form of continuous variables have
been made available as a supplement to this paper.
Practical recommendations for designing studies that
involve stereological evaluations of the size, nu-
clearity and density of hepatocytes in porcine liver are
provided. However, a number of biologically relevant
parameters remain to be mapped within the porcine
liver.

Acknowledgements

This study was supported by the National Sustainability
Program I (NPI) No. L01503 provided by the Ministry of
Education, Youth and Sports of the Czech Republic and the
Prvok P36 Project of Charles University in Prague. T.K.
was supported by the project

D 151)6 of the Czech Ministry of Education Youth and Sports. The skillful technical support of Ms Anne Flemming, Ms Claudia Hixmann and Ms Brigitte Machac is gratefully acknowledged.

Conflict of interest

The authors declare that they have no conflict of interest.

Author contributions

Khan Lamanero-Junatas - review of the literature; histological tissue processing; microscopy and quantification of the sections; data acquisition; illustrations and manuscript writing. Zbyněk Tonar - idea and concept of the study; literature review; stereological design of the study. conducted pilot study; illustrations; statistics; drafting and writing of the manuscript. Tereza Kubíková - quantification of tissue shrinkage in formalin fixed and paraffin-embedded histological sections. Václav Liška and Richard Pálek - contribution to the study design; animal handling; harvesting the liver; performing the sampling of liver tissue probes from

anatomical lobes and regions with different vascular supply. Patrik Mik - review of the literature on binuclear hepatocytes, contribution to the revised manuscript. Milena

Kralickova - critical revision of the manuscript and approval

of the article. Kirsti Witter - contribution to the study design and the pilot feasibility study; histological tissue processing; manuscript writing and editing.

References

- Alexandris N, Galdopoulou H, Dimitriou C, et al (2008) Liver histology alterations during carbon dioxide pneumoperitoneum in a porcine model. *Surg Endosc* 2003, 415-420.
- Altokaynak BZ, Ozbek E (2009) Overweight and structural alterations of the liver in female rats fed a high-fat diet: a stereological and histological study. *Turk J Gastroenterol* 2009, 93-103.
- Arbudo N, Defterevos G, Nastos C, et al. (2011) Development of a porcine model of post-hepatectomy liver failure. *J Surg Res* 170, 33-42.
- Asoaka Y, Togaishi Y, Mutsuga M, et al. (2016) Histopathological changes of chemically induced hepatocellular hyperplasia in mice. *Exp Toxicol Pathol* 68, 233-239.
- Bahr AK, Kaser T, Kemter E, et al. (2016) Ubiquitous LEA29Y expression blocks T cell activation but permits sexual reproduction in genetically modified pigs. *PLoS ONE* 11, e0155676.
- Best JM, Manka P, Syn WK, et al. (2015) Role of liver progenitors in liver regeneration. *Hepatobiliary Surg Nutr* 4, 48-58.
- Bode G, Clausen P, Gerwis F, et al. (2010) The utility of the

isolated hepatocytes, and the intact liver: studies with induced livers involving diazepam. *Drug Metab Dispos* 28, 903-911.

OKW 5, Sihao, J Wang H (2008) *Sample Size Calculations in Clinical Research*. 2nd edn. Boca Raton: Chapman & Hall/CRC Biostatistics Series.

- Collins BH, Chari RS, Magee JC, et al. (1994) Mechanisms of injury in porcine livers perfused with blood of patients with fulminant hepatic failure. *Transplantation* 15, 1162-1171.
- Cooper OK, Ekser B, Tector AJ (2015) A brief history of digital xenotransplantation. *Int J Surg* 23, 205-210.
- Court F, Wemyss-Holden S, Morrison C, et al. (2003) Segmental nature of the porcine liver and its potential as a model for experimental partial hepatectomy. *Br J Surg* 90, 444.
- Damis B, Mohkam K, Schmitt Z, et al. (2015) Subtotal hepatectomy in swine for studying small-for-size syndrome and portal flow modulation: is it reliable? *HPB (Oxford)* 17, 881-888.
- Debbaut C, Vieren dees J, Castelleyn C, et al. (2012) Perfusion characteristics of the human hepatic microcirculation based on three-dimensional reconstructions and computational fluid dynamic analysis. *J Biomed Eng* 134, 011003.
- Debbaut C, Monballeu O, Segers P (2014a) Engineering platform of view on liver transplantation strategies: multi-level modeling of hepatic perfusion. *Transplant Proc* 46, 3143-3146.
- Debbaut C, Segers P, Comiuc P, et al. (2014b) Analyzing the human liver vascular architecture by combining vascular reconstruction and micro-CT scanning: a feasibility study. *J Anat* 224, 509-517.
- Deng M, Kleinert R, Huang H, et al. (2009) Statistical and economic efficiency in assessment of liver regeneration using defined sample size and selection in combination with a fully automated image analysis. *J Histochem Cytochem* 57, 107-1035.
- Dorp Peterse K, A Nyengaard J, Gundersen HJ (2001) Tissue shrinkage and unbiased stereological estimation of particle number and size. *J Microsc* 204, 232-246.
- Dlwan AW (2013) Aneuploidy, polyploidy and ploidy reversal in the liver. *Semin Cell Dev Biol* 24, 347-356.
- Eberl W, Uška V, Mirka H, et al. (2016) Porcine liver vascular bed in Biodur E20 cocultures. *Folia Morphol (Warsz)* 15, 154-161.
- Faa GN, Chi V, Demelia L, et al. (1995) Uneven hepatic mPper distribution in Wilson's disease. *J Hepatol* 22, 303-308.
- Fausto N, Campese U, Johnson JS (2003) The role of hepatocytes and oval cells in liver regeneration and repopulation. *Mech Dev* 120, 117-130.
- Fingar DC, Salama S, Tsou C, et al. (2002) Mammalian cell size is controlled by mTOR and its downstream targets S6K1 and 4EBP1/eIF4E. *Genes Dev* 16, 1472-1487.
- Gardella O, Hatton WJ, Rind HB, et al. (2003) Differential tissue shrinkage and mpression in the z-axis: implications for optical dissection counting in vibratome, plastic and cryosections. *J Neurosci Methods* 124, 45-59.
- minipig as an animal model in regulatory toxicology. *J Pharmacol Toxicol Methods* 62, 19-220.

- Garrido F, Zabka TS, Tao J et al. (2013) Quantitative histological assessment of xenobiotic-induced liver enzyme induction. *586 Analysis of size and density of porcine hepatocytes*, K. L. Jun et al. *against transforming growth factor Beta 1 does not influence liver regeneration after resection in large animal experiments. In Vivo*, 29, 327-340.
- Carille J, Zomorodi K, Houston JB (1997) Scaling factors to relate drug metabolic clearance in hepatic microsomes and pituitary-thyroid axis stimulation in rats using whole-slide automated image analysis. *J Histochem Cytochem* 61, 362-371.
- Gentric G, Oesdouets C (2014) Polyploidization in liver tissue. *Am J Pathol* 184, 322-331.
- Gentric G, Oesdouets C, Clément M, et al. (2012) Hepatocytes polyploidization and cell cycle control in liver physiopathology. *Int J Hepatol* 2012, 282430.

- Gerlyng P, Abyholm A, Grotnol T, et al (1993) Binucleation and ploidy polarization patterns in developmental and regenerative rat liver growth. *Cell Prolif* 26, 557-565.
- Gravante G, Ong SL, West K, et al. (2012) Patterns of histological changes following hepatic electrolytic ablation in an ex vivo perfused model. *Pathol Oncol Res* 18, 1035-1049.
- Guidotti JE, Br gerie O, Robert A, et al. (2003) Liver cell ploidy: a pivotal role for binuclear hepatocytes. *J Biol Chem* 278, 19095-19101.
- Goodersen HJ (1988) The nucleolar. *J Microsc* 151, 3-21.
- Goodersen HJ, Osterby R (1981) Optimizing sampling efficiency of stereological studies in biology: or 'do more less well!'. *J Microsc* 121, 65-73.
- Goodersen HJ, Bagger P, Bendtsen TF, et al. (1988) The new stereological tools: disector, fractionator, nucleolar and point sampled intercepts and their use in pathological research and diagnosis. *APMIS* 96, 857-881.
- Goodersen HJ, Jensen EB, Kieu K, et al. (1999) The efficiency of systematic sampling in stereology. *J Microsc* 193, 199-211.
- Haga S, Ogawa W, Inoue H, et al (2005) Compensatory recovery of liver mass by Akt-mediated hepatocellular hypertrophy in liver-specific STAT3-deficient mice. *J Hepatol* 43, 799-807.
- Hammad S, Hoehme S, Friebe A, et al. (2014) Protocol for staining of bile canaliculi and sinusoidal network of human mouse and pig livers, three-dimensional reconstruction and quantification of tissue microarchitecture by image processing and analysis. *Arch Toxicol* 87, 1161-1183.
- Han J-P, O-Oron RL, Dodson GM, et al. (2015) Comparison of arterial shunting with perihepatic padding versus portal hepatic packing alone for retrohepatic vena caval injuries in a swine model. *Injury* 46, 1751-1764.
- Hessheimer AJ, Escobedo B, Munoz J, et al. (2014) Somatostatin therapy protects porcine livers in small-for-size liver transplantation. *Am J Transplant* 14, 1816-1816.
- Heuer JF, Sauter P, Pelosi P, et al. (2012) Effects of pulmonary aspiration on the lungs and extra-pulmonary organs: a randomized study in pigs. *Crit Care* 16, R35.
- Hoehme S, Brulport M, Bauer A, et al. (2010) Prediction and validation of cell alignment along microvessels as order principle to restore tissue architecture in liver regeneration. *Proc Natl Acad Sci U S A* 107, 10371-10376.
- Hoffman EK, Ooham PB (1995) Membrane mechanisms and intracellular signalling in cell volume regulation. *Int Rev Cytol* 161, 173-262.
- Howard CV, Reed MG (2005) *Unbiased Stereology. Three-Dimensional Measurement in Microscopy*, 2nd edn. New York: Springer.
- Hussein KH, Pari KM, Kim HM, et al. (2015) Construction of a bio-compatible decellularized porcine hepatic lobe for liver bioengineering. *Int J Artif Organs* 38, 9-114.
- Lid T, Yagi S, Tsubota I, et al. (2007) Improvement of morphological changes after 70% hepatectomy with portocaval shunt: preclinical study in porcine model. *J Surg Res* 143, 238-246.
- Irwin R, Parker, J, Lobenhofer E, et al. (2005) Transcriptional profiling of the left and median liver lobes of male F344/N rats following exposure to acetaminophen. *Toxicol Pathol* 33, 111-117.
- Jirak M, Tonar Z, Kr lkov A, et al. (2016) Stereological quantification of microvessels using semiautomated evaluation of x-ray microtomography of hepatic vasculature. *Int J Comput Asskt Radio/ Surg* 11, 1803-1819.
- Karbalay-Doust S, Nooraktian A (2009) Stereological study of the effects of nandrolone decanoate on the mouse liver. *Micron* 40, 471-475.
- Keily DM, Zhu X, Sihiba H, et al. (2000) Fisetin restores the hepatic artery buffer response and improves survival in a porcine model of small-for-size syndrome. *Liver Transpl* 15, 1448-1457.
- Kwon YJ, Lee KG, et al. (2015) (Clinical implications of advances in liver regeneration. *Clin Mol Hepatol* 21, 7-13.
- Kuvshinov, Treska V, Mirka H, et al. (2012) Immediate preoperative use of biological therapy does not influence liver regeneration after large resection - porcine experimental model with monodirectional body against epidermal growth factor. *In Vitro*, 26, 683-691.
- Mandarin Mfe-Lacerda CA (2003) Stereological tools in biomedical research. *An Acad Bras Cienc* 15, 469-486.
- Marcos Ft Monteiro RA, Rocha E (2004) Estimation of the number of stellate cells in a liver with the smooth fractionator. *J Microsc* 215, 174-182.
- Marcos Ft Monteiro RA, Rocha E (2007) Oestimation of hepatocellular number in the rat. *Toxicol In Vitro* 21, 1692-1693.
- Marcos Ft Monteiro RA, Rocha E (2012) The use of design-based stereology to evaluate volumes and numbers in the liver: a review with practical guidelines. *J Anat* 220, 303-317.
- Marcos Ft Braga B, Fontes Sousa AP (2015a) Image analysis or stereology: which to choose for quantifying fibrosis? *J Histotechnol* 63, 734-736.
- Marcos Ft Correia Gomes, C Miranda K et al. (2015b) Liver gender dimorphism - insights from quantitative morphology. *Histol Histopathol* 30, 1431-1437.
- Marcos R, Lopes C, Malhao F, et al. (2016) Stereological assessment of sexual dimorphism in the rat liver reveals differences in hepatocytes and Kupffer cells but not hepatic stellate cells. *J Anat* 228, 99-1005.
- Mattfeldt T, Mali G, Gharehbaghi H, et al. (1990) Estimation of surface area and length with the orientator. *J Microsc* 159, 301-317.
- Myaoka Y, Bato K, Kalo H, et al. (2012) Hypertrophy and unconventional cell division of hepatocytes under liver regeneration. *Cu Biol* 22, 1117-1175.
- Mouton PR (2002) *Principles and Practices of Unbiased Stereology. An Introduction for Bioscientists*. Baltimore: Johns Hopkins University Press.
- Muhlfeld C, Nyengaard JR, Mayhew EP, et al. (2010) A review of state-of-the-art stereology for better quantitative morphology in cardiac research. *Cardiovasc Pathol* 19, 68-82.
- Newsome PN, Henderson NC, Neilson U, et al. (2010) Development of an in vivo monitored porcine model of acetaminophen-induced acute liver failure. *BMC Gastroenterol* 10, 34.
- Nicola S, Wang Y, Nyberg SL (2016) Cell therapy in chronic liver disease. *Curr Opin Gastroenterol* 32, 189-194.
- Nyengaard Jft Goodersen HJG (2006) Sampling for stereology in lungs. *Eur Respir J* 15, 107-114.
- Jack EM, Bentley P, Bieri F, et al. (1990) Increase in hepatocyte and nuclear volume and decrease in the population of binucleated cells in

- preneoplastic foci of rat liver: a stereological study using the nucleator method. *Hepatology* 11, 28-297.
- 586 Analysis of size and density of porcine hepatocytes, K. L. Jun et al.
- Odad E, Bien H, Had muftuoglu A, et al. (2000) Long-term treatments with low- and high-dose olanzapine change hepatocyte numbers in rats. A stereological and histopathological study. *Arch Med Res* 40, 139-145.
- PaUadini G, fertlgnio A, Rizzo v, et al. (2012) Lobe-specific heterogeneity and matrix metalloproteinase activation after

- ischemia/reperfusion injury in rat livers. *Toxicol Pathol* 40, 722–730.
- Pandit SK, Westendorp B, De Bruin A (2013) Physiological significance of polyploidization in mammalian cells. *Trends Cell Biol* 23, 556–566.
- Park GC, Song GW, Moon DB, et al. (2016) A review of current status of living donor liver transplantation. *Hepatobiliary Surg Nutr* 5, 107–117.
- Peeters G, Debbaut C, Cornillie P, et al. (2015) A multilevel modeling framework to study hepatic perfusion characteristics in case of liver cirrhosis. *J Biomech Eng* 137, 051007.
- Peinado A, Vilda P, Quesada A, et al. (1990) Binucleated hepatocyte subpopulations in male and female rats fed with olive and sunflower oils. *Acta Stereol* 9, 3–8.
- Regev A, Berho M, Jeffers L, et al. (2002) Sampling error and intraobserver variation in liver biopsy in patients with chronic HCV infection. *Am J Gastroenterol* 97, 2614–2618.
- Richardson F, Boucheron J, Dyrhoff M, et al. (1986) Biochemical and morphologic studies of heterogeneous lobe responses in hepatocarcinogenesis. *Carcinogenesis* 7, 247–251.
- Rohr HP, L  thy J, Gudat F, et al. (1976) Stereology of liver biopsies from healthy volunteers. *Virchows Arch A Path Anat Histol* 371, 251–263.
- Romeis B (1989) *Mikroskopische Technik*, 16th edn. Munich: Urban und Schwarzenberg.
- Saxena R (2011) *Practical Hepatic Pathology: A Diagnostic Approach*. Philadelphia: Elsevier/Saunders.
- Schwen LO, Schenk A, Kreutz C, et al. (2015) Representative sinusoids for hepatic four-scale pharmacokinetics simulations. *PLoS ONE* 10, e0133653.
- Schwen LO, Homeyer A, Schwier M, et al. (2016) Zonated quantification of steatosis in an entire mouse liver. *Comput Biol Med* 73, 108–118.
- Schwier M, B  hler T, Hahn HK, et al. (2013) Registration of histological whole slide images guided by vessel structures. *J Pathol Inform* 30, S10.
- Shen MR, Droogmans G, Eggermont J, et al. (2000) Differential expression of volume-regulated anion channels during cell cycle progression of human cervical cancer cells. *J Physiol* 529, 385–394.
- Sohlenius-Sternbeck AK (2006) Determination of the hepatocellularity number for human, dog, rabbit, rat and mouse livers from protein concentration measurements. *Toxicol In Vitro* 20, 1582–1586.
- Song T (2015) Recent advances in surgical treatment of hepatocellular carcinoma. *Drug Discov Ther* 9, 319–330.
- Spear B, Jin L, Ramasamy S, et al. (2006) Transcriptional control in the mammalian liver: liver development, perinatal repression, and zonal gene regulation. *Cell Mol Life Sci* 63, 2922–2938.
- Stegemann J, Raina S, Nicholson D, et al. (2000) Comparison of analytical methods for quantitation of isolated porcine hepatocyte yields. *Tissue Eng* 6, 253–264.
- Tanami S, Ben-Moshe S, Elkayam A, et al. (2016) Dynamic zonation of liver polyploidy. *Cell Tissue Res*. In Press. DOI 10.1007/s00441-016-2427-5.
- Vinogradov AE, Anatskaya OV, Kudryavtsev BN (2001) Relationship of hepatocyte ploidy levels with body size and growth rate in mammals. *Genome* 44, 350–360.
- Vrtkova I (2015) Genetic admixture analysis in Prestice Black-Pied pigs. *Arch Anim Breed* 58, 115–121.
- Wang H, Yang YG (2012) Innate cellular immunity and xenotransplantation. *Curr Opin Organ Transplant* 17, 162–167.
- Wang B, Zhao L, Fish M, et al. (2015) Self-renewing diploid Axin2(+) cells fuel homeostatic renewal of the liver. *Nature* 524, 180–185.
- Watanabe T, Tanaka Y (1982) Age-related alterations in the size of human hepatocytes. A study of mononuclear and binucleated cells. *Virchows Arch B Cell Pathol Incl Mol Pathol* 39, 9–20.
- Wu Q, Bao J, Zhou YJ, et al. (2015) Optimizing perfusion-decellularization methods of porcine livers for clinical-scale whole-organ bioengineering. *Biomed Res Int* 2015, 785474.

Supporting Information

Additional Supporting Information may be found in the online version of this article:

Table S1. Primary stereological data on porcine hepatocytes in all samples investigated.

Příloha IV:

MALEČKOVÁ, A., Z. TONAR, P. MIK, K. MICHALOVÁ, V. LIŠKA, R. PÁLEK, J. ROSENDORF, M. KRÁLÍČKOVÁ a V. TŘEŠKA, 2019. Animal models of liver diseases and their application in experimental surgery. *Rozhledy V Chirurgii: Mesicnik Ceskoslovenske Chirurgicke Spolecnosti*. 98(3), 100–109. ISSN 0035-9351. Bez IF.

Zvířecí modely jaterních onemocnění a jejich využití v experimentální chirurgii

A. Malečková^{1,2}, Z. Tonar^{1,2}, M. P. Mik³, K. Michalová¹, V. Liška i.s, R. Pálek^{2,s}, J. Rosendorf^{2,s}, M. Kralická², V. Třeška

¹Ústav histologie a embryologie, Lékařská fakulta v Plzni, Univerzita Karlova

²Biomedicínské centrum, Lékařská fakulta v Plzni, Univerzita Karlova

³Evropské centrum excelence N-TIS, Fakulta aplikovaných věd, Západočeská univerzita v Plzni

⁴Ústav patologie, Lékařská fakulta v Plzni, Univerzita Karlova

⁵Chirurgická klinika, Fakultní nemocnice Plzeň, Lékařská fakulta v Plzni, Univerzita Karlova

Souhrn

Akutní a chronická jaterní onemocnění představují širokou skupinu chorob, které často ohrožují pacienty na životě. Pochopení mechanismů jejich započatí a progresu jaterního poškození je klíčové pro vyvíjení nových terapeutických strategií a léků. Nejvýznamnějším faktorem limitujícím studium patogeneze a progresu jaterních onemocnění je nedostatek vhodných zvířecích modelů. Do souladu s dobovou tabulací v nomotivních zvířecích modelech napodobujících jaterní onemocnění u lidí patří především skupina modelů jaterních onemocnění Tyto modely ovšem dokážou manifestovat všechny klinické aspekty jaterního onemocnění u lidí jen do omezené míry, především pro jejich omezenou anatomickou a fyziologickou podobnost s lidmi. Větší zvířecí modely reprezentované prasetem významně mění v oblasti modelování akutního jaterního onemocnění, jsou však stále využívány v modelování chronických jaterních onemocnění. Výsledky testování nových laboratorních metod do humaní medicíny jeví se jako velmi omezené. Sledování nových laboratorních metod do humaní medicíny jeví se jako velmi omezené. Sledování nových laboratorních metod do humaní medicíny jeví se jako velmi omezené. Sledování nových laboratorních metod do humaní medicíny jeví se jako velmi omezené.

Keywords: onemocnění jater - zvířecí modely - experimentální chirurgie, prasata

Summary

Animal models of liver diseases and their application in experimental surgery

A. Malečková, Z. Tonar, M. P. Mik, K. Michalová, V. Liška, R. Pálek, J. Rosendorf, M. Kralická, V. Třeška

Both acute and chronic liver diseases are frequent and potentially lethal conditions. Development of new therapeutic strategies and drugs depends on understanding of liver injury pathogenesis and progression, which can be studied on suitable animal models. Due to the complexity of liver injury, the understanding of underlying mechanisms of liver diseases and their treatment has been limited by the lack of satisfactory animal models. So far, a wide variety of animals has been used to mimic human liver disease however, none of the models include all its clinical aspects seen in humans. Rodents, namely rats and mice, represent the largest group of liver disease models despite their limited resemblance to human. On the other hand, large animal models like pigs, previously used mostly in acute liver failure modeling, are now playing an important role in studying various acute and chronic liver diseases. Although significant progress has been made the research in hepatology should continue to establish animal models anatomically and physiologically as close to human as possible to allow for translation of the experimental results to human medicine. This review presents various approaches to the study of acute and chronic liver diseases in animal models, with special emphasis on large animal models and their role in experimental surgery.

words: liver disease - animal models - experimental surgery - pig

Rozh Chir 2019;98:100-109

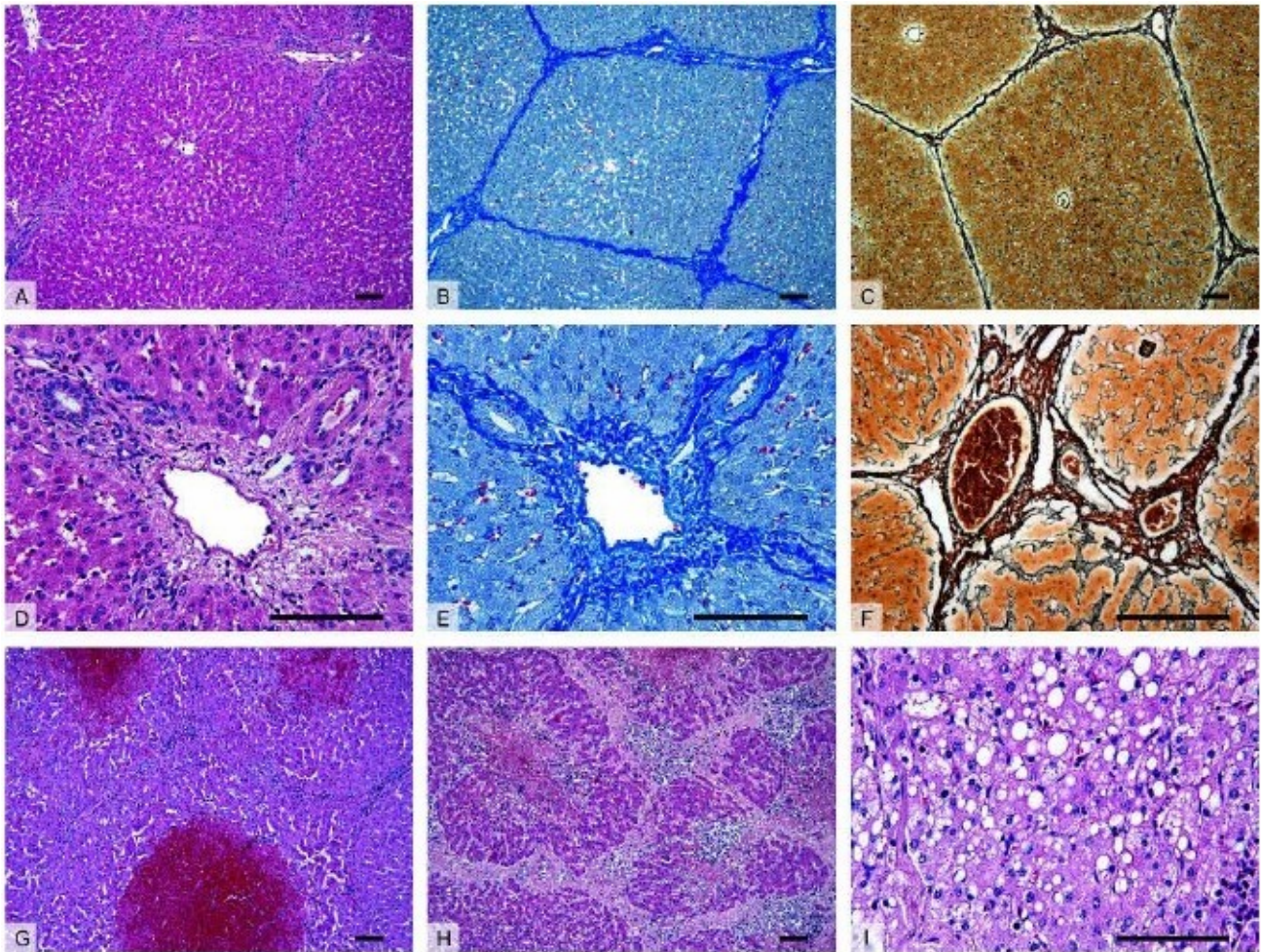
ÚVOD

Akutní jaterní onemocnění (acute hepatic injury, acute liver disease ALD) a chronická jaterní onemocnění (chronic liver disease CLO) představují širokou skupinu chorob jater s různou etiologií a mechanismem vzniku jaterního poškození. ALD mohou vyústit v akutní selhání jater (acute liver failure ALF) nebo přejít do chronicity. CLO typicky vedou k progresivní destrukci jaterního parenchymu a ve svém důsledku vyúsťují v jaterní fibrózu a cirhózu.

Navzdory pokroku v diagnostických a léčebných metodách v hepatologii stále zůstává řada nevyřešených otázek týkajících se patogeneze, progresu

a případného terapeutického ovlivnění jaterních onemocnění. Jednou z vhodných cest ke zkoumání těchto mezer v poznání je experimentální využití zvířecích modelů jaterních onemocnění.

Do současné doby byly formou přehledných sdělení zmapovány oblasti zvířecích modelů akutních i chronických jaterních onemocnění [1-5]. ALD i CLO jsou nejčastěji modelovány na malých laboratorních savcích, kteří se uplatňují zejména díky své snadné genetické manipulovatelnosti, krátkému životnímu cyklu (dospějí v případě CLO do stadia fibrózy či cirhózy [5]) a cenové dostupnosti. Ovšem jejich malá anatomická a fyziologická podobnost s člověkem omezuje aplikovatelnost výsledků studií do humaní medicíny. Proto



Obr.1: Histolog ický obraz zdravých (A-F) a patologicky změněných jater prasete (G-I)

A-C- Přehledné zvětšení zobrazující jaterní parenchym členěný v jednotlivé jaterní lobuly, které jsou u prasete ohraničené oproti člověku významně větším množstvím vaziva.

D-F- Detail portobulí a jejich prostorů obsahujících hepatickou triasu - interlobulární větevce, hepatická propria, v. portae a žlučovodu.

G- Centrilobulární hemoragická nekróza u zvířete se sinusoidálním obstrukčním syndromem vyvolaným experimentální aplikací lizidinového alkaloidu monocrotalínu.

H - Nodulární transformace jaterní tkáně s porušenou mikrostrukturou jater a typicky zmnoženým interlobulárním vazivem u jaterní cirhózy.

I - Steatóza jater charakterizována nahromaděním tukových vakuol v cytoplazmě hepatocytů v důsledku toxického poškození jater.

Barvení: hematoxylin a eosin - přehledné barvení (A, D, G-1), a nitrobojádrová červená - detekce kolagenového vaziva (B, E), stříbrná impregnační metoda (C, F) - detekce retikulárních vláken. Měřítka: 100 μm.

Staining: hematoxylin and eosin staining (A, D, G-1), aniline blue staining, counterstained with nuclear fast red - detection of collagen connective tissue (B, E), silver impregnation technique - detection of reticular fibers.

Scale bars: 100 μm.

Fig. 1: Histology of healthy (A-F) and diseased (G-I) porcine liver

A-C- The liver parenchyma divided into morphological hepatic lobules in pigs the lobules are demarcated by a significantly higher amount of connective tissue when compared to human.

D-F- Detail of portal tracts containing bile ducts and branches of the hepatic artery and portal vein surrounded by connective tissue.

G - Centrilobular hemorrhagic necrosis seen in animal with Sinusoidal Obstruction Syndrome experiment included the application of alkaloid monocrotaline.

H - Cirrhotic liver histologically represented by nodular transformation of liver parenchyma with disruption of liver microarchitecture and excessive amount of interlobular connective tissue.

I - Steatosis characterized by lipid droplet accumulation within hepatocytes caused by toxic liver injury.

Staining: hematoxylin and eosin staining (A, D, G-1), aniline blue staining, counterstained with nuclear fast red - detection of collagen connective tissue (B, E), silver impregnation technique - detection of reticular fibers.

Scale bars: 100 μm.

jsou zde tendence provádět experimenty pC. vodně s malými savci na modelech relevantnějších pro lidskou medicínu, jako např. na praseti [6], jehož játra jsou do velké míry anatomicky a histologicky podobná lidským (Obr. 1).

Naproti tomu v oblasti modelování ALF převážně velké zvířecí modely, které umožňují napojení na mimotělní oběh, opakované odběry krve a jsou vhodné pro nácvik chirurgických technik, které jsou na rozdíl od mikrocirurgických technik používaných na lodavcích

Tab. 1: Srovnání zvířecích modelů jaterních onemocnění
Tab. 1: Comparison of animal models of liver diseases

		Bezpečnost	Výhody	Nevýhody
Velké zvířecí modely	prase	anatomicky a fyziologicky podobné lidem	vysoká cena	nutnost aplikace opakovaných dávek hepatotoxických látek
	pes	akutní selhání jater	možnost opakovaných odběrů krve napojení na mimotělní oběh návlek chirurgických technik	dlouhá doba potřebná k rozvoji CLD
Malé zvířecí modely	myš	akutní jaterní onemocnění	krátká doba potřebná k rozvoji CLD	anatomicky a fyziologicky málo podobné lidem
	potkan králík	chronická jaterní onemocnění	levné možnost genetické modifikace	velikost neumožňující opakované odběry krve napojení na mimotělní oběh

Vywm/ivky:CUJ-chronickéjaterníonemocnění/(chronic liver disease).

je však méně náročná na dovednosti operátora, ale především bližší chirurgické praxi (Tab. 1).

V literatuře nacházíme množství způsobů dělení zvířecích modelů jaterních onemocnění, které se do jisté míry překrývají a duplikují. Liu et al. [4] navrhl rozdělení modelů CLD dle mechanismu vzniku jaterní fibrózy a cirhózy na (i.) klasické modely: neberou v potaz etiologii jaterního poškození, aplikaci hepatotoxických látek dosahují u zvířat jaterní fibrózy, (ii.) modely napodobující specifická jaterní onemocnění: kladou důraz na etiologii CLD, kterým významným způsobem ovlivňuje patogenezi, progresi a prognózu CLD. Poněkud přehlednějším je zde navržené dělení, které zahrnuje většinu možností modelování jak akutního, tak chronického jaterního poškození (Tab. 2).

Cílem tohoto sdělení je představit zvířecí modely jaterních onemocnění a jejich současné využití v experimentu. Pro zachování kompatibility se zahraničními zdroji ponecháváme vedle některých pojmů v češtině i jejich ustálené protějšky v anglickém jazyce.

Tab. 2: Přehled zvířecích modelů jaterních onemocnění
Tab. 2: List of animal models of liver diseases

Akutní selhání jater (ALF)

- Chirurgické modely
- Farmakologické modely
- Infekční modely

Toxické poškození jater

- Chemicky indukované modely
- Lékové poškození jater

Alkoholové poškození jater

Modely imitující specifická jaterní onemocnění

- Modely autoimunitní hepatitidy (AIH)
- Modely primární biliární cirhózy (PBC)
- Modely primární sklerozující cholangitidy (PSC)
- Modely nealkoholické steatózy jater (NAFLD) a steatohepatitidy (NASH)
- Modely virové hepatitidy

Invazivní model jaterní fibrózy

Geneticky modifikované

myš

1. Zvířecí modely akutních a chronických jaterních onemocnění

Následující text shrnuje vybrané modely zvířecích modelů akutních a chronických jaterních onemocnění na základě literární rešerše. Rešerše byla provedena v databázi PubMed k datu 30. 8. 2018 s využitím klíčových slov: acute liver failure, chronic liver disease, animal models. Přehledná sdělení (review) byla následně doplněna o konkrétní studie s využitím klíčových slov nalezených v literatuře, např.: acetaminophen, acute liver failure, animal model, pig. V předkládaném článku jsou uvedena jak přehledná sdělení (review) na dané téma, tak příklad studií, které využily zvířecí model ke konkrétním experimentům, např. k testování podpůrných jaterních systémů (Tab. 4). Zahrnuty byly zejména studie prasečími modely jaterních onemocnění.

1.1 Modely akutního jaterního selhání

Navzdory vysoké regenerační kapacitě hepatocytů a možnost spontánního návratu jaterních funkcí zůstává pro pacienty s ALF bez uspokojuvící regenerace jedinou terapeutickou možností ortotopická transplantace jater (orthotopic liver transplantation OLT). Ve většině případů OLT zlepšuje celkové přežití, ovšem počet pacientů na čekací listině pro transplantaci neustále přibývá [1]. Zlepšení regenerační kapacity jater lze dosáhnout artérializací portální vlny (portal vein arterialization PVA), jak bylo testováno v experimentu na potkanech [7] a prasatech [8]. Současné léčebné možnosti používané k překlenutí čekací doby na OLT (tzv. bridging) jsou omezené a zahrnují transplantaci hepatocytů [9] a využití podpůrných jaterních systémů, tzv. umělých jater (liver support systems) [10,11].

Pokusy o vysvětlení patofyziologických procesů a propojení metabolických změn s klinickými projevy ALF vyústily ve formulování dvou teorií: toxin hypothesis a. critical mass theory. Toxin hypothesis" předpokládala, že klinické projevy ALF jsou zodpovědné nahromaděné látky jako např. amoniak, fenoly či volné žlučové kyseliny, které jsou v zdravých játrech odbourávány. Critical mass theory pak za příčinu jaterního selhání považovala ztrátu hepatocytů pod určitou kritickou mez, kdy již játra nejsou schopna udržovat svou

Tab. 3: Kritéria pro ideální zvířecí model akutního selhání jater (ALF) - převzata a upraveno dle Terblanche a Hickman (13)
 Tab.3: Criteria for an ideal animal model of acute liver failure, (ALF) postulated by Terblanche and Hickman (13)

Kritérium	Charakteristika
Vratnost - reversibility	Při zavedení vhodné léčby by mělo být ALF potenciálně reverzibilní a model by měl při adekvátní léčbě přežít.
Opakovatelnost- reproducibility	Model musí být jednoduše reprodukovatelný.
Smrt z příčin jaterního selhání- death from liver failure	Měly by být přítomny biochemické, histologické a klinické změny od rážejší průběh jaterního selhání lidí a jaterní poškození by mělo být přímo k smrti modelů.
Terapeutické okno- therapeutic window	Mezi inzultem a úmrtím zvířete musí být dostatečný čas k nasazení a posouzení efektu léčby.
Velký zvířecí model - large animal model	Velikost zvířete musí umožňovat pravidelné odběry krve a aplikaci mimo tělního oběhu a model by měl být anatomicky a fyziologicky co nejblíže lidem.
Bezpečnost - minimal risk for personnel	Použití techniky a toxinů musí představovat minimální riziko pro personál.

metabolickou aktivitu na takové úrovni, aby dokázala zajistit podporu funkce dalších periferních orgánů. Hlubší studium problematiky ALF ovšem ukázalo, že mechanismus nahromadění toxických látek a ztráty syntetické kapacity jater nejsou jedinými mechanismy a že vlastní poškozené hepatocyty se podílejí na

prohloubení a progresi ALF uvolňováním zánětlivých

cytokinů či vazoaktivních látek [12]. Přesto dodnes zůstávají některé mechanismy ALF nepopsány. Studium patogeneze ALF a testování nových terapeutických přístupů z hlediska jejich bezpečnosti a efektivity je proto nezbytné etablovat zvířecí model, který bude co nejvíce reflektovat průběh ALF u člověka.

Terblanche a Hickman [13] počátkem 90. let navrhli systém šesti kritérií, která by měl ideální zvířecí model ALF splňovat (Tab. 3). V současnosti žádný zvířecí model ALF nespĺňuje všechna popsaná kritéria. Pro vytvoření modelu ALF se využívají tři hlavní přístupy: chirurgický, farmakologický (toxický) a infekční model [1-3].

1.1.1 Chirurgické modely ALF

Chirurgické modely s výhodou využívají velká zvířata. Rozdělují se do 3 základních skupin: velká resekce (partial hepatectomy), hepatektomie (anhepatic model) a ischemický model (ischemie model, devaskularizace) (Tab. 4).

Modely velké jaterní resekce jsou pro svoji náročnost provedení, jež závisí na technickém vybavení a zkušenostech operátorů, těžko reprodukovatelné. Alternativou k prosté resekcii může být kombinace resekce s ischémii zbytků jaterního parenchymu [14].

Anhepatický model zahrnuje odstranění celého orgánu [1,5] je oproti předchozímu snadněji repro-

dukovatelný. Pro jeho využití v experimentu je mimo jiné důležitá i pooperační intenzivní péče: monitorování hemodynamických parametrů, zajištění ventilace, monitorování a případná úprava mikce, monitorování množství hemoglobinu, hematokritu a laktátu, elektrolytů v séru, acidobazické rovnováhy, krevních plynů a hladiny glukózy které ovlivňují délku přežití zvířete, a tedy i délku terapeutického okna pro použití a testování nových léčebných strategií [16].

Ischemický model představuje dvoustupňový chirurgický výkon, při kterém se vytváří portální shunt s následným uzávěrem hepatické arterie [17]. Okluzí se dočasně, pak je model potenciálně reverzibilní, ovšem průběh ALF je značně nestálý a těžko reprodukovatelný. Jiným přístupem k vytvoření ischemického modelu je přerušovaná okluze v. portae a a. hepatica následnou arteriální ligací [18]. Tento model splňuje všechna kritéria dle Terblanche a Hickmana s výjimkou reverzibility [13].

Tab. 4: Přehled chirurgických modelů akutního selhání jater a jejich současné využití v experimentu na prasati
 Tab. 4: Surgical models of acute liver failure and their current application in experimental research on pigs

Typ modelu	Klinická relevanc	Výhody	Omezení	Využití prasečího modelu v experimentu
Velká jaterní resekce	resekční výkon		technicky náročné	
Partial hepatectomy	pronádorové onemocnění hepatektomie pro rozsáhlé	reverzibilita	nereprodukovatelné ireverzibilní	studium regenerace [48]
Hepatektomie Anhepatic model	trauma či akutní resekci orgánu po	transplantaci		reprodukovatelnost vyloučení vliv poškozených

hBAL [49]

e
p
a
t
o
c
y
t
ů
n
a
p
r
o
g
r
e
s
i
A
L
F

Ischem ický mo de l

dočasná ischémie

reverzibilita

nere produkovatelný

BAL [SOJ

Ischem ie mod el

přiOLT

krátké přežití

1/)'SVM/ivl<y:Ol.T- onotopickátransplantacejater (orthotopic/ivertransplantation),BAL- bioartmcial Hver.

podpCJrných systémů. Nejvýznamnějšími toxiny, jejichž účinky byly studovány na řadě zvířecích druhů a které jsou v současnosti používány k vývoji modelu ALF, patří: galaktosamin [22], acetaminofen [23] a tetrachlormethan [8, 24] (Tab. 5).

1.1.3 Infekční modely

Navzdory tomu, že virové hepatitidy jsou celosvětově jednou z nejčastějších příčin jaterního selhání, byly snahy o vytvoření zvířecího modelu na podkladě infekce dlouhou dobu neúspěšné. Myší modely hepatitidy B přispěly ke studiu patogeneze ALF, ovšem tentomá zvířecí model neumožňoval opakované krevní rozbory a připojení namísto tělní eliminační metody. Z tohoto důvodu se infekční modely prozatím ve studiu ALF neuplatnily.

1.2 Modely toxického poškození jater

Játra hrají zásadní roli v biotransformaci a eliminaci

Tab. 7: Zvířecí modely specifických jaterních onemocnění
 Tab. 7: Animal models mimicking specific chronic liver diseases

Onemocnění	Kritéria {"wish list"} pro ideální model	W...:W	Princip modelu
Autoimunitní hepatitida AIH[26]	přítomnost auto protilátek (ANA, ASMA) chronický zánět přechodem do fibrózy přítomnost antigenně-specifických T-lymfocytů přítomnost nekroz na histologickém vyšetření	myš králík	indukované modely geneticky modifikované spontánní modely geneticky modifikované indukované modely přenos antigenů pomocí virů
Primární biliární cirhóza PBC[29]	převaha rozvoje PBC u samiček přítomnost auto protilátek (AMA) chronický zánět malých a střední intrahepatálních žlučových floridní duktální reakce na histologickém vyšetření	myš	geneticky modifikované spontánní modely modely vyvolané environmentálními faktory geneticky modifikované autoimunitní modely
Primární sklerotizující cholangitida PSC[35]	převaha rozvoje PSC u samců progresivní zánět intra- a extrahepatálních žlučových koncentrická periduktální fibróza (onion skinning) na histologickém vyšetření přítomnost nespecifického zánětu střev (UC) přechod do cholangio karcinomu	potkan myš	chemicky indukované modely modely využívající infekční agens geneticky modifikované modely model GVHD
Nealkoholická steatóza a steatohepatitida HAFL0, NASH (37)	obezita Oslipiclémie inzulinová rezistence steatóza, zánět balonová degenerace hepatocytů progresují ve fibrózu na histologickém vyšetření přechod do HCC	myš potkan	'dietary models' MCD diet CDA diet atherogenní diet a high-fat diet a její variace geneticky modifikované modely
Virová hepatitida B a C HBV [46] a HCV (45)	vřímavost k infekci replikace viru v organismu imunitní odpověď srovnatelná s lidmi Progrese do cirhózy přechod do HCC	šimpanz myš	šimpanzí modely myši exprimující virové proteiny

W) WMI<y: AJ/A - antinukleární auto protilátky, ASMA - auto protilátky proti hladkým svalům / avjmbuňkdm, AMA - anti-mitochondriální protilátka, UC - ulcerózní kolitida, HCC - hepatocelulární karcinom, GVHD - reakce štěpu proti hostiteli, MCD diet - methionine and choline deficiency diet, CDA diet - choline-deficient L-amino acid-defined diet.

exogenních látek, jejichž nadměrnou expozicí často dochází k jaternímu poškození. Opakované aplikace hepatotoxických látek představují klasický způsob indukce jaterní fibrózy u experimentálních zvířat. V závislosti na způsobu podávání ale mohou hepatotoxické látky místo jaterní fibrózy způsobit akutní jaterní poškození, až selhání (viz kapitola 1.1.2 Farmakologické modely ALF) (Tab. 5).

Z preventivního hlediska lze hepatotoxické látky a tedy i zvířecí modely toxického poškození jater, dělit do dvou kategorií: (i.) skutečné hepatotoxiny - jejich podání vyvolá poškození jater u všech jedinců, jde především o produkty chemického průmyslu jako tetrachlormethan, CA, thioacetamid (TAA), dimethylnitrosamin (DMN) a diethylnitrosamin (DEN) - a (ii.) potenciální hepatotoxiny - vyvolají poškození jater jen u části jedinců, jedná se především o léky, např. chemoterapeutika (Tab. 6). Zvláštní kapitolu tvoří alkoholové poškození jater.

1.2.1 Alkoholové poškození jater

Nadměrná konzumace alkoholu, ať už akutní, chronická, je závažným sociálním, ekonomickým i zdravotním problémem. Alkoholové poškození jater zahrnuje

stavy od poměrně nezávažné steatózy až po cirhózu jater s možností vzniku hepatocelulárního karcinomu.

Alkoholové poškození jater se nejčastěji modeluje na myších a potkanech. Nejrozšířenějším modelem je chronické podávání alkoholu (Lieber- DeCarli liquid diet; LD diet), chronická intragastrická aplikace alkoholu nebo kombinace podávání alkoholu se specifickou dietou (high-fat diet), s hepatotoxickými látkami nebo u geneticky modifikovaných myší [25].

1.3 Modely imitující specifická jaterní onemocnění

Společným znakem většiny chronických jaterních onemocnění je jejich vliv na histologickou stavbu jaterního parenchymu se vznikem jaterní fibrózy až cirhózy. Etiologické a patogenetické mechanismy zodpovědné za tyto změny se ovšem u jednotlivých specifických jaterních onemocnění liší a často je ani neznáme. Vytvoření zvířecích modelů je tak komplikováno nejen neznalostí etiopatogeneze onemocnění, ale také tím, že některé choroby se vyskytují pouze u lidí (virové hepatitidy). Prozatím se nedaří modely, které by měly všechny atributy lidského onemocnění, vytvořit (Tab. 7). Navzdory tomu jsou zvířecí modely specifických jaterních onemocnění ideálním nástrojem k pochopení vzniku a progresu CLO a k nalezení jejich účinné léčby.

13.1 Modely autoimunitní hepatitidy (autoimmune hepatitis AIHJ)

AIH je chronické zánětlivé onemocnění jater neznámé etiologie charakterizované přítomností autoantikörperů, histopatologickými změnami v játrech a klinickými příznaky vyplývajícími z jaterního poškození - únava, letargie, méně často ikterus. Charakteristickým diagnostickým klinickým znakem AIH je rychlá odpověď na imunosupresivní léčbu, která se vyskytuje asi u 90 % pacientů. Léčba AIH je založena na imunosupresivní terapii.

Zvířecí modely AIH lze vytvořit několika způsoby. V období předmožnosti genetické manipulace modelových organismů se AIH indukovala aplikací jaterních antigenů, nebo rostlinného lektinu concavalinu A, který nespecificky aktivuje *T-lymfocyty* a vede k poškození jater. Velkou skupinu modelů AIH ovšem představují geneticky modifikované myšičí modely [26] (Tab. 7).

13.2 Primární biliární cirhóza (primary biliary cirrhosis PBC)

PBC je chronické cholestatické onemocnění postihující malé a střední intrahepatální žlučové cesty a objevující se nejčastěji u žen středního věku (vpátě a šesté dekádě života). Klasická forma PBC je spojena s přítomností anti-mitochondriálních protilátek v séru [27]. Aspekty ovlivňující etiologii ovšem zatím zůstávají neznámé a studie se zaměřují zejména na vnitřní, ale i environmentální faktory v rozvoji onemocnění [28]. Do současné doby bylo ke studiu etiopatogeneze a interakce možných genetických a environmentálních faktorů vytvořeno množství zvířecích modelů PBC (myši) [29]. PBC u těchto modelů vzniká buď spontánně u geneticky modifikovaných myší [30-32] nebo je indukována působením environmentálních faktorů na zvíře, jako je expozice xenobiotikům (např. 2-octynoic acid (2-OA) [32]) nebo působením infekčních agens [33].

13.3 Primární sklerozující cholangitida (primary sclerosing cholangitis PSC)

Primární sklerozující cholangitida (primary sclerosing cholangitis PSC) patří mezi další chronické zánětlivé onemocnění jater postihující intra- a extrahepatické žlučové cesty a pomalu může progredovat k biliární cirhóze a jaternímu selhání. PSC se často vyskytuje u pacientů s nespecifickým střevním zánětem, zejména s ulcerózní kolitidou [34]. Klinické a laboratorní nálezy jako T-lymfocytární infiltrace v okolí cílových žlučových ductů, přítomnost autoantikörperů pANCA (perinukleární autoantikörperů proti cytoplasmě neutrofilů, perinuclear antineutrophil cytoplasmic antibodies) a spojitost s určitými HLA haplotypy a dalšími autoimunitními chorobami (UC) svědčí o autoimunitně zprostředkovaném mechanismu vzniku a progresu onemocnění. Ovšem v porovnání s jinými autoimunitními chorobami PSC špatně reaguje na imunosupresivní léčbu, vyskytuje se častěji u mužů (2-3:1) a je zde jen slabá korelace mezi hladinou sérových autoantikörperů s klinickými a laboratorními nálezy.

Pollheimer a Fickert [35] rozdělují zvířecí modely PSC do několika skupin dle mechanismu indukce onemocnění.

2. Žádný z modelů ovšem ještě nezodpovídá všem otázkám týkajícím se etiogeneze a progresu onemocnění.

13.4 Nealkoholická steatóza jater (non-alkoholic fatty liver disease NAFLD) a nealkoholická steatohepatitida

(non-alkoholic steatohepatitis NASHJ)

NAFLD je v současné době nejčastějším chronickým progresivním jaterním onemocněním v rozvinutém světě jehož prevalence se odhaduje až na 30 % populace. Většinou (případ.) je NAFLD úzce spojená s nadváhou a obezitou a s ní spojeným metabolickým profilem, a to především s inzulínovou rezistencí. Pokud jsou v játrech současně přítomny steatóza, zánět a poškození hepatocytů (balonová degenerace, ballooning), hovoříme o NASH, která může být doprovázena progresivní fibrózou a je spojena s vyšším rizikem vzniku hepatocelulárního karcinomu.

Nejlépe popsány a nejčastěji používanými modely NAFLD jsou tzv. dietary models, kde je navozeno jaterní poškození změnami ve stravě modelového organismu. Různé typy diet jsou pro zvířecí modely NASH klíčové. Představují buď vlastní příčinu NASH, nebo slouží jako spouštěče jaterního poškození geneticky modifikovaných modelů. Diety jsou založeny buď na kaloricky bohaté stravě - fruktózová dieta, high-fat diet (HFD) - nebo na deficitu určitých živin podílejících se na správném metabolismu tuků - methionine and choline deficient diet (MCD diet), choline-deficient L-amino acid-defined diet (CDAA diet). Z geneticky modifikovaných modelů, je nejčastěji uplatňují modely myší s diabetem [36,37].

13.5 Modely virové hepatitidy

Studium virové hepatitidy B a C bylo dlouho omezeno na *in vitro* podmínky nebo na studie probíhající na jediném zvířeti, které je k infekci těmito hepatotropními viry vnímavé - na šimpanzovi [38,39]. Šimpanzí model hrál klíčovou roli při studiu interakce hostitel-virus a bylo na něm možno testovat první antivirové strategie v léčbě infekce. Přelomovým objevem bylo objevení buněčných receptorů pro HBV a HCV, díky nimž bylo možné vytvořit buněčné linie pro studium životního cyklu a jednotlivých virových komponent *in vitro*. Základních strategií tvorby *in vivo* myšičích modelů virové infekce je několik. Jednou z nich je expresivní virových proteinů, nebo receptorů pro lidské viry samotnými hepatocyty u transgenních myší [40]. Další možností je vytvoření chimerických myší, a to transplantací lidských hepatocytů do imunodeficientních myší [41,42]. Imunodeficientní organismy ovšem nedovolují studium imunitních mechanismů. Z tohoto důvodu byly vyvinuty imunokompetentní modely (potkan), kterých bylo dosaženo současnou transplantací lidských krvevorných kmeňů nových buněk [43,44].

V současnosti máme tedy k dispozici množství modelů jak pro preklinické testování antivirové terapie (imunodeficientní) tak pro studium imunitní odpovědi na léčbu (imunokompetentní). Žádný z modelů, ovšem nespĺňuje všechna kritéria pro ideální model, a to zejména přechod do chronicity se vznikem jaterní cirhózy a eventuálně HCC [45,46].

1.4 Invazivní model jaterní fibrózy

Podvaz *ductus hepaticus communis* (bile duct ligation (BDL)) je invazivní metodou vyvolání sekundární biliární cirhózy. Obstrukce toku žlučové kyseliny způsobuje intrahepatální cholestázu, proliferaci žlučových cest, zánět v portobiliárních prostorech a fibrózu a vede ke vzniku sekundární biliární cirhózy a jaternímu selhání. BDL se provádí u potkanů, kteří nemají žlučník [47].

1.5 Geneticky modifikované myši jako zvířecí

modely jaterních onemocnění

Geneticky modifikované myši se používají k modelování jaterní fibrózy kdy vyřazení specifických genů nebo naopak jejich over-exprese umožňuje studium

jejich fibrogenního nebo antifibrogenního vlivu exprimovaných faktorů [5]. Transgenické myši se uplatňují i při modelování nespecifických jaterních onemocnění, jak je uvedeno v předchozích kapitolách.

ZÁVĚR

Snahy vytvoření zvířecích modelů jaterních onemocnění probíhají již několik desetiletí s většími a menšími úspěchy o přiblížení průběhu jaterních chorob u lidí. Největší skupinu tvoří malé zvířecí modely reprezentované myši a potkany, které využívají nejčastěji ke studiu etiopatogeneze a progresu onemocnění. Testování (NCN) dle terapeutické

přístupů, a to jaklékeli, tak invazivních metod, je ovšem z těchto modelů jenomezeně přenositelné do humánní medicíny.

Na druhou stranu velké zvířecí modely, zektel) dle je často používaným modelem prase, představují spojující d'ánek mezi experimentální medicínou a klinickou praxí. Uplatňují se zejména ke studiu akutního selhání jater (Tab. 1), kde je **el-**

ke zvířecím zásadním kritériím ideálního modelu, a stále častěji přivývoji nových chirurgických přístupů a invazivních terapeutických metod, jako jsou podpůrné jaterní *systemy*.

Využití anatomické a fyziologické podobnosti jater prasete játry člověka může být s výhodou využito při přenosu výsledků experimentálních výzkumů do humánní klinické medicíny. Vývoj nových velkých zvířecích modelů jaterních onemocnění např. v oblasti autoimunitních jaterních onemocnění, je ovšem zatížen řadou nevýhod spojených s prací s velkými zvířaty. Menší počet jedinců

v porovnávaných skupinách ztěžuje statistické vyhodnocení experimentů s možným ovlivněním výsledků značnou interindividuální variabilitou. Oproti laboratorním hlodavcům by ale prasecí modely chronických jaterních onemocnění mohly přinést nové poznatky o mechanismech způsobujících jaterní poškození a umožnit tak přesnější diagnostiku účinnější léčbu u našich pacientů.

Seznam zkratk

AIH - autoimunitní hepatitida, autoimmune

Rozhledy v chirurgii 2019, roč. 98 / 3

APAP	- acetaminophen
ASH	- alkoholová steatohepatitida (alcoholic steatohepatitis)
ASMA	- autoprotilátka proti hladkým svalovým buňkám, anti-smooth muscle antibodies
BAL	- bioartificial liver
BOL	- podvaz <i>ductus hepaticus communis</i> , bile duct ligation
CASH	- steatohepatitida spojená s chemoterapií, chemotherapy-associated steatohepatitis

(DAA) diet	- choline-deficient L-amino acid defined diet
CCI,	- tetrachloroethane
CLO	- chronická jaterní onemocnění, chronic liver disease

DEN	- diethylnitrosamin
DNM	- dimethylnitrosamin
GVHD	- reakce štěpu proti hostiteli, graft versus host disease

HBV	- virus hepatitidy B, hepatitis B virus
HCC	- hepatocelulární karcinom, hepatocellular carcinoma

HCV	- virus hepatitidy C, hepatitis C virus
HFD	- dieta bohatá na tuky, high-fat diet
MCD diet	- methionine and choline deficiency diet
MSC	- mezenchymální kmenové buňky, mesenchymal stem cells

NAFLD	- nealkoholická steatóza jater, non-alcoholic fatty liver disease
-------	---

NAPQI	- N-acetylparabenzochinonimin
NASH	- nealkoholická steatohepatitida, non-alcoholic steatohepatitis

NO	- oxid dusnatý, nitric oxide
OLT	- ortotopická transplantace jater, orthotopic liver transplantation

pANCA	- perinukleární autoprotilátky proti cytoplasmě neutrofilů, perinuclear anti-neutrophil cytoplasmic antibodies
-------	--

PBC	- primární biliární cirhóza, primary biliary cirrhosis
PSC	- primární sklerozující cholangitida, primary sclerosing cholangitis
PI/A	- arteriální portální trombóza, portal vein arterialization
TAA	- thioacetamid

hepatitis

ALD	- akutní jaterní onemocnění, acute liver disease
ALF	- akutní selhání jater, acute liver failure
AMA	- antimitochondriální protilátky, anti-mitochondrial antibodies
ANA	- antinukleární protilátky, antinuclear antibodies

UC - ulcerózní kolitida , ulcerativecolitis

Podpora:

Program rozvoje vědních oborů Univerzity
Karlovy {Progres Q39
) ; Národní program udržitelnosti I
(NPU) č. LOI503 poskytnutý Ministerstvem
školství, mládeže a tělovýchovy; SW
260390 Univerzity Karlovy
Univerzitní výzkumná cen- tra
UK UNCE/006. Univerzitní centrum
klinické a experimentální jaterní chirurgie
Projekt Aplikace moderních technologií v
medicíně a průmyslu reg.č: U. 02.1.0 1/0.0/0.
0/17_048/0007280 financovaného z EFRR.

Konflikt zájmů

Autoři článku prohlašují, že nejsou v
souvislosti se vznikem tohoto článku
vestřet zájmů a že tento článek
nebyl publikován v žádném jiném časopise

LITERATURA

1. Van Oe Kerkhove MP, Hoekstra R, Van Gulik TM, et al. Large animal models of fulminant hepatic failure in artificial and bioartificial liver support research. *Biomaterials* 2004;25:1613-25.
2. Rahman TM, Hodgson HI. Animal models of acute hepatic failure. *Int J Exp Pathol* 2000;81:145-57.
3. Newsome PN, Plevris JN, Nelson U, et al. Animal models of fulminant hepatic failure: a critical evaluation. *Liver Transpl* 2000;6:21-31.
4. Yu Y, Meyer C, Xu C, et al. Animal models of chronic liver diseases. *AJP Gastrointest Liver Physiol* 2013;304:G449-68.
5. Starkel P, Leclercq IA. Animal models for the study of hepatic fibrosis. *Best Pract Res Clin Gastroenterol* 2011;25:319-33.
6. Plek R, Lillka V, Tielka V, et al. Sinusoidal obstructions syndrome induced by monocrotaline in a large animal experiment - a pilot study. *Rozhl Chir* 2018;97:214-21.
7. Fan YD, Praet M, van Huysse J, et al. Effects of portal vein arterialization on liver regeneration after partial hepatectomy in the rat. *Liver Transplant* 2002;8:152.
8. Zuo A, Cannist M, Vallari G, et al. Liver regeneration induced by extracorporeal portal vein arterialization in a swine model of carbon tetrachloride intoxication. *Transplant Proc* 2015;47:21HS.
9. Hughes RO, Mistry RR, Ohawan A. Current status of hepatocyte transplantation. *Transplantation* 2012;93:342-7.
10. Laleman W, Mime A, Evenepoel P, et al. Review article: No biological liver support in liver failure. *Aliment Pharmacol Ther* 2006;23:351-63.
11. Ryska O, Pantoflík T, Ušáková E, et al. Souřasný význam biologických a nebiologických elimináčních metod v léčbě akutního selhání jater. *Rozhl Chir* 2008;87:291-6.
12. Los M-R, Pajen O. Mechanisms of liver damage. *Semin Liver Dis* 1996;16:357-67.
13. Terblanche J, Hickman R. Animal models of fulminant hepatic failure. *Organs Sci* 1991;36:770-4.
14. Ladurner R, Hochleitner B, Schneeberger S, et al. Extended liver resection and hepatic ischemia in pigs: A new, potentially reversible model to induce acute liver failure and study artificial liver support systems. *Eur Surg Res* 2005;37:365-9.
15. Sosef MN, Van Gulik TM. Total hepatectomy model in pigs: Revised method for vascular reconstruction using a rigid vascular prosthesis. *Eur Surg Res* 2004;36:8-12.
16. Thiel C, Thiel K, Elspueker A, et al. Standardized intensive care unit management in an anhepatic pig model: new standards for analyzing liver support systems. *Crit Care* 2010;14:R138.
17. Nieuwoudt M, Kunnik R, Smuts M, et al. Standardization criteria for an ischemic surgical model of acute hepatic failure in pigs. *Biomaterials* 2006;27:3836-45.
18. Lee KU, Zheng L, Cho YB, et al. An experimental animal model of fulminant hepatic failure in pigs. *J Korean Med Sci* 2005;20:427-32.
19. Saracyn M. Hepatoprotective effect of nitric oxide in experimental model of acute hepatic failure. *World J Gastroenterol* 2014;20:17407.
20. Carvalho NR, Tassi CC, Oobraschinski F, et al. Reworsing of bioenergetic dysfunction by diphenyl diselenide is critical to protection against the acetaminophen-induced acute liver failure. *Ufe Sci* 2017;180:42-50.
21. Zhang S, Zhu Z, Wang Y, et al. Therapeutic potential of Barna miniature pig adipose stem cells induced hepatocytes in a mouse model with acute liver failure. *Cytotechnology* 2018;70:131-41.
22. Kalpana K, Ong HS, Soo KC, et al. An improved model of galactosamine-induced fulminant hepatic failure in the pig. *JSurg Res* 1999;82:211-30.
23. Thiel C, Thiel K, Elspueker A, et al. A reproducible porcine model of acute liver failure induced by intrajugular acetaminophen administration. *Eur Surg Res* 2011;46:118-26.
24. Nayak NC, Chopra P, Ohar A, et al. Overview of mechanisms of hepatocellular injuries due to chemicals: evidence in rats administered carbon tetrachloride or dimethylnitrosamine. *Br J Exp Pathol* 1975;56:103-12.
25. Ghosh Oastidar S, Wamer J, Wamer O, et al. Rodent models of alcoholic liver disease: Role of binge ethanol administration. *Biomolecules* 2018;8:3.
26. Christen U, Holdener M, Hintermann E. Animal models of autoimmune hepatitis. *Autoimmun Rev* 2007;6:306-11.
27. Oertelt S, Rieger R, Selmi C, et al. A sensitive bead assay for anti-mitochondrial antibodies: Chipping away at AMA-negative primary biliary cirrhosis. *Hepatology* 2007;45:659-65.
28. Tanaka A, Leung PSC, Young HA, et al. Towards solving the etiological mystery of primary biliary cholangitis in mice. *Hepatology* 2017;1:275-87.
29. Katsumi T, Tomita K, Leung PSC, et al. Animal models of primary biliary cirrhosis. *Oin Rev Allergy Immunol* 2015;4:8142-53.
30. Koorada S, Wu Y, Fertig N, et al. Genetic control of autoimmunity: Protection from diabetes, but spontaneous autoimmune diabetes in a nonobese diabetic congenic strain. *J Immunol* 2004;173:2315-23.
31. Oertelt S, Lian Z X, Cheng C-M, et al. Anti-mitochondrial antibodies and primary biliary cirrhosis in TGF-receptor U dominant-negative mice. *J Immunol* 2006;177:1655-60.
32. Wakabayashi K, Lian Z-X, Morooki Y, et al. IL-2 receptor α -/- mice and the development of primary biliary cirrhosis. *Hepatology* 2006;44:1240-9.
33. Wang JJ, Yang GX, Zhang WC, et al. Escherichia coli infection induces autoimmune cholangitis and anti-mitochondrial antibodies in non-obese diabetic (NOD).B6 (Idd10/Idd18) mice. *Clin Exp Immunol* 2014;175:192-201.
34. Fausa O, Schrupf E, Elgjo K. Relationship of inflammatory bowel disease and primary sclerosing cholangitis. *Semin Ultrasound Dis* 1991;11:31-9.
35. Pollheimer MJ, Fickert P. Animal models in primary biliary cirrhosis and primary sclerosing cholangitis. *Oin Rev Allergy Immunol* 2015;4:8207-17.
36. Santhelcadur PK, Kumar DP, Sanyal AJ. Preclinical models of non-alcoholic fatty liver disease. *J Hepatol* 2018;68:230-7.
37. van Herk MA, Vooghia L, Francque SM. Animal models of nonalcoholic fatty liver disease - a starter's guide. *Nutrients* 2017;9:1-13.
38. Bukh J. A critical role for the chimpanzee model in the study of hepatitis C. *Hepatology* 2004;39:1469-75.
39. Meland SF. The chimpanzee model for hepatitis B virus infection. *Cold Spring Harbor Perspect Med* 2015;5:1-19.
40. Moriya K, Fujie H, Shintani Y, et al. The core protein of hepatitis C virus induces hepatocellular carcinoma in transgenic mice. *Nat Med* 1998;4:1065-7.
41. Dandri M, Burda MR, Torok E, et al. Repopulation of mouse liver with human hepatocytes and non-infection with hepatitis B virus. *Hepatology* 2001;33:981-8.
42. Bissig K-O, Wieland SF, Tran P, et al. Human liver chimeric mice provide a model for hepatitis C and C virus infection and treatment. *J Clin Invest* 2010;120:92430.
43. Washburn ML, Bililyk MT, Zhang L, et al. A humanized mouse model to study hepatitis C virus infection, immune response, and liver disease. *Gastroenterology* 2011;140:134-44.
44. Billerbeck E, Mommersteeg MC, Shlomai A, et al. Humanized mice efficiently engrafted with fetal hepatoblasts and syngeneic immune cells develop human monocytes and NK cells. *J Hepatol* 2016;65:334-41.
45. Vercauteren K, De Jong VP, Meuleman P. HCV animal models and liver disease. *J Hepatol* 2014;61:S26-33.
46. Dandri M, Petersen J. Animal models of HBV infection. *Best Pract Res Clin Gastroenterol* 2017;31:273-9.
47. Abd El Motteleb DM, Ibrahim IAAEH, Elshazly SM. Sildenafil protects against bile duct ligation induced hepatic fibrosis in rats: Potential role for silent information regulator 1 (SIRT1). *Toxicol Appl Pharmacol* 2017;335:4-71.
48. Michalopoulos GK. Liver regeneration after partial hepatectomy. *Am J Pathol* 2010;176:2-13.
49. Abrahamse SL, Van De Kerckhove MP, Sosef MN, et al. Treatment of acute liver failure in pigs reduces hepatocyte function in a bioartificial liver support system. *Int J Artif Organs* 2002;25:966-74.
50. Lee J-H, Lee D-H, Lee S, et al. Functional evaluation of a bioartificial liver support system using immobilized hepatocyte spheroids in a porcine model of acute liver failure. *Sci Rep* 2017;7:3804. doi: 10.1038/s41598-017-03424-2.
51. Lv G, Zhao L, Zhang A, et al. Bioartificial liver system based on chondrocyte fluidized bed bioreactor improves the survival time of fulminant hepatic failure pigs. *Bio Technol Bioeng* 2011;108:2229-36.
52. Sang J-F, Shi X-L, Han B, et al. Intraportal mesenchymal stem cell transplantation prevents acute liver failure through promoting cell proliferation and inhibiting apoptosis. *Hepatobiliary Pancreat Dis Int* 2016;15:602-11.
53. He G-L, Feng L, Cai L, et al. Artificial liver support in pigs with acetaminophen-induced acute liver failure. *World J Gastroenterol* 2017;23:3262.
54. Saxena R. Practical hepatic pathology:

- A diagnostic approach. Elsevier/Saunde", Philadelphia 2011.
55. Hamid M, Abdulrahim Y, Liu Q, et al. The hepatoprotective effect of selenium-enriched yeast and gum Arabic combination on carbon tetrachloride-induced chronic liver injury in rats. *J. Food Sci* 2018;83:525-34.
 56. Ma L, Yang X, Wei R, et al. MicroRNA-214 promotes hepatic stellate cell activation and liver fibrosis by suppressing Sufu expression. *Cen Death Dis* 2018;9:1-B.
 57. Alam MF, Safhi MM, Arrwe T, et al. Therapeutic potential of Vanillin acetone against CCl₄ induced hepatotoxicity by suppressing the serum marker, oxidative stress, inflammatory cytokines and apoptosis in Swiss albino mice. *Exp Mol Pathol* 2018;105:81-8.
 58. Song YC, Liu YC, Chao PH, et al. Combined delivery of sorafenib and a MEK inhibitor using CXC targeted nanoparticles reduces hepatic fibrosis and prevents tumor development. *Theranostics* 2018;8:894-905.
 59. Czechowski G, Zielinski K, Korolczuk A, et al. Protective effects of melatonin against thioacetamide-induced liver fibrosis in rats. *J Physiol Pharmacol* 2015;66:567-79.
 60. Mazagova M, Wang L, Anfora AT, et al. Commensal microbiota is hepatoprotective and prevents liver fibrosis in mice. *FASEB J* 2015;29:10H-55.
 61. Chandel R, Saxena R, Das A, et al. Association of miR-183-182 cluster with diethylnitrosamine induced liver fibrosis in Wistar rats. *J Cell Biochem* 2018;119:4072-84.
 62. Jilkova ZM, Kuyucu AI, Kurma K, et al. Combination of AKT inhibitor ARQ 092 and sorafenib potentiates inhibition of tumor progression in cirrhotic rat model of hepatocellular carcinoma. *Oncotarget* 2018;9:1145-55.
 63. Marrone AK, Shipway S, Chappell G, et al. Differentially expressed microRNAs provide mechanistic insight into fibrosis-associated liver carcinogenesis in mice. *Mol Carcinog* 2016;55:808-17.
 64. King PO, Perry MC. Hepatotoxicity of chemotherapy. *Oncologist* 2001;6:162-76.
 65. Nakamura K, Iatano E, Narita M, et al. Sorafenib attenuates monoxrotalene-induced sinusoidal obstruction syndrome in rats through suppression of JNK and MMP-9. *He patol* 2012;57:1037-43.
 66. Robinson SM, Mann DA, Manas DM, et al. The potential contribution of tumour-related factors to the development of FOLFOLX-induced sinusoidal obstruction syndrome. *Br J Cancer* 2013;109:2396-403.
 67. Bruha J, Yycital O, Tonar Z, et al. Monoclonal antibody against transforming growth factor beta 1 does not influence liver regeneration after resection. *Large Animal Experiments* 2015;340:327-40.
 68. Chen X, Ying X, Sun W, et al. The therapeutic effect of fraxetin on ethanol-induced hepatic fibrosis by enhancing ethanol metabolism, inhibiting oxidative stress and modulating inflammatory mediators in rats. *Int Immunopharmacol* 2018;56:931-04.
 69. Choi Y, Abdelmegeed MA, Song BJ. Preventive effects of indole-3-carbinol against alcohol-induced liver injury in mice via antioxidant, anti-inflammatory, and anti-apoptotic mechanisms: Role of gut-liver-adipose tissue axis. *J Nutr Biochem* 2018;55:12-25.

MUDr. Anna Malet'k-Ovd
 ústavh to/ogieaembryologieLFUKvPlzni
 Karlovarskd 48
 JOiOQPtzeň
 anna.mackova@lfpcunia

Příloha V:

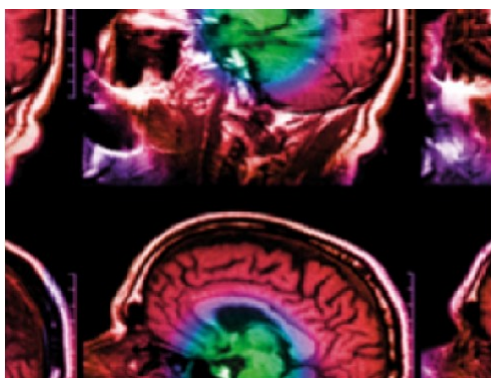
MALEČKOVÁ, Anna, Petra KOCHOVA, Richard PÁLEK, Václav LIŠKA, Patrik **MIK**, Tomasz BONKOWSKI, Miroslav HORÁK a Zbyněk TONAR, 2021. Blunt injury of liver – mechanical response of porcine liver in experimental impact test. *Physiological Measurement* [online]. [vid. 2021-02-24]. ISSN 0967-3334. Dostupné z: doi:10.1088/1361-6579/abdf3c. **IF₂₀₂₀=2,833, Q2**(Biomedical, Engineering).

PAPER

Blunt injury of liver: mechanical response of porcine liver in experimental impact test

To cite this article: Anna Maleková *et al* 2021 *Physiol. Meas.* **42** 025008

View the [article online](#) for updates and enhancements.



IPEM | IOP

Series in Physics and Engineering in Medicine and Biology

Your publishing choice in medical physics,
biomedical engineering and related subjects.

Start exploring the collection—download the
first chapter of every title for free.



CORRIGENDUM

Corrigendum: Blunt injury of liver: mechanical response of porcine liver in experimental impact test (2021 *Physiol. Meas.* 42 025008)

RECEIVED
10 April 2021ACCEPTED FOR PUBLICATION
15 April 2021PUBLISHED
17 June 2021

Anna Malečková^{1,2}, Petra Kochová³, Richard Pálek^{2,4}, Václav Liška^{2,4}, Patrik Mik⁵, Tomasz Bońkowski⁶, Miroslav Horák⁷ and Zbyněk Tonar³

¹ Department of Histology and Embryology, Faculty of Medicine in Pilsen, Charles University, Pilsen, Czech Republic

² Biomedical Center, Faculty of Medicine in Pilsen, Charles University, Pilsen, Czech Republic

³ European Centre of Excellence NTIS, Faculty of Applied Sciences, University of West Bohemia, Pilsen, Czech Republic

⁴ Department of Surgery, Faculty of Medicine and University Hospital in Pilsen, Charles University, Pilsen, Czech Republic

⁵ Department of Anatomy, Faculty of Medicine in Pilsen, Charles University, Pilsen, Czech Republic

⁶ New Technologies—Research Centre, University of West Bohemia, Pilsen, Czech Republic

⁷ Department of Mechanics, Faculty of Applied Sciences, University of West Bohemia, Pilsen, Czech Republic

This corrigendum corrects the wrong description of hepatic lobes in ‘Blunt injury of liver—mechanical response of porcine liver in experimental impact test’ (Malečková *et al* 2021). Right hepatic lobes were wrongly described as left hepatic lobes and vice versa, namely the right lateral lobe was wrongly described as the left lateral lobe; the

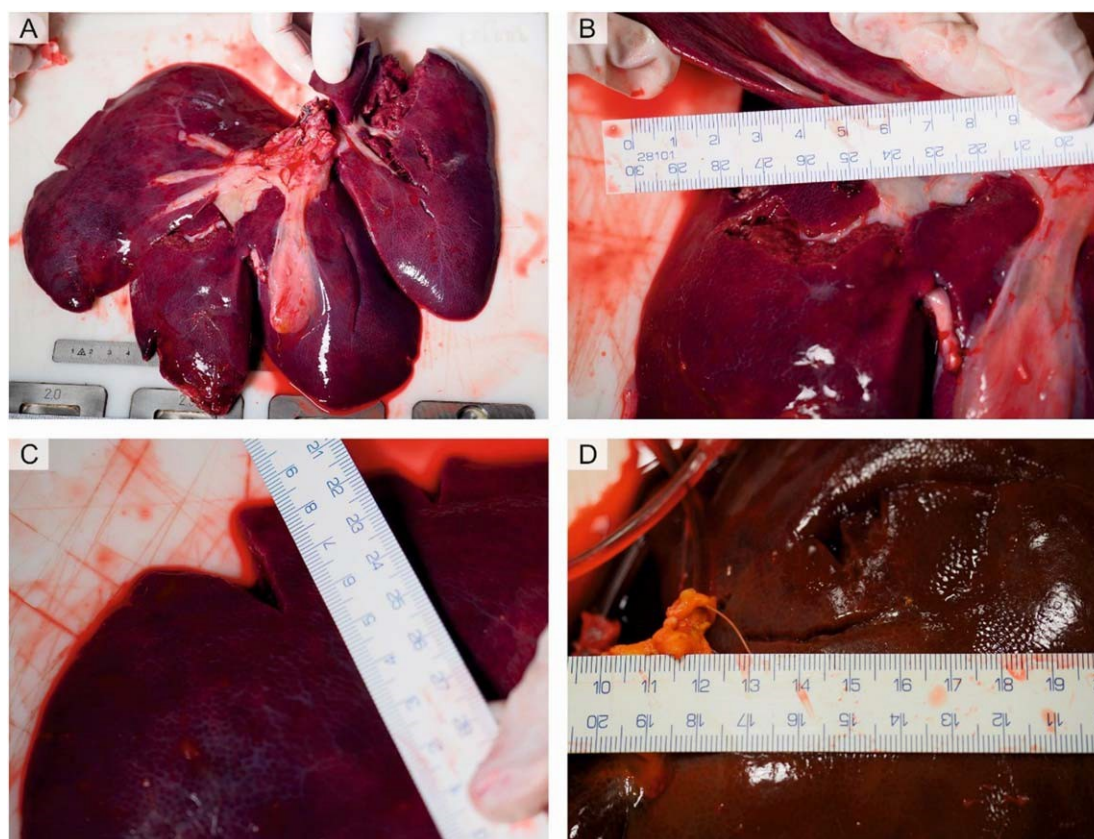


Figure 4. Typical external injury patterns of the porcine liver after the impact test. (A) Laceration of the visceral surface of the liver affecting more than a half of the right lateral lobe, injury grade V. (B) Rupture of the visceral surface of the left medial lobe, that propagates from the hilum along the big vessels and the stromal connective tissue. (C) Peripheral rupture starting at the border of the left lateral lobe. (D) Occasional shallow rupture on the diaphragmatic surface of the liver, most likely caused by the direct impact of the wood plate used in the impact test.

left medial lobe was wrongly described as the right medial lobe. Therefore, the figure caption in figure 4 should be as follows:

Additionally, this error also occurred in Results. The formulation in the section 3.3.1 'Ruptures propagated from the hilum along big vessels and were mostly located in the left lateral (figure 4(A)) and right medial lobes (figure 4(B))' should be changed to 'Ruptures propagated from the hilum along big vessels and were mostly located in the right lateral (figure 4(A)) and left medial lobes (figure 4(B))'.

ORCID iDs

Anna Malečková  <https://orcid.org/0000-0003-2674-6268>

Reference

Malečková A, Kochová P, Pálek R, Liška V, Mik P, Bořkowskí T, Horák M and Tonar Z 2021 Blunt injury of liver—mechanical response of porcine liver in experimental impact test *Physiol. Meas.* **42** 025008



PAPER

Blunt injury of liver: mechanical response of porcine liver in experimental impact test

RECEIVED

15 September 2020

REVISED

13 January 2021

ACCEPTED FOR PUBLICATION

22 January 2021

PUBLISHED

9 March 2021

Anna Malečková^{1,2}, Petra Kochová^{3,*}, Richard Pálek^{2,4}, Václav Liška^{2,4}, Patrik Mik⁵, Tomasz Bońkowski⁶, Miroslav Horák⁷ and Zbyněk Tonar³

¹ Department of Histology and Embryology, Faculty of Medicine in Pilsen, Charles University, Pilsen, Czech Republic

² Biomedical Center, Faculty of Medicine in Pilsen, Charles University, Pilsen, Czech Republic

³ European Centre of Excellence NTIS, Faculty of Applied Sciences, University of West Bohemia, Pilsen, Czech Republic

⁴ Department of Surgery, Faculty of Medicine and University Hospital in Pilsen, Charles University, Pilsen, Czech Republic

⁵ Department of Anatomy, Faculty of Medicine in Pilsen, Charles University, Pilsen, Czech Republic

⁶ New Technologies—Research Centre, University of West Bohemia, Pilsen, Czech Republic

⁷ Department of Mechanics, Faculty of Applied Sciences, University of West Bohemia, Pilsen, Czech Republic

* Author to whom any correspondence should be addressed.

E-mail: Anna.Maleckova@lfp.cuni.cz, kochovap@ntc.zcu.cz, palekr@fnplzen.cz, liskav@fnplzen.cz, Patrik.Mik@lfp.cuni.cz, tomasz@ntc.zcu.cz, horak21@kme.zcu.cz and tonar@ntis.zcu.cz

Keywords: porcine liver, mechanical behavior, liver microstructure, reticular fibers, stereology

Supplementary material for this article is available [online](#)

Abstract

Objective. The liver is frequently injured in blunt abdominal trauma caused by road traffic accidents. The testing of safety performance of vehicles, e.g. belt usage, head support, seat shape, or air bag shape, material, pressure and reaction, could lead to reduction of the injury seriousness. Current trends in safety testing include development of accurate computational human body models (HBMs) based on the anatomical, morphological, and mechanical behavior of tissues under high strain. **Approach.** The aim of this study was to describe the internal pressure changes within porcine liver, the severity of liver injury and the relation between the porcine liver microstructure and rupture propagation in an experimental impact test. Porcine liver specimens ($n = 24$) were uniformly compressed using a drop tower technique and four impact heights (200, 300, 400 and 500 mm; corresponding velocities: 1.72, 2.17, 2.54 and 2.88 m s⁻¹). The changes in intravascular pressure were measured via catheters placed in portal vein and caudate vena cava. The induced injuries were analyzed on the macroscopic level according to AAST grade and AIS severity. Rupture propagation with respect to liver microstructure was analyzed using stereological methods. **Main results.** Macroscopic ruptures affected mostly the interface between connective tissue surrounding big vessels and liver parenchyma. Histological analysis revealed that the ruptures avoided reticular fibers and interlobular septa made of connective tissue on the microscopic level. **Significance.** The present findings can be used for evaluation of HBMs of liver behavior in impact situations.

1. Introduction

Road traffic accidents (RTAs) are one of the main causes of blunt abdominal trauma, which is often accompanied by internal organ injuries, most frequently to the spleen, the liver and the kidney (Elhagediab and Rouhana 1998, Augenstein *et al* 1999, Monchal *et al* 2018). Although soft tissue injuries and bone fractures are the most common types of road traffic injuries, liver trauma is responsible for significant morbidity and mortality (Doklestić *et al* 2015, Vyčítal *et al* 2019). According to the Global Status Report On Road Safety issued by the World Health Organization (2018), vehicle safety is one of the key factors reducing the likelihood of serious injury in RTAs. The importance of both air bag deployment and safety belt restraint in preventing the liver injuries was demonstrated by Holbrook *et al* (2007) in a study that analyzed 311 patients with injuries

suffered in motor vehicle crashes. Therefore, improving safety systems for car occupants became an important tool for the reduction of traffic accident injuries and casualties (Xu *et al* 2018).

Testing the safety performance of newly developed vehicles is usually carried out in two distinct ways: (i) standardized car crash tests using anthropometric testing devices (ATDs) commonly called dummies or (ii) car crash simulations using computational models of ATDs or human body models (HBMs) (Xu *et al* 2018). The current trend in predicting trauma impact on human tissues and organs relies on the development of computational modeling, as only a few large corporations use mechanical dummies for car crash tests (Xu *et al* 2018) and the ATD outputs are only injury criteria based on physically measurable parameters (acceleration, force, compression of chest). The models are based on morphometric data collected from human cadavers (Tropiano *et al* 2004) or imaging modalities such as CT and MRI (Gayzik *et al* 2011), and could be morphed for the wide variety of anthropometries.

The HBMs used for abdominal injury prediction include e.g. the HUMAN Model of Safety, HUMOS (Behr *et al* 2003, Arnoux *et al* 2008), Total Human Model for Safety, THUMS (Golman *et al* 2014), Global Human Body Models Consortium, GHBM (Schoell *et al* 2015, Schwartz *et al* 2015), Wayne State Human Body Models, WSUHAM (Lee and Yang 2001). Arnoux *et al* (2008) used in their experiment a hybrid approach coupling numerical simulation (HUMOS) with experimental data from free fall tests using human cadaver trunks. They provided a complex analysis of the liver behavior within the abdomen in frontal crash situations and proved the importance of experimental data for computational modeling of inner organ behavior. The study has been followed by several experimental studies on human (Cheyne *et al* 2009, Conte *et al* 2012, Untaroiu *et al* 2015) and porcine liver (Chen *et al* 2018, Chen *et al* 2019) biomechanical behavior since then. The studies were mostly focused on the effect of sudden deceleration and impact, two phenomena that were identified as the main causes of liver injury (King and Yang 1995, Cheyne *et al* 2009). The results of those tests were influenced by parameters such as velocity, mass, size, surface area of the impactors, compression and duration of the applied force (Untaroiu *et al* 2015). However, only a few studies were focused on the relationship between liver injury and internal pressure changes (Sparks *et al* 2007, 2008). That is despite the extensive vascular supply of the liver and the previously described dependence of the liver injury severity on rapid increase in internal fluid pressure (Sparks *et al* 2007, 2008, Sparks and Dupaix 2008).

Experiments conducted on human cadavers or organs are valuable sources of biomechanical data (Kemper *et al* 2010, Conte *et al* 2012). Many previous experiments and most of the current liver models, however, include the use of animal tissue to simulate human organs (Melvin *et al* 1973, Wang *et al* 1992, Tamura *et al* 2002, Santago *et al* 2009, Marchesseau *et al* 2017). Using animal cadavers and livers is therefore a plausible and more feasible approach to obtaining biomechanical data. Pig is particularly convenient as it is widely used in different fields of biomedicine for its anatomical and physiological similarities with humans (Eberlova *et al* 2016, Malečková *et al* 2019, Eberlova *et al* 2020). Nevertheless, the anatomical and microscopic differences between human and porcine liver need to be taken into consideration when interpreting data from animal experiments (Huelke *et al* 1986, Kruepunga *et al* 2019). The porcine liver microstructure has already been described in detail using well-established stereological methods (Junatas *et al* 2017, Mik *et al* 2018). The microstructure is organized into well-defined roughly hexagonal hepatic lobules demarcated by fibrous interlobular septa containing portal triads. The interlobular connective tissue originates from the fibrous capsule and enters the liver via the hilum along big branches of hepatic vessels—the portal vein and hepatic artery. The hepatocytes are arranged within lobules into trabeculae surrounded by a delicate network of reticular fibers that separates the hepatocytes from hepatic sinusoids (see supplement S1 (available online at stacks.iop.org/PMEA/42/025008/mmedia)).

The aim of our study was to describe the biomechanical behavior of the whole porcine liver in an experimental impact test, with special emphasis on the internal pressure changes depending on the impact energy. The experiment was designed to enable us to study the effect of impact alone with no influence of deceleration. The severity of liver damage on the macroscopic level was evaluated using the American Association for the Surgery of Trauma (AAST) organ injury scaling and Abbreviated Injury Scale (AIS severity), 2018 update (Kozar *et al* 2018). As the mechanical properties of the soft tissue organs depend on their microscopic structure, we wanted to specifically focus on the relationship between rupture propagation and tissue microstructure, namely on the main fibrillary components of the hepatic interstitial connective tissue matrix. Hence, our biomechanical data were accompanied by histological quantitative analysis. Our aim was also to provide complete primary biomechanical data and make them publicly available for biomechanical modeling of liver crash tests.

2. Methods

2.1. Liver sample preparation

Liver samples were obtained from Prestice Black-Pied pigs (Vrtkova 2015) ($n = 24$). The animals received standard care in compliance with the European Convention on Animal Care, and the project no. MSMT-4428/2018-2 was

approved by the Faculty Committee for the Prevention of Cruelty to Animals. The piglets were pre-medicated by intramuscular administration of 10 mg kg⁻¹ ketamine (Narkamon; Spofa, A.S., Prague, Czech Republic), 5 mg kg⁻¹ azaperon (Stresnil; Janssen Pharmaceutica NV, Beerse, Belgium) and 1 mg atropine (Atropin Biotika; Hoechst Biotika, Martin, Slovak Republic). For general anaesthesia propofol (1% mixture 5–10 mg⁻¹ kg⁻¹ h⁻¹ propofol; Fresenius Kabi Norges AS, Halden, Norway) was administered intravenously. Continuous analgesia was provided by fentanyl (1–2 µg⁻¹ kg⁻¹ h⁻¹ Fentanyl Torre; Chiesi CZ s.r.o., Prague, Czech Republic). Airways were secured by endotracheal intubation and pigs were mechanically ventilated. The piglets received infusion and volume substitution when necessary (Hartmann's Solution; B. Braun Melsungen AG, Melsungen, Germany and Plasmalyte; Baxter Healthcare Ltd, Compton, UK).

Midline laparotomy was performed to enter the abdominal cavity. All the ligaments attaching the liver to the surrounding structures were transected, the common bile duct was ligated and divided, and the portal vein, hepatic artery and the infrahepatic part of the caudate vena cava (equivalent to the inferior vena cava in human anatomy) were dissected. The thoracic cavity was opened to gain access to the thoracic part of the caudate vena cava. The diaphragm was transected in the ventrodorsal direction leaving a small rim around the caudate vena cava. The animal was then heparinized (10 000 IU of heparin; Zentiva, k.s., Prague, Czech Republic) and the portal vein and the thoracic part of the caudate vena cava were cannulated by infusion tubes. These tubes were later used for measuring intravascular pressure in the liver. Finally, all the vessels supplying and draining the liver were ligated and divided and the whole organ, filled with blood, was removed from the body. The animals were sacrificed under general anesthesia via an intravenous administration of a cardioplegic solution (potassium chloride).

2.2. Impact

test

Prior to the mechanical experiment, all the specimens were checked for the following conditions that might have been caused by specimen handling: contusions, ruptures and bleeding. Damaged specimens were excluded from further analysis. In total, 24 livers were used for the mechanical experiment. The livers were divided into four groups (six livers per group) based on the impact height (200, 300, 400 and 500 mm and corresponding impact velocity 1.72, 2.17, 2.54 and 2.88 m s⁻¹, respectively). The specimens were kept cool on ice until the mechanical impact test. The maximum time between surgery and impact test was three hours. Firstly, each liver was pressurized through the infusion tubes inserted in the portal vein and caudate vena cava at 7 cm H₂O by 0.9% NaCl solution. Maintaining the turgor of the liver at a level comparable to normal hemodynamic pressures was necessary for simulation of impact injuries (Melvin *et al* 1973). Then the size and weight of the pressurized liver was measured. After that, the livers were put into the measurement device—a drop tower (Sparks *et al* 2008). The livers were uniformly compressed using an impact 6.22 kg plate made of wood with impact area of 29.5 cm × 29.5 cm. The plate was firmly connected to an aluminum beam, which could freely move along the aluminum frame. We neglected the beam friction to simulate the plate free fall by the use of Teflon sliders between the beam and the frame. The plate was covered by a plastic foil and spread with tempera color to visualize the contact area between the plate and the liver.

The pressure was recorded at the portal vein and the caudate vena cava during the impact test using a Silicon Pressure Sensor MPXV5100DP (GND +5V) (NXP Semiconductors N.V., Eindhoven, Netherlands). The sensor was connected to the external opening of the infusion tube, while the intravascular opening was placed in the blood vessels, in a way similar to the setting previously proposed by Sparks *et al* (2008).

Maximal pressure values were used for further quantitative analysis. The position of the impact plate before the impact was measured by two lasers optoNCDT 2300-50 (Micro-Epsilon GmbH, Frankfurt am Main, Germany) on each side of the impacting beam. The velocity of the impact was derived from the position measurement and then averaged from both lasers. Measured signals were acquired by the NI CompactDAQ (National Instruments, Austin, TX, USA) system with SignalExpress software (National Instruments, Austin, TX, USA). The system energy was determined by two formulas:

$$E_K = \frac{1}{2}mv^2$$

where m was the weight of the impact plate and v was the velocity of the impact plate before impact, and

$$E_P = mgh$$

where m was the weight of the impact plate, g was acceleration of gravity, and h was the height of the impact given as impact height minus the liver thickness. The loading area was calculated from the colored part of the liver using Ellipse software (ViDiTo, Košice, Slovak Republic). The impact energy was then calculated as the energy of the plate divided by the loaded area. The loaded area in percentage was calculated as the colored part of liver divided by the total liver area. Both parameters were estimated with Ellipse software using the 'POLYGON' tool in calibrated photographs.

2.3. Macroscopic

injury

analysis

Immediately after the impact test, ruptures on the surface of the liver were captured by camera and the projection length of the ruptures was measured. The position of the ruptures with respect to the liver lobes was registered to determine the most frequently damaged part of the liver. After that, each liver was cut completely into 1 cm thick slices and the depth of the ruptures and the depth of the contused parenchyma were measured. The depth was defined as the distance between the liver surface and the deepest point of the damaged parenchyma perpendicular to the liver surface. Both the projection length and the depth of the ruptures were measured in calibrated photographs using the Ellipse software 'LINE' tool (ViDiTo, Kosice, Slovak Republic). The injury grade and AIS severity were then determined according to liver injury scaling (Moore *et al* 1989, Kozar *et al* 2018).

2.4. Microscopic

injury

analysis

For the histological analysis, every fourth tissue slice was selected using systematic uniform random sampling. The first slice was selected randomly using the RANDBETWEEN function in Microsoft Office Excel. The selected slices were trimmed into tissue blocks with dimensions $1 \times 1 \times 1$ cm. Every eighth tissue block was then processed histologically. Each sample was carefully examined for liver abnormalities or signs of liver damage, especially inflammation and liver fibrosis. For the quantitative analysis of the ruptures we selected tissue samples with a macroscopically visible crack, 27 tissue blocks in total. The tissue samples were fixed in 4% buffered formalin, dehydrated and embedded in paraffin blocks. Each selected tissue block was cut into 5 μ m thick sections. The section plane was perpendicular to the liver capsule. Sections were stained with hematoxylin-eosin (HE) and with Reticulin kit (BioGnost Ltd, Zagreb, Croatia) in order to visualize reticular fibers (type III collagen). Reticular fibers are located within the interlobular septa. They also represent the essential part of a delicate network, that separates the hepatic sinusoids and hepatocytes within the hepatic lobules (supplement S1). The results were based on 189 sections.

To determine the spatial relationship of ruptures and reticular fibers, we used a method previously published by Tonar *et al* (2009) and Kubíková *et al* (2017). Briefly, an isotropic stereological grid with known geometrical parameters was superimposed over the microphotographs. The number of intersections between this grid and reticular fibers was then counted. We compared the estimated value of the intersection intensity of reticular fibers along the rupture $P'_{L(\text{ret.})}$ with the theoretical value $P_{L(\text{ret.})}$ that should be expected in the case of random propagation of the microcracks throughout the liver parenchyma. The values were calculated with the assumption of independence of the ruptures on the reticular fibers.

The theoretical intersection intensity $P_{L(\text{ret.})}$ was calculated as the intersection intensity of a randomly oriented line (i.e. the rupture) with the reticular fibers (Stoyan *et al* 1995). It was defined as follows:

$$P_{L(\text{ret.})} = \frac{2}{p} L_{A(\text{ret.})}$$

where $L_{A(\text{ret.})}$ was the 2D length density of reticular fibers within liver. For each analyzed sample the length density L_A was assessed individually as follows:

$$L_A = \frac{L}{A}$$

where L is the length of the reticular fibers and A is the area of the reference space. L was estimated by counting the intersections of circular arcs randomly positioned on the microphotographs with reticular fibers. A was estimated using the point grid.

The intersection intensity of reticular fibers $P'_{L(\text{ret.})}$ was defined as follows:

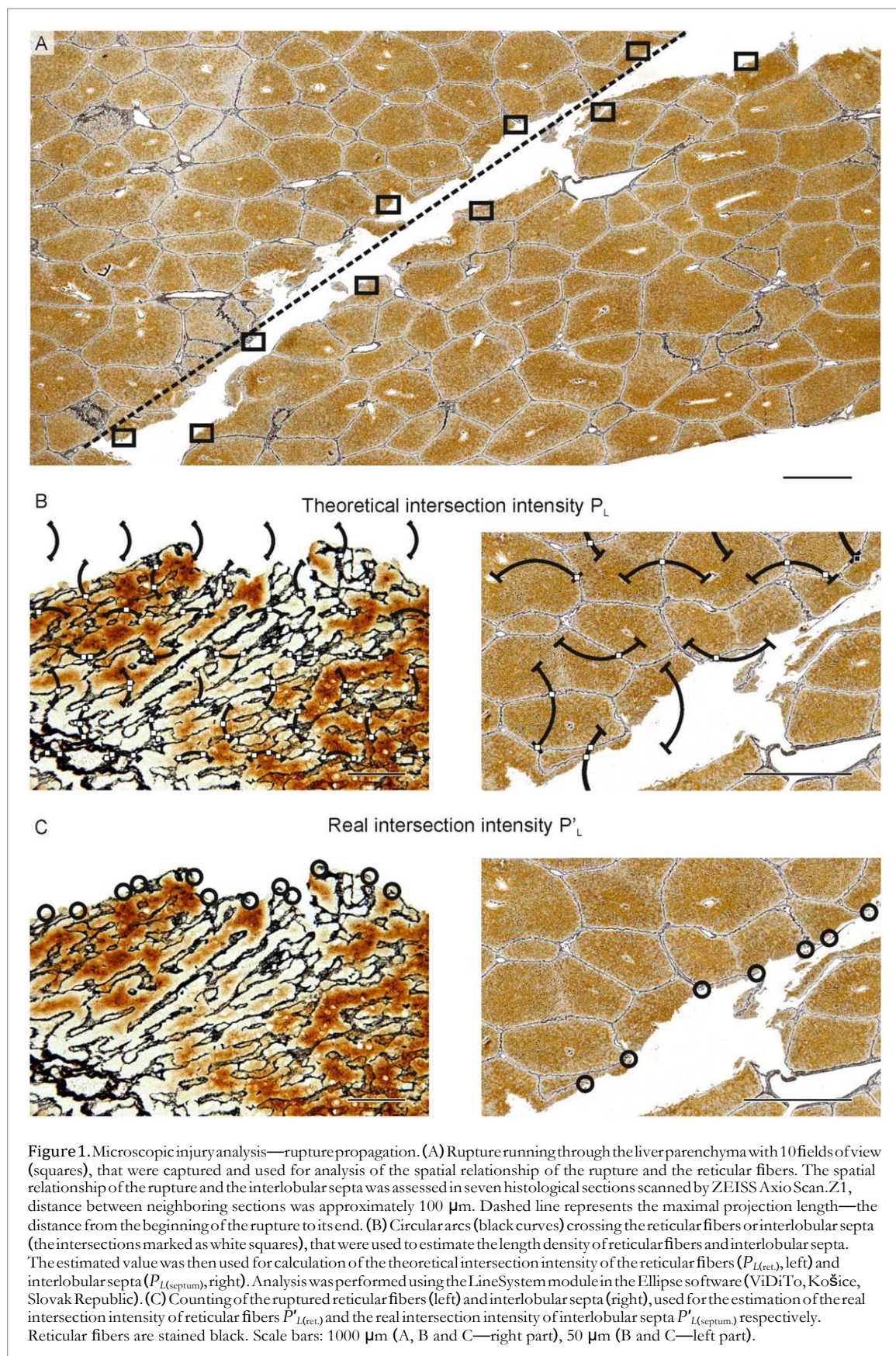
$$P'_{L(\text{ret.})} = \frac{p(\text{ret.})}{l(\text{ret.})}$$

where $p(\text{ret.})$ is the real number of the intersections counted in the histological sections along the rupture of the length l . The length $l(\text{ret.})$ was defined as the shortest distance between the beginning and the end of the crack, the so-called maximal projection length. To estimate all the parameters, we used Ellipse software (ViDiTo, Košice, Slovak Republic) (figure 1).

The same analysis was performed to determine the spatial relationship of ruptures and the interlobular septa. We compared the estimated value of the intersection intensity of interlobular septa along the rupture $P'_{L(\text{septum})}$ with its theoretical value $P_{L(\text{septum})}$.

If the actual propagation of the ruptures throughout the liver parenchyma were at random, there would be no significant difference between the real intersection intensity and the theoretical intersection intensity ($P'_L = P_L$). Therefore, a significant difference between the theoretical value of intersection intensity P_L and the observed intersection intensity P'_L would indicate that the rupture ran predominantly across the reticular fibers

or interlobular septa ($P'_L > P_L$) or along the reticular fibers or interlobular septa ($P'_L < P_L$).



2.5. Statistical

analysis

The data were processed using Statistica Base 10 (StatSoft, Inc., Tulsa, OK, USA). The normality of the data was tested using the Shapiro–Wilk W -test. All the statistical tests were non-parametric methods, because some datasets did not pass the normality test. To assess the differences among the impact groups, we used the Kruskal–Wallis

Table 1. Morphometric data on pigs and livers.

Impact height (mm)/ impact velocity (m s ⁻¹)	Sex	Age (weeks)	Pig weight (kg)	Liver weight (kg)	Liver width (mm)	Liver height (mm)	Liver depth (mm)
200/1.74	Female	14	30	1.570	300	216	33
200/1.70	Female	16	25	1.328	278	208	50
200/1.72	Female	16	35	1.636	299	224	47
200/1.74	Male	14	27	1.472	274	241	35
200/1.70	Male	14	24	1.192	267	222	40
200/1.71	Male	14	24.5	1.232	296	216	38
300/2.15	Male	17	28.5	1.336	264	219	47
300/2.16	Male	15	27.2	1.278	298	285	45
300/2.20	Female	15	29.6	1.348	288	240	33
300/2.17	Male	15	36	1.394	280	250	45
300/2.20	Male	16	34.2	1.112	283	208	33
300/2.14	Female	16	37.8	1.400	283	220	37
400/2.52	Female	17	42.8	1.446	273	224	43
400/2.56	Male	15	28.5	1.054	247	226	41
400/2.50	Male	16	33	1.252	257	232	39
400/2.62	Male	16	37	1.650	315	245	40
400/2.51	Male	16	41.5	2.044	287	265	55
400/2.50	Female	16	39.4	1.492	265	275	38
500/2.89	Male	15	36.5	1.030	240	194	37
500/2.92	Male	15	28	1.070	256	184	35
500/2.85	Male	15	25.5	1.108	246	198	40
500/2.84	Male	15	25	1.060	244	191	43
500/2.95	Male	16	37.7	1.572	307	248	40
500/2.86	Male	16	35	1.700	283	235	55

ANOVA test. To compare the paired values of real intersection intensity (P'_L) and theoretical intersection intensity (P_L), we used the Wilcoxon signed-rank test. The level of significance was 0.05.

3. Results

3.1. Liver samples

The livers were collected from 24 Prestige Black-Pied pigs aged 14–17 weeks and weighing 24–42.8 kg (31.9 ± 5.6 kg, mean \pm standard deviation [SD]). Seventeen piglets were neutered male and seven female. The fresh liver weight ranged from 1.030 to 2.044 kg (1.364 ± 0.24 kg, mean \pm standard deviation [SD]) (table 1). None of the specimens had signs of microscopic injury such as inflammatory infiltration or fibrosis.

3.2. Impact test

3.2.1. Greater impact velocity (heights) resulted in increased maximal intravascular pressure accompanied by more severe injury.

The impact plate hit less than a half or about a half of the liver in all cases, figure 2(A). There was an increasing trend of maximal pressure related to the impact velocity, but it did not reach the level of significance, figure 2(B). The impact energies (given by liver height and by plate position measured by laser, figure 2(C)) increased with impact velocity. The higher impact velocity led to more severe injury, figure 2(D, E). The linear regression analysis of the AIS severity and injury grade is shown in figure 2(F). These two parameters are interchangeable. The regression analysis of AIS severity and maximal pressure, and impact energy is shown in figure 3(A), and 3(B), respectively. The results are summarized in table 2 and shown in figure 2. Complete primary biomechanical data are available as supplement S2.

3.3. Macroscopic injury analysis

3.3.1. Ruptures affected mostly the interface between connective tissue surrounding big vessels and liver parenchyma

The major injuries affected the visceral surface of the liver as shown in figure 4. Ruptures propagated from the hilum along big vessels and were mostly located in the left lateral (figure 4(A)) and right medial lobes (figure 4(B)). The depth of the lacerations and contused parenchyma differed among experimental groups as well as among livers within the groups. The injury grade was based both on the length and on the depth of the ruptures. Most severe injuries were found in the group with impact velocity 2.88 m s⁻¹ (impact height 500 mm)

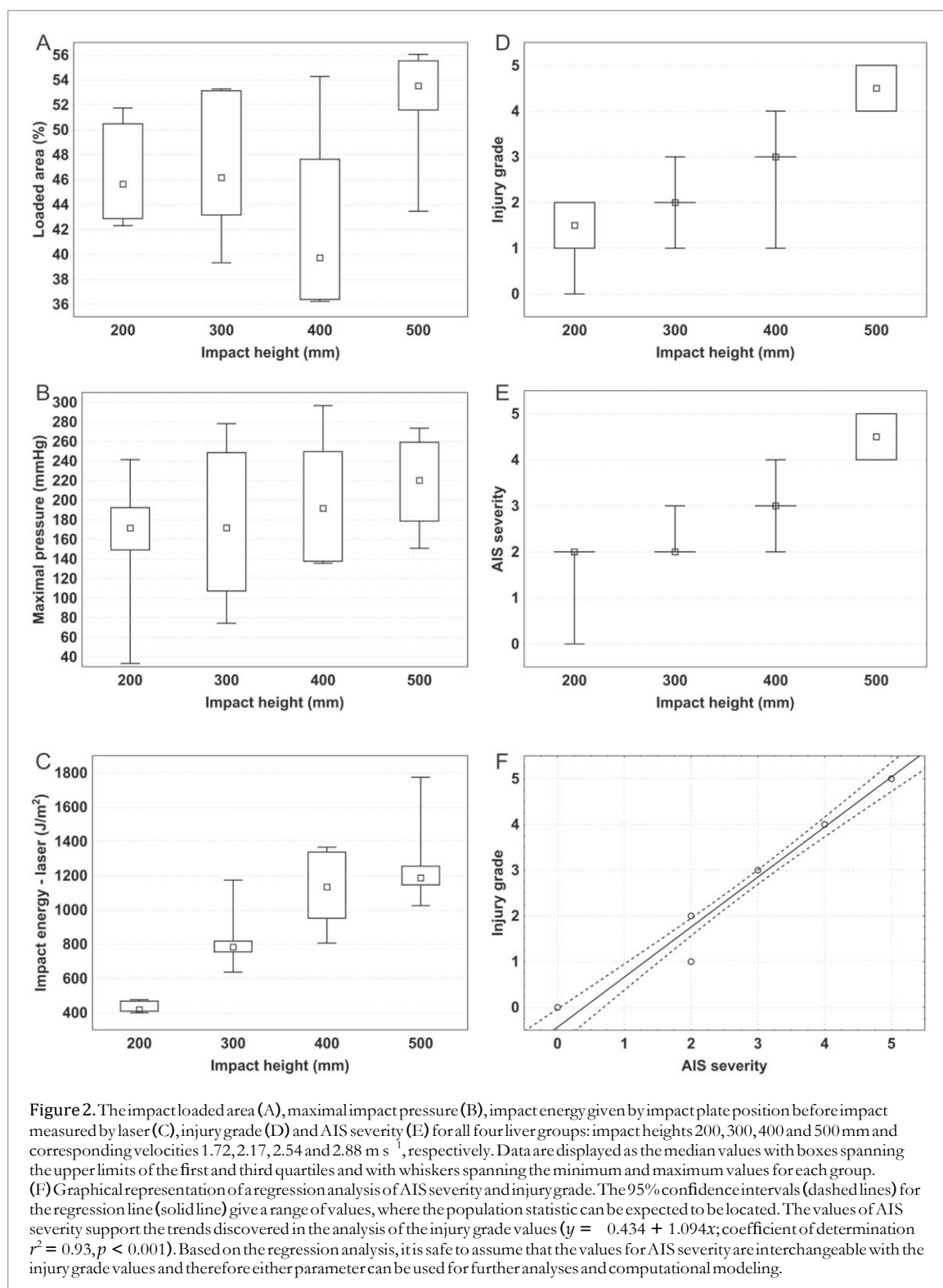


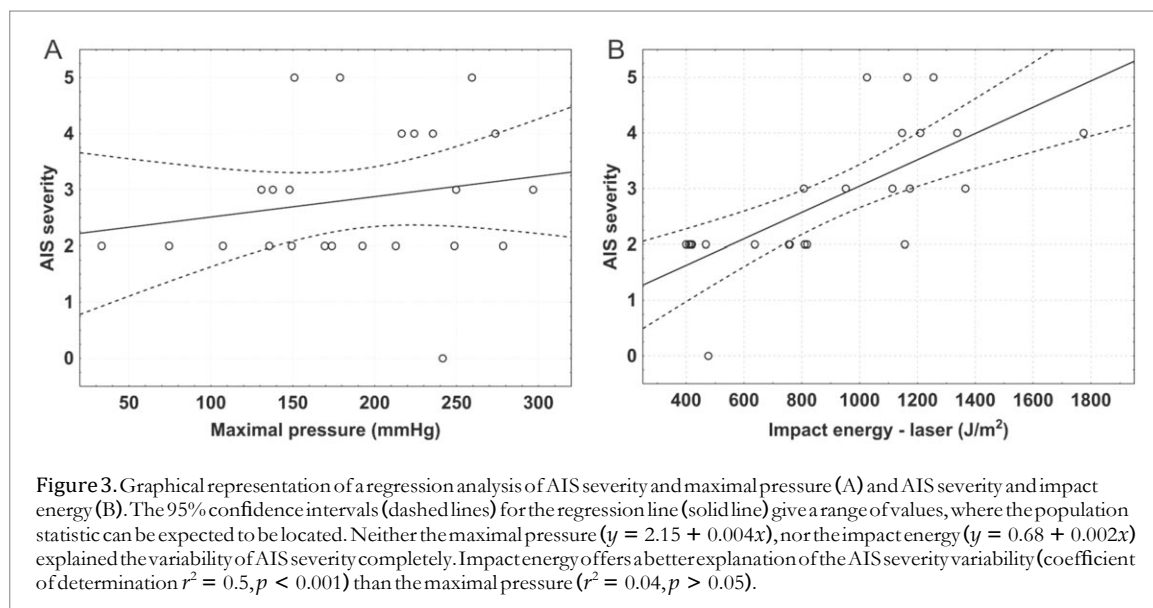
Figure 2. The impact loaded area (A), maximal impact pressure (B), impact energy given by impact plate position before impact measured by laser (C), injury grade (D) and AIS severity (E) for all four liver groups: impact heights 200, 300, 400 and 500 mm and corresponding velocities 1.72, 2.17, 2.54 and 2.88 m s^{-1} , respectively. Data are displayed as the median values with boxes spanning the upper limits of the first and third quartiles and with whiskers spanning the minimum and maximum values for each group. (F) Graphical representation of a regression analysis of AIS severity and injury grade. The 95% confidence intervals (dashed lines) for the regression line (solid line) give a range of values, where the population statistic can be expected to be located. The values of AIS severity support the trends discovered in the analysis of the injury grade values ($y = 0.434 + 1.094x$; coefficient of determination $r^2 = 0.93$, $p < 0.001$). Based on the regression analysis, it is safe to assume that the values for AIS severity are interchangeable with the injury grade values and therefore either parameter can be used for further analyses and computational modeling.

(table 2). In some cases, the ruptures were located on the periphery of the lobe (figure 4(C)) and, occasionally, we found small lacerations on the diaphragmatic surface of the liver (figure 4(D)).

3.4. Microscopic injury analysis

3.4.1. The ruptures avoided reticular fibers and interlobular septa on the microscopic level

The real intersection intensity P^l_L was smaller than the theoretical intersection intensity P_L for both the reticular fibers and for the interlobular septa (Wilcoxon signed-rank test, $p < 0.001$) (figure 5). The ruptures thus did not



propagate randomly through the liver parenchyma but predominantly ran along the reticular fibers and interlobular septa avoiding intersections with reticular fibers and interlobular septa.

4. Discussion

This study on porcine liver injury focused on description of the tissue damage and the biomechanical behavior of liver tissue. We combined an impact approach using a drop tower technique, while registering the changes of intravascular pressure in portal vein and caudate vena cava. Our mechanical data focused on the internal fluid pressure changes in impact situations. Even though the liver tissue damage in car crashes is the consequence of both deceleration and impact (Cheynel *et al* 2009), the sole impact approach allowed us to exclude the influence of the deceleration on the biomechanical behavior and to study the effect of impact alone. A similar approach, albeit, by simulating the deceleration injury alone has already been used in studies by Cheynel *et al* (2006, 2009) and by Arnoux *et al* (2008). Such experiments provide data that can be used for validation of the computational models of liver injury.

The finite element method (FEM)-based models of liver are mostly based on the detailed geometry of the real liver. Our study showed that the ruptures were spreading around the vascular branches, thus the vascular tree should be included in the FEM models because of its important contribution to the injury mechanism.

Another factor that should be taken into account in the models is the increased inner liver pressure caused by impact loading. High pressure levels can cause ruptures adjacent to the vascular trees. These ruptures propagate along the reticular fibers and interlobular connective tissue septa as shown in our study.

Our results are further suitable for validation of impact test results in terms of the impact energy and velocity threshold. The impact velocities and the impact energies used in the impact tests in our study should lead to the same injury levels also when used in the simulated impact tests with HBMs. An impact velocity of 1.72 m s^{-1} with impact energy 418 J m^{-2} leads to low injury grade (0–II) and AIS severity (0–2), while the higher impact velocity (energy) caused the injury connected with large blood outflow. An impact velocity higher than 2.88 m s^{-1} , related to an impact energy higher than 1187 J m^{-2} , leads to total disruption of the liver. Also the internal liver pressure in the HBMs should be the same as during our impact test. Note that the high levels of pressure could also lead to the artery or internal structures ruptures.

A recent study by Chen *et al* (2019) provided detailed data on material behavior of porcine liver during high strain rate compression. However, their measurements were performed on tissue samples separated from the whole liver, thus excluding the effect of the fibrous capsule on the biomechanical behavior. It was proven that the content of connective tissue influenced the stiffness of the liver tissue (Mazza *et al* 2007). Neglecting the influence of the capsule could result in significant differences when assessing the biomechanical behavior of the liver parenchyma (Hollenstein *et al* 2006). The test on tissue samples provided us only with information on local material properties. Moreover, the proposed study design using samples of liver tissue cannot be used for studying the relation of internal fluid pressure changes on the impact injury. As previously described, rapid increase in internal fluid pressure is related to the severity of liver injury on the whole organ level (Spark *et al* 2008). Therefore

Table 2. The impact loaded area, maximal impact pressure, impact velocity, impact energy (given by position of the plate before the impact) measured by laser and given by liver height respectively, AAST injury grade and AIS severity for all four liver groups: impact height 200, 300, 400 and 500 mm. *N* is the number of specimens. The values of impact velocity are presented as mean values. The values of loaded area, maximal vascular pressure and impact energy are presented as medians (lower quartile–upper quartile).

Impact height (mm)	Impact velocity (m s ⁻¹)	Loaded area (%)	Maximal vascular pressure (mmHg)	Impact energy—laser (J m ⁻²)	Impact energy—height (J m ⁻²)	AAST injury grade/AIS severity	<i>N</i>
200	1.72	45.65 (42.88–50.48)	171.69 (149.35–192.52)	418.00 (409.55–467.87)	450.00 (446.57–485.07)	0–II/0–2	6
300	2.17	46.17 (43.17–53.14)	174.85 (107.34–248.69)	783.97 (755.30–818.35)	850.31 (813.06–876.81)	I–III/2–3	6
400	2.54	39.73 (36.40–47.64)	191.77 (137.85–249.69)	1134.79 (952.00–1337.62)	1239.53 (976.22–1435.52)	I–IV/2–4	6
500	2.88	53.53 (51.89–55.54)	220.35 (178.85–259.36)	1187.47 (1146.72–1255.55)	1305.18 (1224.52–1347.71)	IV–V/4–5	6

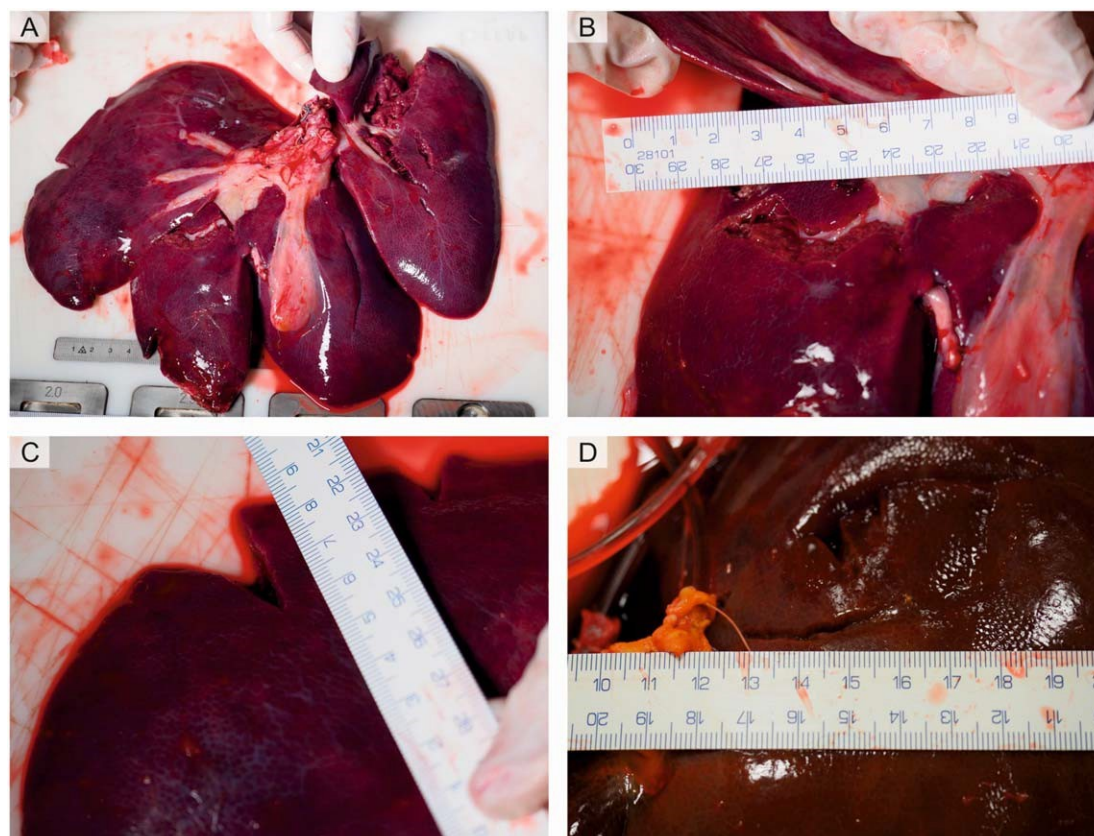


Figure 4. Typical external injury patterns of the porcine liver after the impact test. (A) Laceration of the visceral surface of the liver affecting more than half of the left lateral lobe, injury grade V. (B) Rupture of the visceral surface of the right medial lobe that propagates from the hilum along the big vessels and the stromal connective tissue. (C) Peripheral rupture starting at the border of the right hepatic lobe. (D) Occasional shallow rupture on the diaphragmatic surface of the liver, most likely caused by the direct impact of the wood plate used in the impact test.

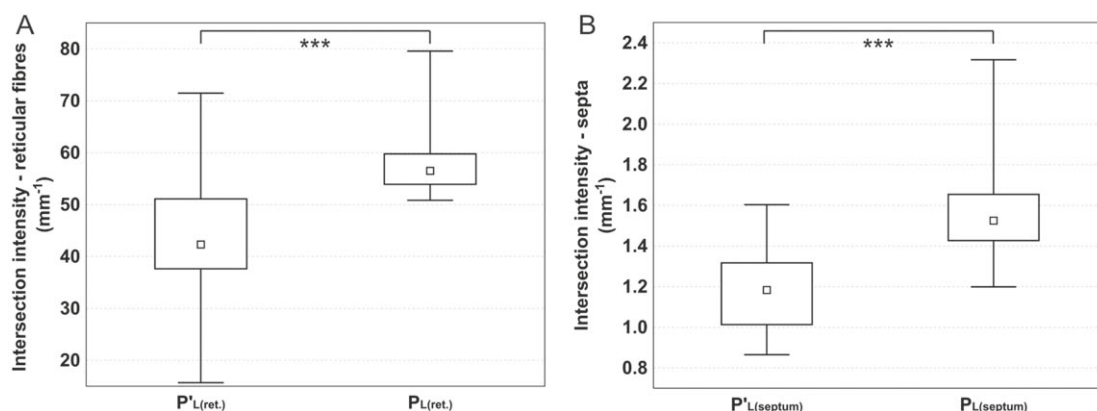


Figure 5. Results of microscopic injury analysis. The Wilcoxon signed-rank test showed statistically significant differences between the real intersection intensity of the reticular fibers $P'L_{(ret.)} = 42$ (38–51) mm^{-1} ; median (lower quartile–upper quartile) and the theoretical intersection intensity of the reticular fibers $PL_{(ret.)} = 57$ (54–60) mm^{-1} ; median (lower quartile–upper quartile), ($p < 0.001$). Significant differences were also found between the real intersection intensity of the interlobular septa ($P'L_{(septum)} = 1.2$ (1–1.3) mm^{-1} ; median (lower quartile–upper quartile) and the theoretical intersection intensity of the interlobular septa $PL_{(septum)} = 1.5$ (1.4–1.7) mm^{-1} ; median (lower quartile–upper quartile), ($p < 0.001$). Data are displayed as the median values with boxes spanning the upper limits of the first and third quartiles and with whiskers spanning the minimum and maximum values for each group.

experiments on whole porcine liver are a necessary source of data on liver behavior from the pressure changes point of view.

The whole liver was also used in experiments with human organs. Conte *et al* (2012) investigated macroscopic damage of human liver in a uniaxial compression test. The macroscopic injury consisted mostly of

lacerations of the right lobe. In some cases the lacerations originated in close proximity to the big vessels and propagated along the connective tissue, which was in concordance with the macroscopic injury pattern in our study. Occasional lacerations of the liver diaphragmatic surface found in our study were mostly caused by the setting of the experiment. The diaphragmatic surface was exposed to the direct impact of the wooden plate, which did not correspond to the injury mechanism *in vivo*.

The multiscale analysis by Conte *et al* (2012) also included histological analysis of the damaged tissue. The microscopic injury patterns presented in human liver tissue were described as ‘cracking’ and ‘cavitation’ that appeared to propagate within the hepatic lobules. According to this analysis the cracks’ origin appeared to be located at the interface between the vessel wall and the parenchyma. Their data, however, did not clearly answer how the tissue damage spread in the context of liver microstructure, namely in the context of the fibrous components of the connective tissue matrix.

Our histological quantitative analysis based on stereological methods revealed that the ruptures did not propagate randomly through the liver parenchyma, but rather followed a pattern that was closely related to the tissue microstructure. The weak link of the tissue appeared to be the interface between the reticular fibers and the hepatocytes arranged into trabeculae, as ruptures crossing the reticular fibers were statistically proven to be less likely to occur than ruptures propagating along the above-mentioned interface. Moreover, the interlobular septa that are composed of connective tissue also seemed to represent a strong border that ruptures did not cross.

The components of the extracellular connective tissue matrix, such as collagen III in reticular fibers, influence the response of the organ to mechanical stimuli. Collagen is a rather stiff and hard protein whereas cells on the other hand tend to respond to mechanical stimuli in various ways (Meyers *et al* 2008). The cell rigidity is dependent on its environment, including cell–extracellular matrix interactions. The difference in microscopic structures of porcine and human liver therefore needs to be taken into consideration when extrapolating data from experiments on porcine organs to the human model.

Based on our study and works focused on the macro- and micro-structure of liver, there are three main differences between human and porcine liver that are important for the mathematical modeling. The microstructure of porcine liver is organized into only roughly hexagonal hepatic lobules, while the microstructure of human liver is organized into regular hexagonal hepatic lobules. This difference is important for the mathematical models based on the microstructure. The second main difference is the shape of the whole liver (Ntonas *et al* 2020). The shape of porcine liver is lobular and thick in the centre, becoming thinner at the perimeter of the organ, while human liver has a triangular prism shape, and the size decreases from right to left. Both human and porcine livers consist of sinister, dexter, quadrate, and caudate lobes. Because of the more lobular shape of the porcine liver, the sinister and dexter lobes are each divided into lateral and medial lobes. The arterial vascular system in both humans and pigs have the same structure. The portal veins of the species have minor differences. In human, the division of the portal vein occurs outside the liver parenchyma, while in pigs, it occurs at the hilum. The third difference is the amount of connective tissue, which is significantly higher in pigs compared to humans (Mik *et al* 2018). One of the main aims of our study was to find connection between the impact energy and the range of injury. The results are based on the porcine liver, but the level of injury, the rupture around veins and the rupture spreading should be similar for both species due to similarities in the tissue structure (however, this claim is yet to be verified).

Velocity is recognized to be a critical factor in evaluating the possibility of abdominal organ injuries. According to Brasel and Nirula (2005) the probability of abdominal injury significantly increases at velocity $>20 \text{ km h}^{-1}$. However, in our study, relatively low velocities of the impact plates at the moment of impact still led to severe liver injury. This was probably caused by the absence of the protective effect of the rib cage and of the abdominal wall. Despite this limitation, the analysis showed an increasing trend of maximal pressure related to the impact height and impact velocities, which supported the view that the severity of injury was dependent on the impact energy. The highest loaded velocity (impact height) caused the most severe lacerations.

5. Conclusion

Using an experimental impact approach, this study provides a multiscale analysis of the mechanism of porcine liver injury that gives an accurate description of damage evolution which can also be applied to human liver tissue. Biomechanical behavior of porcine tissue, namely changes in intravascular pressure, was coupled with analysis of rupture propagation on both the macroscopic and microscopic level. The microscopic analysis proved that connective tissue containing reticular fibers influenced the rupture propagation through liver. The pattern of rupture propagation, with regards to differences in the amount of connective tissue in porcine and human liver, should be especially considered when extrapolating data from animal experiments to the human model. The present findings can be used to improve (by incorporating the vascular tree) and validate computational models of liver behavior in impact situations.

Acknowledgments

This study was supported by the LO1506 (PK) provided by the Ministry of Education, Youth and Sports of the Czech Republic, by the Charles University Research Fund (Progres Q39) (AM), by Charles University Project number SVV 260 536 (AM) and GAUK 1098120 (AM), by the Centre of Clinical and Experimental Liver Surgery UNCE/MED/006 (AM, RP, VL, PM), by University of West Bohemia Project number SGS-2019-002 'Computer modelling and monitoring of human body used for medicine' (TB) and by European Regional Development Fund-Project, Application of Modern Technologies in Medicine and Industry' (No. CZ.02.1.01/0.0/0.0/17_048/0007280) (PK, RP, VL, PM, ZT).

Authorship

Study design, literature search, data analysis, data interpretation, and writing—AM, PK, ZT, animal care—RP, VL, histology—AM, PM, ZT, biomechanical measurements—PK, TB, MH, critical revision—ZT, VL, PM.

Disclosure

The authors declare no conflicts of interest.

References

- Arnoux P J, Serre T, Cheynel N, Thollon L, Behr M, Baque P and Brunet C 2008 Liver injuries in frontal crash situations a coupled numerical—experimental approach *Comput. Methods Biomech. Biomed. Engin.* **11** 189–203
- Augenstein J, Bowen J, Perdeck E, Singer M, Stratton J, Horton T, Rao A, Digges K H, Malliaris A C and Steps J 1999 Injury patterns in near-side collisions *Annu. Proc. Assoc. Adv. Automot. Med.* **43** 139–58 (PMCID: PMC3400216)
- Behr M, Arnoux P J, Serre T, Bidal S, Kang H S, Thollon L, Cavallero C, Kayvantash K and Brunet C 2003 A human model for road safety: from geometrical acquisition to model validation with radioss *Comput. Methods Biomech. Biomed. Engin.* **6** 263–73
- Brasel K J and Nirula R 2005 What mechanism justifies abdominal evaluation in motor vehicle crashes? *J. Trauma* **59** 1057–61
- Chen J, Brazile B, Prabhu R, Patnaik S S, Bertucci R, Rhee H, Horstemeyer M F, Hong Y, Williams L N and Liao J 2018 Quantitative analysis of tissue damage evolution in porcine liver with interrupted mechanical testing under tension, compression, and shear *J. Biomech. Eng.* **140** 0710101–07101010
- Chen J, Patnaik S S, Prabhu R K, Priddy L B, Bouvard J L, Marin E, Horstemeyer M F, Liao J and Williams L N 2019 Mechanical response of porcine liver tissue under high strain rate compression *Bioengineering (Basel)* **6** 49
- Cheynel N, Serre T, Arnoux P J, Baque P, Benoit L, Berdah S V and Brunet C 2006 Biomechanical study of the human liver during a frontal deceleration *J. Trauma* **61** 855–61
- Cheynel N, Serre T, Arnoux P J, Ortega-Deballon P, Benoit L and Brunet C 2009 Comparison of the biomechanical behavior of the liver during frontal and lateral deceleration *J. Trauma* **67** 40–4
- Conte C, Garcia S, Arnoux P J and Masson C 2012 Experimental multiscale analysis of liver damage and failure process under compression *J. Trauma Acute Care Surg.* **72** 727–32
- Doklešić K et al 2015 Surgical management of AAST grades III–V hepatic trauma by damage control surgery with perihepatic packing and definitive hepatic repair—single centre experience *World J. Emerg. Surg.* **10** 34
- Eberlova L et al 2016 Porcine liver vascular bed in Biodur E20 corrosion casts *Folia Morphol. (Warsz)* **75** 154–61
- Eberlova L, Malečkova A, Mik P, Tonar Z, Jirik M, Mirka H, Palek R, Leupen S and Liska V 2020 Porcine liver anatomy applied to biomedicine *J. Surg. Res.* **250** 70–9
- Elhagediab A and Rouhana S 1998 Patterns of abdominal injury in frontal automotive crashes *The 16 Int. Technical Conf. on the Enhanced Safety of Vehicles*
- Gayzik F S, Moreno D P, Geer C P, Wuertzer S D, Martin R S and Stitzel J D 2011 Development of a full body CAD dataset for computational modeling: a multi-modality approach *Ann. Biomed. Eng.* **39** 2568–83
- Golman A J, Danelson K A, Miller L E and Stitzel J D 2014 Injury prediction in a side impact crash using human body model simulation *Accid. Anal. Prev.* **3** 1–8
- Holbrook T L, Hoyt D B, Eastman A B, Sise M J, Kennedy F, Velky T, Conroy C, Pacyna S and Erwin S 2007 The impact of safety belt use on liver injuries in motor vehicle crashes: the importance of motor vehicle safety systems *J. Trauma* **63** 300–6
- Hollenstein M, Nava A, Valtorta D, Snedeker J G and Mazza E 2006 Mechanical characterization of the liver capsule and parenchyma *ISBMS 2006: Biomedical Simulation (Lecture Notes in Computer Science vol 4072)* ed M Harders and G Székely (Berlin: Springer) (https://doi.org/10.1007/11790273_17)
- Huelke D F, Nusholtz G S and Kaiker P S 1986 Use of quadruped models in thoraco-abdominal biomechanics research *J. Biomech.* **19** 969–77
- Junatas K L, Tonar Z, Kubíková T, Liška V, Pálek R, Mik P, Králíčková M and Witter K 2017 Stereological analysis of size and density of hepatocytes in the porcine liver *J. Anat.* **230** 575–88
- Kemper A R, Santiago A C, Stitzel J D, Sparks J L and Duma S M 2010 Biomechanical response of human liver in tensile loading *Ann. Adv. Automot. Med.* **54** 15–26 (PMID: 21050588)
- King A I and Yang K H 1995 Research in biomechanics of occupant protection *J. Trauma* **38** 570–6
- Kozar R A, Crandall M, Shanmuganathan K, Zarzaur B L, Coburn M, Cribari C, Kaups K, Schuster K, Tominaga G T and AAST Patient Assessment Committee 2018 Organ injury scaling 2018 update: spleen, liver, and kidney [published correction appears in *J. Trauma Acute Care Surg.* 2019 Aug;87(2):512] *J. Trauma Acute Care Surg.* **85** 1119–22
- Kruepunga N, Hakvoort T B M, Hiksloops J P J M, Köhler S E and Lamers W H 2019 Anatomy of rodent and human livers: what are the differences? *Biochim. Biophys. Acta, Mol. Basis Dis.* **1865** 869–78

- Kubíková T, Kochová P, Brázdil J, Špatenka J, Burkert J, Králíčková M and Tonar Z 2017 The composition and biomechanical properties of human cryopreserved aortas, pulmonary trunks, and aortic and pulmonary cusps *Ann. Anat.* **212** 17–26
- Lee J B and Yang K H 2001 Development of a finite element model of the human abdomen *Stapp Car Crash J.* **11** 79–100
- Malečková A et al 2019 Animal models of liver diseases and their application in experimental surgery *Rozhl. Chir.* **98** 100–9
- Marchesseau S, Chatelin S and Delingette H 2017 Non linear biomechanical model of the liver: hyperelastic constitutive laws for finite element modeling *Biomechanics of Living Organs* ed Y Payan and J Ohayon (Cambridge: Academic)
- Mazza E, Nava A, Hahnloser D, Jochum W and Bajka M 2007 The mechanical response of human liver and its relation to histology: an *in vivo* study *Med. Image Anal.* **11** 663–72
- Melvin J, Stalnaker R, Roberts V and Trollope M 1973 Impact injury mechanisms in abdominal organs *Proc. 17th Stapp Car Crash Conf.* (Warrendale, PA: Society of Automotive Engineers) pp 115–26
- Meyers MA, Chen P Y, Lin A Y and Seki Y 2008 Biological materials: structure and mechanical properties *Prog. Mater. Sci.* **53** 1–206
- Mik P et al 2018 Distribution of connective tissue in the male and female porcine liver: histological mapping and recommendations for sampling *J. Comp. Pathol.* **162** 1–13
- Monchal T, Ndiaye A, Gadegbeku B, Javouhey E and Monneuse O 2018 Abdominopelvic injuries due to road traffic accidents: characteristics in a registry of 162 695 victims *Traffic Inj. Prev.* **19** 529–34 Moore
- E E et al 1989 Organ injury scaling: spleen, liver, and kidney *J. Trauma* **29** 1664–6 Ntonas A,
- Katsourakis A, Galanis N, Filo E and Nossios G 2020 Comparative anatomical study between the human and swine liver and its importance in xenotransplantation *Cureus* **12** e9411 Santiago
- A C, Kemper A R, McNally C, Sparks J L and Duma S M 2009 The effect of temperature on the mechanical properties of bovine liver —biomed 2009 *Biomed. Sci. Instrum.* **45** 376–81 (PMID: 19369792)
- Sparks J L, Bolte J H 4th, Dupaix R B, Jones K H, Steinberg S M, Herriott R G, Stammen J A and Donnelly B R 2007 Using pressure to predict liver injury risk from blunt impact *Stapp Car Crash J.* **51** 401–32 (PMID: 18278606)
- Sparks J L and Dupaix R B 2008 Constitutive modeling of rate-dependent stress-strain behavior of human liver in blunt impact loading *Ann. Biomed. Eng.* **36** 1883–92
- Sparks J L, Stammen J, Herriott R and Jones K 2008 Development of a fluid-filled catheter system for dynamic pressure measurement in soft-tissue trauma *Int. J. Crashworthiness* **13** 255–64
- Stoyan D, Kendall W S and Mecke J 1995 *Stochastic Geometry and its Applications* 2nd edn (New York: Wiley)
- Schoell S L, Weaver A A, Urban J E, Jones D A, Stitzel J D, Hwang E, Reed M P, Rupp J D and Hu J 2015 Development and validation of an older occupant finite element model of a mid-sized male for investigation of age-related injury risk *Stapp Car Crash J.* **11** 359–83 (PMID: 26660751)
- Schwartz D, Guleypoglu B, Koya B, Stitzel J D and Gayzik F S 2015 Development of a computationally efficient full human body finite element model *Traffic Inj. Prev.* **16** S49–56
- Tamura A, Omori K, Miki K, Lee J B, Yang K H and King A I 2002 Mechanical characterization of porcine abdominal organs *Stapp Car Crash J.* **11** 55–69 (PMID: 17096218)
- Tonar Z, Janáček J, Nedorost L, Grill R, Báca V and Zátura F 2009 Analysis of microcracks caused by drop shatter testing of porcine kidneys *Ann. Anat.* **191** 294–308
- Tropiano P, Thollon L, Arnoux P J, Huang R C, Kayvantash K, Poitout D G and Brunet C 2004 Using a finite element model to evaluate human injuries application to the HUMOS model in whiplash situation *Spine (Phila Pa 1976)* **29** 1709–16
- Untaroiu C D, Lu Y C, Siripurapu S K and Kemper A R 2015 Modeling the biomechanical and injury response of human liver parenchyma under tensile loading *J. Mech. Behav. Biomed. Mater.* **41** 280–91
- Vrtkova I 2015 Genetic admixture analysis in Prestice Black-Pied pigs *Arch. Anim. Breed.* **58** 115–21
- Vyčítal O, Horský O, Rosendorf J, Liška V, Skalický T and Třeška V 2019 Treatment of liver injuries at the Trauma Centre of the University Hospital in Pilsen *Rozhl. Chir.* **98** 488–91
- Wang B C, Wang G R, Yan D H and Liu Y P 1992 An experimental study on biomechanical properties of hepatic tissue using a new measuring method *Biomed. Mater. Eng.* **2** 133–8
- World Health Organization 2018 Road traffic injuries *World Road Safety Global Status Report on Road Safety* (<https://who.int/news-room/fact-sheets/detail/road-traffic-injuries>) (accessed 8 June 2020)
- Xu T, Sheng X, Zhang T, Liu H, Liang X and Ding A 2018 Development and validation of dummies and human models used in crash test *Appl. Bionics Biomech.* **38** 32850

Příloha VI:

MIK, P., Z. TONAR, A. MALEČKOVÁ, L. EBERLOVÁ, V. LIŠKA, R. PÁLEK, J. ROSENDORF, M. JIŘÍK, H. MÍRKA, M. KRÁLÍČKOVÁ a K. WITTER, 2018. Distribution of Connective Tissue in the Male and Female Porcine Liver: Histological Mapping and Recommendations for Sampling. *Journal of Comparative Pathology* [online]. 162, 1–13. ISSN 0021-9975. Dostupné z: doi:10.1016/j.jcpa.2018.05.004 **IF₂₀₁₇=1,364, Q2**(veterinary sciences)•



SPONTANEOUSLY ARISING DISEASE

Distribution of Connective Tissue in the Male and Female Porcine Liver; Histological Mapping and Recommendations for Sampling

P. Mik*, Z. Tonart, A. Malečková, L. Eberlová*, V. Liška!, R. Pálek!, J. Rosendorf, M. Jiřilá, H. Mirka!, M. Králíčková! and K. Witterl

* Department of Anatomy, Department of Histology and Embryology and Biomedical Center, Faculty of Medicine in Pilsen, Charles University, Karlovská 48, Department of Surgery and Biomedical Center, Faculty of Medicine in Pilsen, Charles University, Aleš SvoBODY & J. European Centre of Excellence JETIS, Faculty of Applied Sciences University of West Bohemia University, Ústí nad Labem, Department of Imaging Methods and Biomedical Centre, Faculty of Medicine in Pilsen, Charles University, University Hospital in Pilsen, Czech Republic, Institute of Anatomy, Histology and Embryology, Department for Pathology, University of Veterinary Medicine Vienna, Veterinärplatz 1, Vienna, Austria

Summary

The pig is a large animal model that is often used in experimental medicine. The aim of the study was to assess, in normal pig livers, sexual dimorphism in the normal fraction of hepatic interlobular and intralobular connective tissue (Cf) in six hepatic lobes and in three macroscopical regions of interest (ROIs) with different positions relative to the liver vasculature. Using stereological point grids, the fractions of Cf were quantified in histological sections stained with routine blue and fast red. Samples (415 tissue blocks) were collected from the adult piglets, representing paracaval, paraportal and peripheral ROIs. There was considerable variability in the Cf fraction at all sampling levels. In males the mean fraction of interlobular Cf was $4.7 \pm 2.4\%$ (mean \pm SD) and ranged from 0% to 11.4%. In females the mean fraction of the interlobular Cf was $3.6 \pm 2.2\%$ and ranged from 0% to 12.3%. The mean fraction of intralobular (perisinusoidal summed with pericentral) Cf was $<0.2\%$ in both sexes. The interlobular Cf represented $>99.8\%$ of the total hepatic Cf and the fractions were highly correlated (Spearman $r = 0.998$, $P < 0.05$). The smallest Cf fraction was observed in the left medial lobe and in the paracaval ROI. The largest Cf fraction was detected in the quadrilateral lobe and in the peripheral ROI. For planning of experiments involving the histological (quantification of liver fibrosis) and requiring comparison between the liver lobes, the data indicate the power analysis for sample size needed to detect the expected relative increase or decrease in the fraction of Cf.

© 2018 Elsevier Ltd. All rights reserved.

Keywords: connective tissue; histology; liver; pig

Introduction

Both small and large animals are used to study the mechanisms of the origin and spread of liver fibrosis, often together with the regenerative capacity and healing of the liver. Fibroses of different aetiologies have been studied predominantly in mice (George

et al., 2003; Anstee and Goldin, 2006; Machado *et al.*, 2015) and rats (Yi *et al.*, 2012; Nowatzky *et al.*, 2013; Fakhoury-Sayegh *et al.*, 2015). However, small animal models of liver fibrosis have several limitations due to the small organ size (Lossi *et al.*, 2016). Therefore, it is usually not possible to study phenomena such as portocentral and portoportal bridging fibrosis, modelling of the biomechanics of trauma, lobar resection and regeneration or surgical

Correspondence to: Z. Tonart (e-mail: Zbynck.Tonart@lip.eu11.e2).

techniques. Large animal models are needed for the improved translation of experimental work into human medicine. Apart from sheep liver (Ghodsizad *et al.*, 2012), the porcine liver is the most widely used large animal model (Avritscher *et al.*, 2011; Kawamura *et al.*, 2014; Bruha *et al.*, 2015; Nygrad *et al.*, 2015; Wang *et al.*, 2015) to study improvements in invasive (Croome *et al.*, 2015) and **non-invasive methods of liver disease management** (Gnutzmann *et al.*, 2015), to interpret animal experiments and to translate the results of animal models to human medicine (Arkadopoulos *et al.*, 2011; Watson *et al.*, 2016; Budai *et al.*, 2017). Chen *et al.* (2013) showed that histological assessment of liver fibrosis in the pig correlates with non-invasive magnetic resonance imaging. Combining the data obtained for connective tissue (CT) with data on the microvasculature of the porcine liver (Eberlova *et al.*, 2016, 2017) would improve existing models of **human liver perfusion. Moreover, fibrosis is an important part of porcine liver diseases, such as in pigs suffering from biliary and peribiliary cysts (Komine *et al.*, 2008) or swine hepatitis E (Lee *et al.*, 2010).**

Summarizing the present literature, porcine liver fibrosis and cirrhosis of different aetiologies can be used as a model for human liver fibrosis and cirrhosis (Avritscher *et al.*, 2011). In the porcine liver, fibrosis is usually induced by CCL₄ (Zhang *et al.*, 2009), by alcohol (Lee *et al.*, 2017), by a high-fat diet or by a Western-style diet (Panasevich *et al.*, 2018) or by using pentoxifylline (Peterson and Neumeister, 1996). It has been proposed that porcine liver fibrosis may be staged according to human standards using the Metavir scoring system (Ishak *et al.*, 1995; Zhou *et al.*, 2014; Yin *et al.*, 2017); however, this required several modifications (Huang *et al.*, 2014, 2017).

The major fibrogenic cells in the liver are the hepatic stellate cells, portal fibroblasts, fibrocytes, bone marrow-derived cells that are activated and transdifferentiated into hepatic myofibroblasts and possibly hepatocytes and cholangiocytes that transition to myofibroblasts (Forbes and Parola, 2011; Zhao *et al.*, 2016; Kisseleva, 2017). Histological assessment of the location of fibrosis and identification of the source of fibrogenic cells is necessary when assessing the severity of the liver disease and the patient's prognosis (Takahashi and Fukusato, 2014; Stasi and Milani 2016). Biopsy samples are usually scored in terms of their grade (Scheuer, 1991) and stage (Saxena, 2011). Six specific loci of liver fibrogenesis have been proposed for scoring, namely portal, pericellular (i.e. perisinusoidal), pericentral (i.e. perivenular), centrilobular, ductal (i.e. periductal) and ductular (Batts and Ludwig, 1995; Gohlke *et al.*,

1996; Brunt *et al.*, 1999; Sakhuja, 2014; Takahashi and Fukusato, 2014).

During chronic hepatitis, fibrosis starts and spreads from portal regions, forming stellate periportal scars or enlarging the portal tracts (Lelkowitz, 2007). Steatofibrosis in alcoholic liver disease begins in the pericentral region and extends in a perisinusoidal pattern, where it is more pronounced than in hepatitis C infection (Zaitoun *et al.*, 2001). This phenomenon leads to centroportal and portoportal bridging and, together with the regenerating nodular parenchyma, results in cirrhosis (Theise, 2013). Similar histological findings have been reported in non-alcoholic fatty liver disease (NAFLD) or non-alcoholic steatohepatitis (NASH), but lack the pericentral origin of fibrosis (Brunt *et al.*, 1999; Kleiner *et al.*, 2005; Takahashi and Fukusato, 2014). Primary biliary cirrhosis involves fibrosis of small intrahepatic bile ducts (Lindor *et al.*, 2009; Working Subgroup for Clinical Practice Guidelines for Primary Biliary Cirrhosis, 2014). Central hepatic veins are often retained in their centrilobular location, even in cirrhosis. Sclerosing cholangitis shows bile duct scarring, biliary fibrosis, leading eventually to cirrhosis (Hirschfield *et al.*, 2013; de Vries *et al.*, 2015).

The amount of CT in the human liver is usually estimated during routine analysis of liver biopsy samples, according to widely used scoring systems (Scheuer, 1991; Ishak *et al.*, 1995; Bedossa and Poynard, 1996). However, Standish *et al.* (2006) highlighted several limitations of subjective or semiquantitative scoring as **both the interobserver and intraobserver variability might disqualify the data generated from comparative studies or from evaluations of non-invasive methods of liver fibrosis. Therefore, the need for an objective, reproducible measure, preferably generating continuous data, has been articulated (Saxena, 2011).**

To the best of our knowledge, no published data are available for continuous quantitative histological parameters that demonstrate the normal intersexual and interindividual variability in the fraction of CT in various macroscopical regions of porcine liver lobes. Therefore, the aim of the present study was to assess the content and distribution of normal hepatic CT in the domestic pig and to provide sampling recommendations for further histopathological studies. The following null hypotheses were tested: (1) the volume fraction of CT in the liver is the same in male and in female pigs, (2) the volume fraction of CT in the liver is the same in all hepatic lobes and (3) the volume fraction of CT in the liver is the same in three macroscopical regions with different positions related to the liver vasculature (regions of interest; ROIs): the peripheral regions of the liver lobes, the regions near

the porta hepatis and the regions adjacent to the caudal vena cava.

Material and Method

Animals

As a part of this study we used liver samples collected previously for studies of the size and density of hepatocytes in the porcine liver (Junatas *et al.*, 2017). Five more animals were added. Briefly, liver samples were obtained from 12 healthy Prestice black-pied pigs (Vrtková, 2015) aged 9–15 weeks and weighing 25–45 kg (34.3 ± 5.3 kg, mean \pm standard deviation, at Jon [SOJ]). Six piglets were male and six piglets were female (see Supplementary Table I for sample details). All animals received humane care in compliance with the European Convention on Animal Care and project number 27374/2011-30 was approved by the Faculty Committee for the Prevention of Cruelty to Animals. The animals were premedicated (with atropine, ketamine and azaperone), anaesthetized (with propofol and fentanyl), relaxed (with pancuronium), intubated and mechanically ventilated. Fluid infusion and volume restoration were provided (Plasmalyte™ solution and Gelofusine™ solution; B-Block, Melsungen, Germany). Animals were killed under anaesthesia by administration of cardioplegic solution (KCI). Immediately after sacrifice, the whole liver was removed. The fresh liver volumes ranged from 0.640 to 1.200 l and the mean \pm SD values were 0.871 ± 0.146 l.

Tissue Sample Collection

Each liver was sectioned into 1.5 cm thick slices and immersed in 10% neutral buffered formalin. From each liver, 36 tissue samples (each approximately 25 x 25 x 15 mm) were collected to represent six hepatic lobes (i.e. left lateral, left medial, right medial, right lateral, caudate and quadrate) and three different positions (ROIs) relative to the liver vasculature (Fig. 1A). In each lobe, two samples represented the peripheral ROIs, two were from the paracaval ROIs and two were from the parportal ROIs. The peripheral ROIs were defined as located no more than 1 cm from the surface and periphery of each hepatic lobe. The paracaval location was the region of each lobe immediately adjacent to the openings of the hepatic veins into the caudal vena cava. The parportal (biliary) location was adjacent to the main branches of the porta venae following from the hilum within each anatomical lobe.

In total, 415 tissue samples were collected (in three animals, the size of the quadrate lobe did not allow collection of separate tissue samples; moreover, three other samples were lost during processing). Before

cutting, the orientation of each tissue block was randomized using the orientator scheme (Matfeldt *et al.*, 1990; Mihihfeld *et al.*, 2010).

Volumetric Analysis of Regions of Interest

Volumetric analysis of the ROIs was based on computed tomography. The borders between ROIs were mapped to guarantee that each region represented approximately one third of the volume of each lobe. Therefore, the sampling described above was not biased by different relative volumes of the ROIs. Prior to sampling, the liver was scanned using a Somatom Definition Flash Dual Source Computed Tomography Scanner (Siemens, Erlangen, Germany) and the Syngo software kernel. The section thickness was 0.65 mm and the voxel size was $0.65 \times 0.65 \times 0.40$ mm³. A typical tomography stack consisted of 700–800 sections. Assignment of the liver parenchyma to the paracaval, parportal and peripheral ROI was done using the USA (Liver Surgery Analyzer) software (Jirík *et al.*, 2018), a free and open-source application intended for computer-aided liver surgery and measurement. Liver segmentation was performed using a 3D Gradient-Cut algorithm (Boykov and Jolly, 2000). For the measurement of ROI respective volumes, the porta venae vascular bed and the hepatic vein vascular bed were segmented separately. The liver parenchyma was assigned to the respective vascular bed by its position within the ball-distance between two vascular beds using the Euclidean Distance Transform. In the second step, we arbitrarily cut-off the peripheral third of the liver parenchyma and assigned it to the peripheral ROI. The mean volumes of each ROI were set to one-third of the total liver parenchyma volume (see an example in Fig. 1B).

Histological Processing

The tissue blocks were processed routinely and embedded in paraffin wax. Three sections (3 μ m) were cut from each block and one was selected randomly and used for further analysis. After dewaxing and rehydration, nuclei were stained with nuclear fast red (Waldeck GmbH, Munster, Germany). After washing in distilled water, the sections were differentiated in 5% phosphotungstic acid and washed again in distilled water. Collagen fibres were stained with 0.5% aniline blue (Merck KGaA, Darmstadt, Germany).

Microscopic Sampling and Quantification of Volume Fraction of Connective Tissue

All quantified parameters are listed in Table I. The first step comprised a systematic uniform random

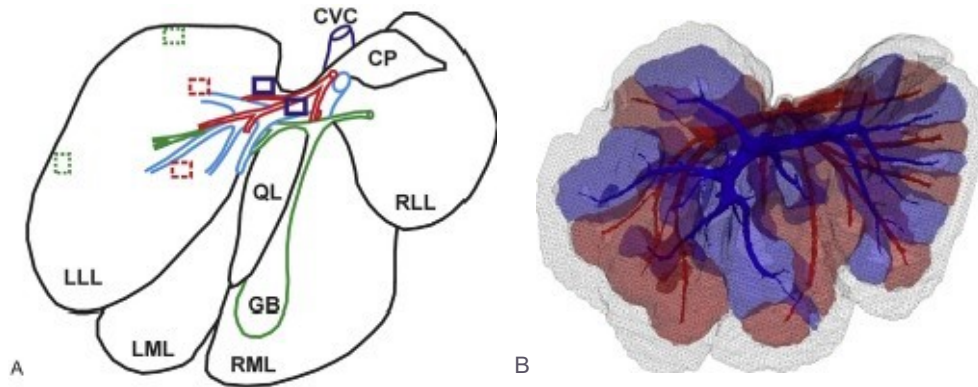


Fig. 1. Collection of tissuesamplesofthe porcine Liver for quantitative histology and the relative volumes of the regions of interest (ROIs). (A) As shown on a drawing of the facial surface of the porcine liver, the sampling strategy was the same as in J. Unata et al. (2017). This scheme outlines the left lateral lobe (LLL), left medial lobe (LML), right medial lobe (RML), right lateral lobe (RLL), quadrate lobe (QL) and caudate lobe (QL). In addition to the vessels, the scheme shows the caudate process (CP), the gallbladder (GB) and the caudal vena cava (CVC). Branching of hepatic arteries is shown in red, branching of the portal vein in blue and branching of the bile ducts in green. The LLL is used as an example of collection of histological samples from the ROIs: paracaval region (dark blue rectangles drawn with a continuous line), paracaval region (red rectangles with a dashed line) and the peripheral region (green rectangles with a dotted line). Samples of the other lobes were collected accordingly. (B) Visualization of the ROIs representing approximately the three thirds of the total volume of the porcine liver. The liver was scanned using computed tomography and the reconstruction was rotated so that the visceral surface is shown from a caudal view. In this individual, the paracaval region with associated hepatic vessels is shown in red (volume = 0.3881), the peripheral region is shown in black (volume = 0.4271) and the peripheral region with the branching of the portal vein is shown in blue (volume = 0.4001). The volumes of the blood vessels were subtracted from the ROIs.

sampling of microscopical image fields within each section according to Fig. 2A. To quantify the interlobular CT V_{17} (ICT) (i.e. CT surrounding classical lobules), three uniform random fields of view (FOVs) at $\times 10$ magnification were captured, while to quantify the perisinusoidal CT V''' (PSCCT) (i.e. intralobular CT adjacent to the liver sinusoids) and pericentral CT V'' (PCCT) (i.e. CT surrounding the central veins), four uniform random FOVs at $\times 20$ magnification were photographed (Fig. 2A) at a resolution of 1,280 \times 960 pixels. In the second step, a stereological

point grid was applied over the FOVs in the Ellipse software (ViDiTo, Kosice, Slovak Republic; Tonar *et al.*, 2015; Kubíková *et al.*, 2017) to quantify the volume fraction of each Cf type (Figs. 2B and C). The areas occupied by the Cf were equal to the corresponding volume fractions according to the Delesse principle (Mouton, 2011). The fibrous capsule of the liver, which was present in the samples from the peripheral region, was omitted from the quantification. Any tissue processing artifacts, such as microcracks or folds, were not evaluated and were subtracted from

Table I
Stereological parameters used for porcine liver connective tissues

Abbreviation and unit	Definition	Sampling method
Volume fraction of interlobular connective tissue V_v (ICT)	Fraction of connective tissue surrounding classical lobules within the liver	Point grid
Volume fraction of perisinusoidal connective tissue V_v (PSCCT)	Fraction of connective tissue located at or in the lobular sinusoids within the liver lobules	Point grid
Volume fraction of pericentral connective tissue V_v (PCCT)	Fraction of connective tissue surrounding the central vein within the liver lobules	Point grid
Volume fraction of total connective tissue V_v (CT)	Sum of the V_v (ICT) + V_v (PSCCT) + V_v (PCCT) (POCT)	None (calculated from previous three parameters)

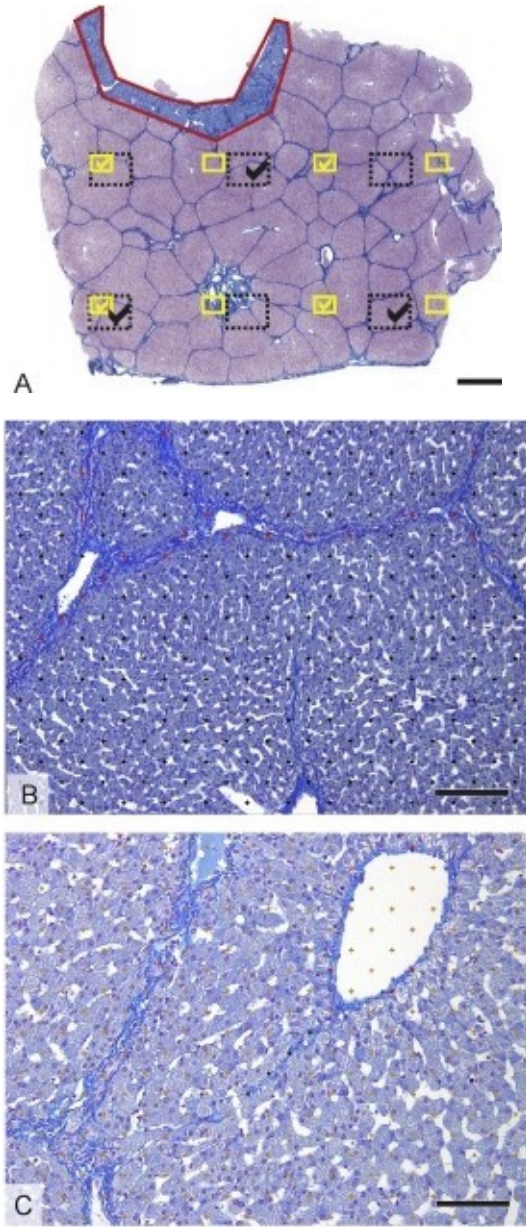


Fig. 2. Histological Sampling and quantification of connective tissue. (A) Fields of view (FOVs) sampled, captured and used for quantification of connective tissue. For interlobular connective tissue (ICT), three FOVs observed with X100 objectives were sampled (black dotted rectangles, MCd FOV = $870 \times 653 \mu m$). For perisinusoidal connective tissue (PSCT) and pericentral connective tissue (PCCT), four FOVs with X20 objectives were used (black dotted rectangles, size of FOV = $435 \times 326 \mu m$). The first FOV was positioned randomly, starting from the top left corner of the section and further FOVs were placed equidistantly using a micrometer. The FOVs photographed from this systematic uniform sampling pattern are marked on the schematic with check marks. The hepatic capsule (outlined red) was omitted from the quantification. (B) Stereological point grid used for quantification of ICT. Points hitting the ICT are highlighted in red. (C) Stereological point grid used for quantification of PSCT (highlighted in black) and PCCT (highlighted in red). Detection of collagen using aniline blue staining counterstaining with nuclear fast red. Bars, 1 mm (A), $200 \mu m$ (B), $100 \mu m$ (C).

the reference space. We did not observe any differential shrinkage between the Cf and the liver parenchyma.

Statistical Analysis

The study was based on the quantification of 2,905 micrographs sampled from 415 histological tissue blocks. The Statistica Base 11 software package (StatSoft, Inc., Tulsa, Oklahoma, USA) was used for the statistical analysis. The Shapiro-Wilk's W-test for normality showed that some of the data were not distributed normally. Therefore, we used non-parametric tests for further analysis. To assess differences between the male and female animals, among the six liver lobes, the differences between the different ROIs, the differences between $V_{17}(PSC T)$ and $V_{17}(PCCT)$, the Kruskal-Wallis ANOVA and the Mann-Whitney U-test were used. As an example of the use of our data, the possible sample size calculation for the porcine liver is shown: a power analysis (Chow et al., 2008) was performed to illustrate the sample size needed to detect the expected relative change in the fraction of CT in various hepatic lobes and ROIs.

Coefficient of Error

Estimation of the volume fraction of CT and the size of hepatic lobules was based on two tissue sections per tissue block. However, the values of these parameters might differ between individual histological sections. Therefore, we assessed the volume fraction of CT and the size of hepatic lobules in series of 12 equidistant sections in four randomly selected tissue samples. To provide recommendations for sampling the sections, the variation quantified in the serial sections was estimated using the moving average of the CT fraction and the coefficient of error (CE) (Gundersen and Jensen, 1987).

Results

There was considerable variability in the Cf fraction at all sampling levels of the study: between sexes, among individual animals, liver lobes and ROIs. The mean fraction of interlobular CT was greater in males than in females ($P < 0.001$) (Fig. 3A). In males, the mean fraction of interlobular Cf was $4.7 \pm 2.4\%$ (mean \pm SD; Fig. 3B) and ranged from 0% to 11.4%. In females, the mean fraction of interlobular Cf was $3.6 \pm 2.2\%$ (Fig. 3C) and ranged from 0% to 12.3%. The mean fraction of intralobular (i.e. perisinusoidal summed with pericentral) CT was $< 0.2\%$ both in males and in females; the V_{17} (PSCT) was $0.003 \pm 0.02\%$ in males and $0.002 \pm 0.02\%$ in

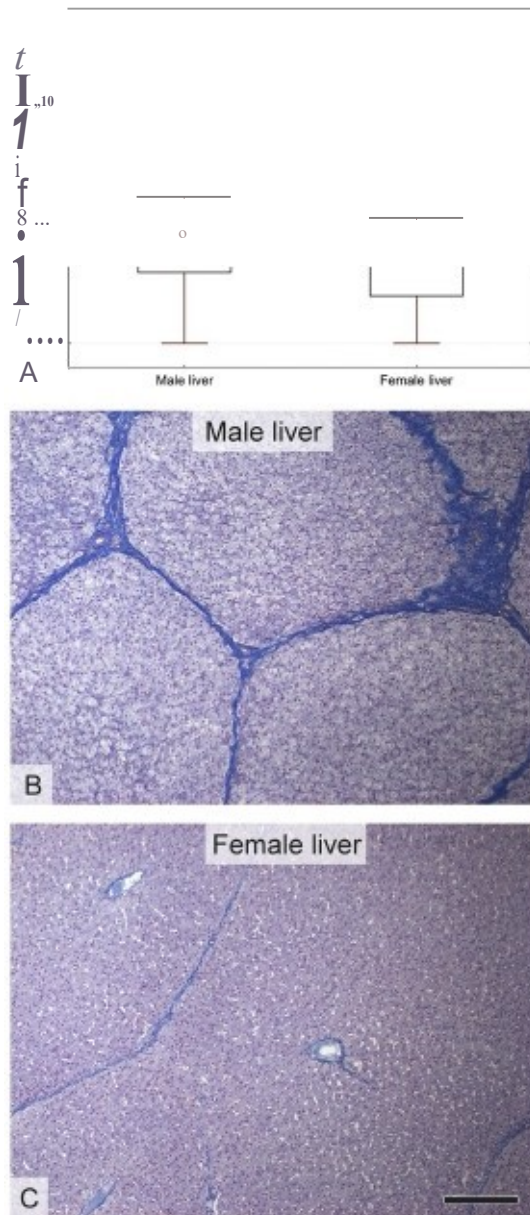


Fig. 3. Fraction of interlobular connective tissue in male versus female animals (A) In the male porcine liver the volume fraction of connective tissue (mean = 4.7%) was significantly higher ($p < 0.001$, Mann-Whitney U-test) when compared with female liver (mean = 3.6%). The statistical findings are illustrated with histological pictures taken randomly from the paracaval region of the lateral lobe in: (B) a male pig and (C) a female pig. Aniline blue and nuclear fast red, Bar, 200 μm (B).

females and the V_v (PCCT) was $0.03 \pm 0.1\%$ in males and $0.04 \pm 0.1\%$ in females. Unlike in females, the fraction of pericentral CT in males was greater than the fraction of the perisinusoidal CT ($P < 0.01$). The interlobular CT represented $> 99.9\%$ of the total hepatic CT and their fractions were mutually highly

correlated (Spearman $r = 0.998$, $P < 0.05$). The complete stereological results for all samples are provided in [Supplementary Table 1](#).

Volume Fractions of Connective Tissue

In male pigs, the only significant differences in the fraction of interlobular CT among hepatic lobes were observed between the quadrate and left medial lobe ($P < 0.05$) and between the quadrate and right medial lobe ($P < 0.05$) (Fig. 4A). The paracaval ROI was the region with the smallest volume fraction of interlobular CT ($3.9 \pm 2.3\%$, $P < 0.01$). The parportal ROI ($4.9 \pm 2.0\%$) and the peripheral ROI ($5.2 \pm 2.5\%$) had a greater fraction of CT (Fig. 4B). Other differences in interlobular CT among the ROIs were not significant. The same differences were detected when the total CT fraction was analysed. The fractions of both the perisinusoidal and the pericentral CT were negligible ($< 0.2\%$).

In female pigs, the volume fractions of interlobular CT differed between the left medial lobe and the caudate lobe ($P < 0.05$) and the quadrate lobe ($P < 0.05$), and between the right medial lobe and the caudate lobe ($P < 0.05$; Fig. 4A). The volume fraction of interlobular CT was greater in the peripheral ROI ($4.1 \pm 2.4\%$) than in the paracaval ROI ($3.1 \pm 2.0\%$) ($P < 0.05$; Fig. 4B). The fractions of both the perisinusoidal and the pericentral CT were negligible ($< 0.2\%$).

Qualitative Findings

Histological images illustrating the typical findings in liver lobes are shown in [Supplementary Fig. 1](#) and [Fig. 5](#). Apart from the typical histological findings of regularly arranged lobules (Fig. 5A), several less common histological characteristics were found. In the paracaval region of the caudate lobe, the hepatocytes within the lobules below the fibrous capsule showed shape elongation (Fig. 5B), which currently cannot be distinguished from an artifact. In the peripheral region of the left medial lobe, more (or branching) central veins were found (Fig. 5C). In the peripheral region of the left medial lobe, incompletely separated lobules (Fig. 5D) were found.

Coefficients of Errors in Serial Sections

Analysis of four series of 12 serial sections revealed the relationship between the CEs and the number of histological sections selected for the analysis (Table 2). The data suggested that using four sections for quantification of both the fraction of CT in liver instead of one section would have reduced the sampling error to an acceptable value of approximately 0.11.

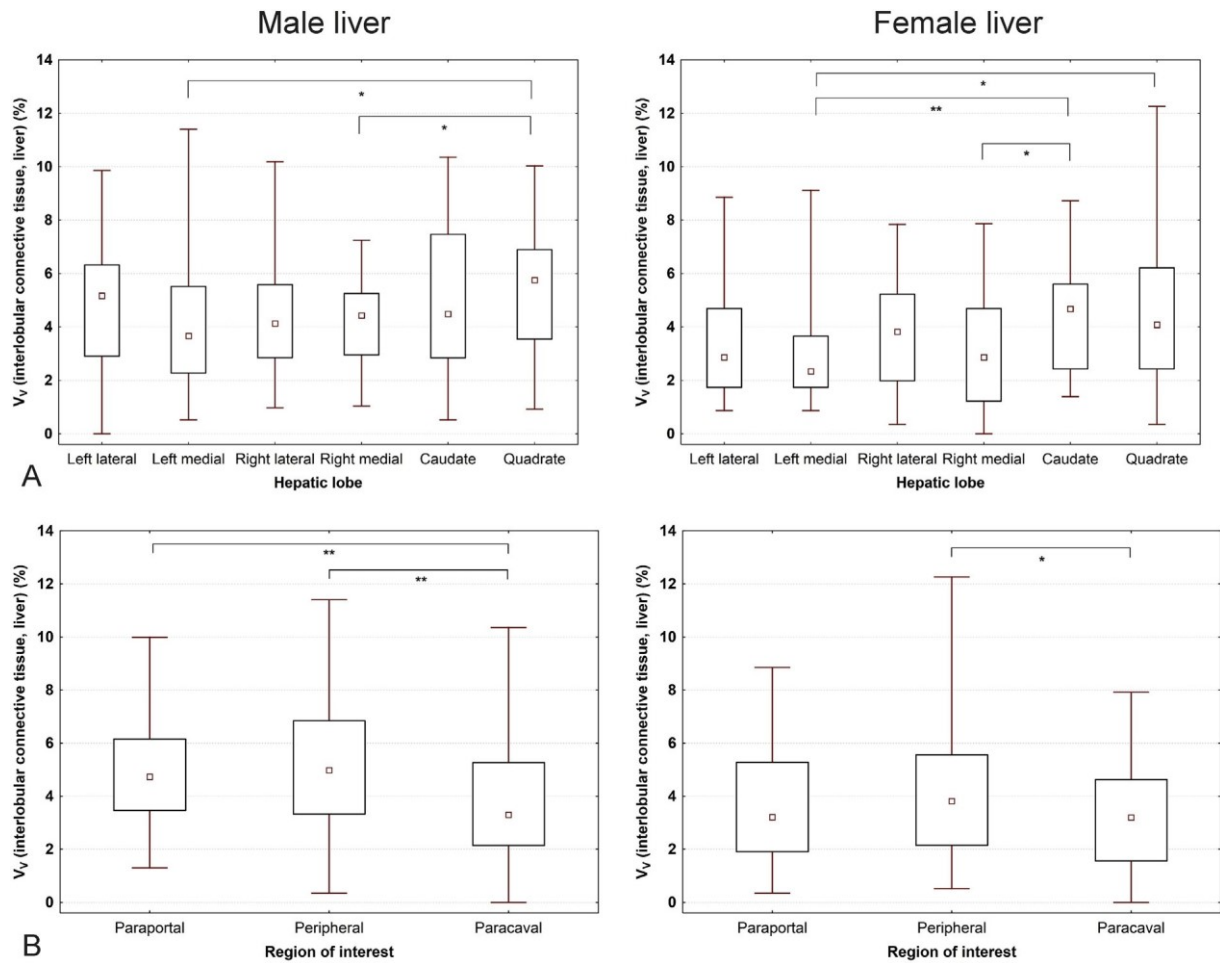


Fig. 4. Fraction of interlobular connective tissue (ICT) in male (on the left) and female (on the right) pig livers. The data are presented in six porcine hepatic lobes (A) and in regions of interest (ROIs) with respect to their proximity to the liver vasculature (B). (A) In males (left), the fraction of ICT was greater in the quadrate lobe than in the left medial and right medial lobes. The left medial lobe contained the smallest fraction of ICT (median 3.67%), the quadrate lobe contained the largest fraction of ICT (median 5.75%). In females (right), the fraction of ICT was greater in the caudate lobe than in the left medial and right medial lobes and was smaller in the left medial lobe than in the quadrate lobe. The left medial lobe contained the smallest fraction of ICT (median 2.34%), the caudate lobe contained the largest fraction of ICT (median 4.67%). (B) In males (left), the fraction of ICT was the smallest in the paracaval ROI (median 3.30%). In females (right), the fraction of ICT was smaller in the paracaval ROI than in the peripheral ROI. Data are displayed as median values with boxes spanning the limits of the first and third quartiles and whiskers spanning the minimum and maximum values for each group. Significant differences ($*p < 0.05$, $**p < 0.01$, $***p < 0.001$) identified by the Mann-Whitney U -test are presented. See [Supplementary Table 1](#) for the source data.

Calculating the Sample Size for Histological Evaluation of Hepatic Fibrosis in Pigs

The number of histological samples needed to detect an expected relative increase in the CT fraction in various hepatic lobes and ROIs is shown in [Fig. 6](#). The number of tissue samples needed for comparison rapidly decreased with an increasing expected change. This phenomenon applied especially to lobes with a relatively high (e.g. quadrate lobe, [Fig. 6B](#)) or intermediate (e.g. left lateral lobe, [Fig. 6A](#)) intralobar variation among the ROIs. We also simulated an experiment with pooled lobes (e.g. for cases where

the anatomical origin of the histological samples from the lobes would not be known, but the ROIs would be known) ([Fig. 6C](#)). The case with unknown ROIs, but known lobes, is shown in [Fig. 6D](#). Source data for all lobes and ROIs are provided in [Supplementary Tables 2 and 3](#).

Discussion

The detected variability in the volume fraction of CT between sexes can be attributed to the effect of sex hormones, especially oestrogen that has a protective effect against fibrogenesis ([Yang et al., 2014](#)).

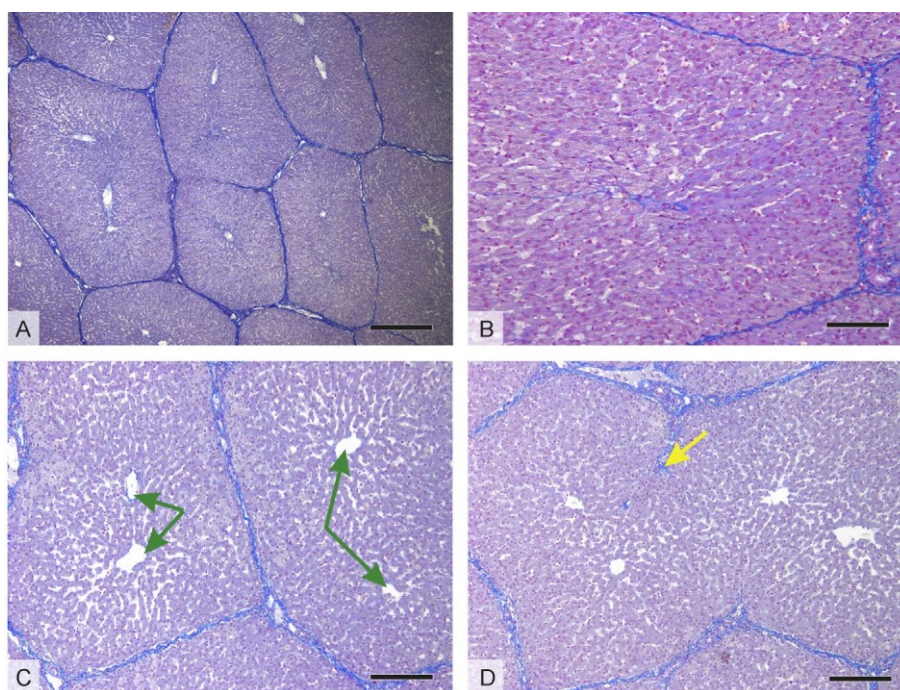


Fig. 5. Illustration of qualitative histological findings in the porcine liver. (A) Typical histological findings of regularly arranged lobules. (B) In the paracaval region of the caudate lobe, the hepatocytes within the lobules adjacent to the fibrous capsule are attenuated and elongated. The possibility that this could be an artifact cannot be excluded. (C) In the peripheral region of the left medial lobe, more (or branching) central veins are found (green arrows). (D) In the peripheral region of the left medial lobe, incompletely separated pseudolobules (yellow arrow) are found. Aniline blue and nuclear fast red staining. Bars, 500 μ m (A), 100 μ m (B), 200 μ m (C, D).

Table 2
of the coefficient of error (CE) estimating the amount of sampling error between the serial histological sections in four randomly selected samples of the porcine liver

Number of serial sections sampled	2	3	4	5	6	7	8	9	10
CE (%)	21.3	14.6	11.3	8.70	8.70	7.49	6.66	5.85	5.47

For each of the four samples the volume fraction of interlobular CT was analysed. The mean CE (Gundersen and Jensen, 1987) decreases with increasing numbers of analysed sections.

Therefore, in pre-menopausal women (Yang *et al.*, 2014), as well as in female Wistar rats (Marcos and Correia-Gomes, 2015), the amounts of CT in the liver tend to reach lower values relative to male counterparts. The sex-related differences in rats included mainly increased perisinusoidal fibrous tissue deposition in males with ageing (Marcos and Correia-Gomes, 2015). Our results add to the evidence for a greater volume fraction of CT in male porcine livers when compared with their female counterparts.

To our best of our knowledge, no data explaining the differences in variable fractions of CT in various ROIs and lobes have been published. The only known data show preferential distribution of types of collagen, namely: type I and type III collagen co-localize in the same fibre bundles both outside the hepatic lobule (i.e. in the portal tracts) and within the hepatic lobule (Mak *et al.*, 2012), while collagen IV is found only

within the hepatic lobule (Mak *et al.*, 2013). Our present findings on the greater fraction of CT in peripheral ROIs could be answered by further studies: (1) mapping the distribution of brogenic cells, and (2) mapping quantitatively the local differences in the hepatic microvascular bed (Zhang *et al.*, 2015). Although brogenic cells within the liver have been studied (Zhao *et al.*, 2016; Kisseleva, 2017), their differential distribution within liver compartments has not yet been mapped. The greater content of CT in peripheral ROIs found in our study could be explained by the proximity to mesothelial cells that count as liver brogenic cells (Lua *et al.*, 2015).

The fraction of CT in the normal porcine liver in our study was considerably higher than that in most other animals or in man. CT is hardly visible in the dog, goat, horse, cat, rat and man; however, CT is clearly visible in the guinea pig, hamster, sheep and

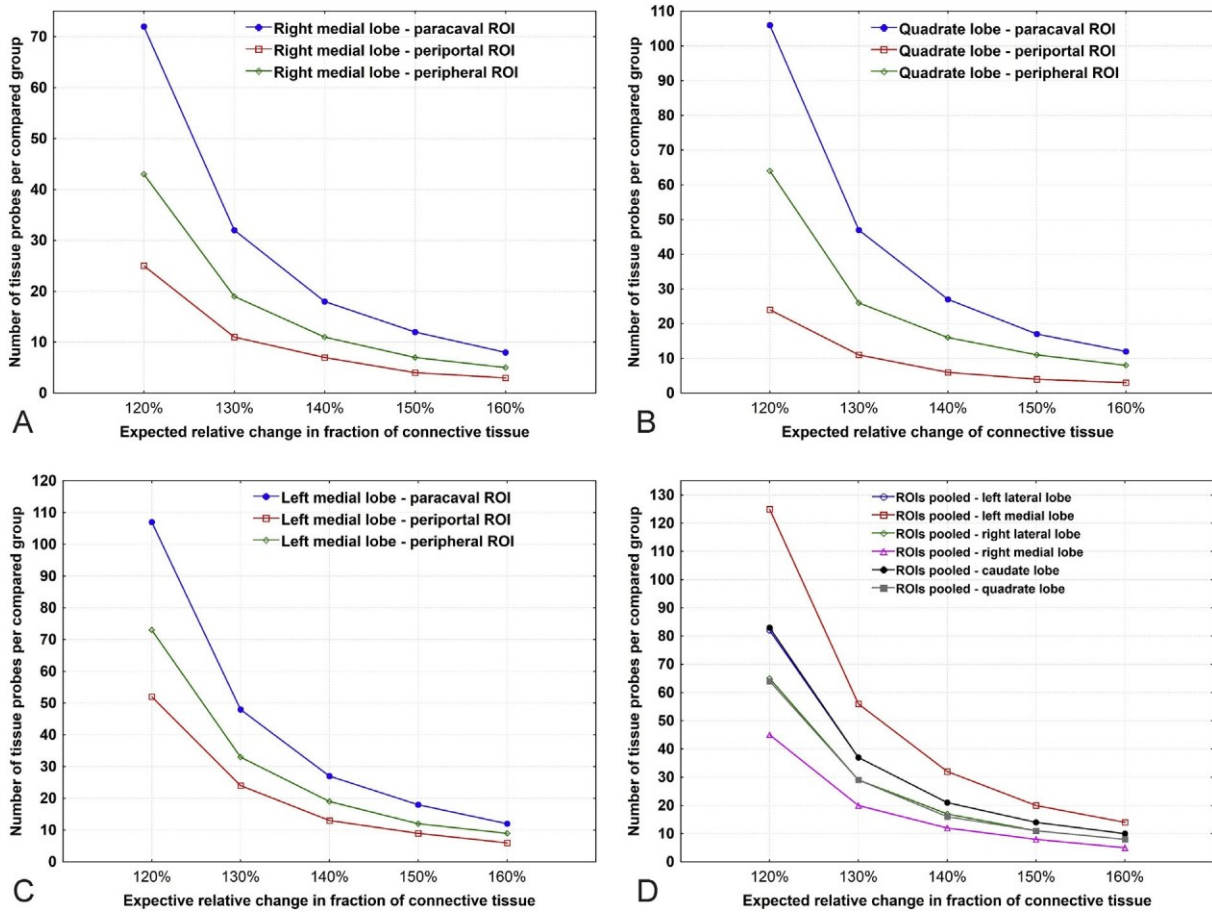


Fig. 6. Examples for calculating the sample size needed to detect a certain expected relative increase in the connective (CT) fraction in various hepatic lobes and ROIs in male pig liver. In each of the graphs, the x-axis shows the expected change in the CT fraction (i.e. an expected 30% increase in the fraction of CT corresponds to 130% on the x-axis). The y-axis shows the number of tissue blocks needed from a group under study to detect the expected change calculated according to [Chow et al. \(2008\)](#). The number of tissue blocks needed for comparison rapidly decreases with an increasing expected change. (A) In male porcine liver, in the right medial lobe, the greatest coefficients of intralobar variability were found ([Supplementary Table 2](#)). Detecting a 30% increase in CT would require, for example, 40 tissue blocks in the paraportal regions and 61 blocks in the paracaval regions. (B) The quadrate lobe had an intermediate intralobar variability of CT (see the coefficients of variation in [Supplementary Table 2](#)), for example, detecting a 30% increase in CT would require 11 tissue blocks in the paraportal regions and 47 tissue samples in the paracaval regions. (C) When all of the lobes are pooled, detection of a 30% increase in the fraction of CT requires at least 24 tissue blocks (paraportal ROI) in each group under study. (D) When comparing the variability inside the lobes by pooling their paracaval, paraportal and peripheral regions, detecting the same increase in the CT fraction inside the right medial lobe (pink line) would require fewer samples than detecting the same changes in the left medial lobe (red line). This observation shows the importance of respecting the anatomical lobes and ROIs when sampling the porcine liver for histological analyses. Source data are provided for male and female animals separately in [Supplementary Tables 2 and 3](#).

pig. Studies using transmission electron microscopy ([Hosoyamada et al., 2000](#)) revealed detailed patterns of length distribution of collagen fibrils. The mean amount of CT in the porcine liver is approximately double that found in the rat liver ([Marcos and Correia-Gomes, 2015](#)). Other numerical data are sparse, both for small and large animals. Moreover, few studies in animals have used an unbiased stereological design ([Zaitoun et al., 1998](#); [Marcos et al., 2012](#) and [Supplementary Table 4](#)). The importance of a quantitative approach proved to be useful: in

our study, quantification revealed several differences, which were scarcely visible using routine qualitative histology ([Supplementary Fig. 1](#)).

For studies of human liver diseases, such as chronic hepatitis C infection ([Besusparis et al., 2014](#)), alcoholic liver disease and non-alcoholic liver disease ([Sakhuja, 2014](#)), primary biliary cirrhosis ([Working Subgroup for Clinical Practice Guidelines for Primary Biliary Cirrhosis, 2014](#)) or sclerosing cholangitis ([de Vries et al., 2015](#)), using porcine liver as an experimental model, it should be noted that the

norma) amounts of CT in porcine liver already resemble fibrosis in human livers (Saxena, 2011). Moreover, the distribution of interlobular and intra-lobular CT in pigs and in humans has different patterns. The use of our data as a basis for the design of the following studies is explained in Fig. 6 as follows. In the male porcine liver, the mean fraction of interlobular CT in right medial lobes is $4.27 \pm 1.62\%$; therefore, if we expect, for example, a 30% increase in CT in the porcine liver (to 5.99%), then we should compare at least 11 tissue blocks in each of the compared groups (power = 0.8; significance level = 0.05); however, this is only true when we know the exact position of the tissue blocks with respect to the liver lobe and to the ROI. If we know only the lobe of origin of the tissue blocks, then we should compare at least 20 tissue blocks in each of the compared groups. If the positions of the tissue blocks for comparison are unknown (i.e. all the lobes would be pooled, e.g. when assessing archival samples), the variability between the lobes, the ROIs and between the individuals would affect the study design in such a way that at least 36 tissue blocks for each of the compared groups should be sampled to detect the same degree of fibrosis. When the sampling scheme of experiments using the porcine liver reflects the differences between the lobes and the ROIs, the **same quantitative information may result from a more efficient comparison to the situation in which the tissue blocks are harvested in a purely random manner.**

The population of animals used in this study was of the **minimum size allowed for use of non-parametric statistical tests** ($n > 6$). In large animal models, such as the pig, experiments are typically done using relatively small numbers of animals according to the principles of the '3Rs' (replacement, reduction and refinement; Emerson, 2010). This strategy suffers from an increased variability of results caused by interindividual differences, but the researchers are simulated to follow large biological effects that are observable even in small study groups. Since our study was performed on piglets aged 9-15 weeks, an ontogenetic perspective should also be considered in future studies. Age-related differences are to be expected. Although mechanisms of fibrogenesis during liver development have been studied (Lepreux and Desmoulière, 2015), to the best of our knowledge, no study quantifying the amount of CT during liver development has been conducted to date.

In conclusion, for planning experiments involving the histological quantification of liver fibrosis and requiring comparison between the liver lobes, these data facilitate the power analysis for the sample size

needed to detect the expected relative increase or decrease in the fraction of CT.

Acknowledgements

This study was supported by the National Sustainability Programme I (NPU I) number LO1503 and number LO1506 provided by the Ministry of Education, Youth and Sports of the Czech Republic and by the Charles University Research Fund (Progress Q39). The project also received support from Charles University Project numbers SVV 260390/2017, SVV 260392/2017 and GAUK 1206417 and from the project of the Centre of Clinical and Experimental Liver Surgery UNCE/MED/006 and Application of Modern Technologies in Medicine and Industry CZ.02.1.01/0.0/0.0/17_048/0007280. The study also received support from the Ministry of Education, Youth and Sports under the project FINE, number CZ.02.1.01/0.0/0.0/16_019/0000787. Skillful technical support from Ms. A. Flemming, Ms. C. Hochsmann and Ms. B. Macbac is gratefully acknowledged.

Supplementary Data

Supplementary data related to this article can be found at <https://doi.org/10.1016/j.jcpa.2018.05.004>.

References

- Anstee QM, Goldin RD (2006) Mouse models in non-alcoholic fatty liver disease and steatoc hepatitis research. *International Journal of Experimental Pathology*, **8** 7, 1-16.
- Arkadopoulos N, Dellerevos G, Nastos C, Papalois A, Kalimeris K *et al.* (2011) Development of a porcine model of post-hepatectomy liver failure. *Journal of Surgical Research*, **170**, e233-e242.
- Avritscher R, Wright KC, Javadi S, Udiemandul R, Gupta S *et al.* (2011) Development of a large animal model of cirrhosis and portal hypertension using hepatic transarterial embolization: a study in swine. *Journal of Vascular Medicine and Biologicals*, **22**, 1329-1334.
- Baus KPMD, Ludwig JMD (1995) Chronic hepatitis: an update on terminology and reporting. *Journal of Surgical Pathology*, **19**, 1409-1417.
- Bedossa P, Poynard T (1996) A algorithm for the grading of activity in chronic hepatitis C. *Hepatology*, **24**, 289-293.
- Besusparis J, Jokubauskiene S, Plancoulaine B, Herlin P, Laurinaviciene A *et al.* (2014) Quantification accuracy of liver fibrosis by in-vivo elastography and digital image analysis of liver biopsy histology. *Analytical Cell Pathology*, **2014**, e317635.
- Boykov Y, Jolly M-P (2000) Interactive organ segmentation using graph cuts. In: *Mathematical Image Computing and Computational Assisted Filtering - MICCAI 2000*, SL Delp, L Scou, AM DiGoia, BJarama:z, F. ds., Springer, Bertin, pp. 276-286.

- Bruha J, Vyciál O, Tonar Z, Mirka H, Haidingerová L *et al.* (2015) Monoclonal antibody against transforming growth factor beta 1 does not influence liver regeneration after resection in large animal experiments. *In Vivo*, 29, 327-340.
- Brum EM, Janney CG, DiBisceglie AM, Neuschwander-Tetri BA, Bacon BR (1999) Nonalcoholic liver disease: a proposal for grading and staging the histological lesions. *Annals of Gastroenterology*, 94, 2467-2474.
- Budai A, Fulop A, Hahn O, Onody P, Kovacs T *et al.* (2017) Animal models for association of liver portal and portal vein ligation for staged hepatectomy (ALPPS): achievements and future perspectives. *EuroJMN, Surgical & Cardiac*, 58, 140-157.
- Chen XL, Chen T-W, Zhang X-M, Li Z-L, Li H *et al.* (2013) Splenic magnetic resonance diffusion-weighted imaging for quantitative staging of hepatic fibrosis in miniature pigs: an initial study. *Hepatology & Surgery*, 43, 1231-1240.
- Chow S-C, Wang H, Shao J (2008) *Sampling Calculations in Clinical Research*. Ed. Chapman and Hall/CRC Biostatistics Series, Boca Raton, pp. 49-82.
- Croome KP, Mao SA, Glorioso JM, Krishna M, Nyberg SL *et al.* (2015) Characterization of a porcine model for associating liver partition and portal vein ligation for staged hepatectomy. *Journal of the International Hepato-Biliary Association*, 17, 1130-1136.
- de Vries EMG, Verheij J, Hubscher SG, Leeflang MMG, Boonstra K *et al.* (2015) Application of bile duct and prognostic value of fibrosis scoring systems in primary sclerosing cholangitis. *Journal of Hepatology*, 63, 1212-1219.
- Eberlova L, Liska V, Mirka H, Gregor T, Tonar Z *et al.* (2016) Porcine liver vascular bed in Biodur E20 corrosion casts. *Folia Morphologica*, 75, 151-161.
- Eberlova L, Liska V, Mirka H, Tonar Z, Haviar S *et al.* (2017) The use of porcine corrosion casts for liver histology, anatomy, and immunohistochemistry. *Annals of Anatomy*, 213, 69-77.
- Emerson M (2010) Refinement, reduction and replacement approaches to in-vivo cardiovascular research. *British Journal of Pharmacology*, 161, 749-754.
- Fakhoury-Sayegh N, Tarrak-Smayra V, Khazzaka A, Esseily F, Obeid Ott *et al.* (2015) Characterization of non-alcoholic fatty liver disease induced in wistar rats following four different diets. *Journal of the International Hepato-Biliary Association*, 9, 350-357.
- Forbes SJ, Parola M (2011) Liver fibrosis. *Best Practice & Research Clinical Gastroenterology*, 25, 207-217.
- George J, Pereira N, Phung N, Lederer C, Yun Hou J *et al.* (2003) Lipid peroxidation, superoxide production and hepatic fibrogenesis in a rat model of chronic steatohepatitis. *Journal of Hepatology*, 39, 756-764.
- Ghodszad A, Faby BN, Wadawczyk S, Liedlke S, Berjon JMG *et al.* (2012) Porcine liver application of human unrestricted somatic stem cells to support hepatic regeneration after portal embolization and tumor surgery. *ASAIO Journal*, 58, 255-261.
- Gnurrmann DM, Medel J, Schmilz A, Kohler K, Krone D *et al.* (2015) Evaluation of the plasma kinetic and parenchymal elution kinetics of two different irinotecan loaded drug-eluting embolies in a pig model. *Journal of Vascular and Interventional Radiology*, 26, 746-754.
- Gohlke F, Lohse AW, Dienes HP, Lohr H, Marker-Hermann E *et al.* (1996) Evidence for an overlap syndrome of autoimmune hepatitis and primary sclerosing cholangitis. *Journal of Hepatology*, 24, 699-705.
- Gunthersen HJG, Jensen EB (1987) Tissue efficiency of systematic sampling in stereology and its prediction. *Journal of Microscopy*, 147, 229-263.
- Hirschfield GM, Karsen TH, Lindor KD, Adams OH (2013) Primary sclerosing cholangitis. *Lancet*, 382, 1587-1599.
- Hosoyama V, Kurihara H, Sakai T (2000) Ultrasound-visual localization of sized elastic fibers in glisson's sheath of rat liver: implications for mechanical environment and possible production. *Journal of Anatomy*, 196, 327-340.
- Huug SV, Abdelsalam ME, Harmouch S, Ensor JE, Chellappa J (2014) Evaluation of liver fibrosis and hepatic venous pressure gradient with MR elastography in a novel swine model of cirrhosis. *Journal of Magnetic Resonance Imaging*, 39, 590-597.
- Huug V, Adams LA, Joseph J, Bulsara MK, Jeffrey GP (2017) The ability of Hepascore to predict liver fibrosis in chronic liver disease: a meta-analysis. *Liver International*, 37, 121-131.
- Ishak K, Balis LA, Bird L, Casazza F, De Groen C *et al.* (1995) Histological grading and staging of chronic hepatitis. *Journal of Hepatology*, 22, 696-699.
- Jirák M, Baroš M, Tomášek P, Malečková A, Kural T *et al.* (2018) Generalized low-dose image data for liver and calcium quantification of volumes, surfaces, lengths, and object counts in fibrous and porous materials using X-ray microtomography. *Materials*, 11, 551-568.
- Junaš KL, Tonar Z, Kubíková T, Liška V, Pálek R *et al.* (2017) Stereological analysis of size and density of hepatocytes in the porcine liver. *Journal of Anatomy*, 230, 575-588.
- Kawamura V, Ikeda K, Fukusuma T, Hara T, Hosaka T *et al.* (2014) Potential of a non-invasive pincer ablation procedure for small hepatocellular carcinoma using a multipolar radiofrequency ablation system: an experimental animal study. *Hepatology & Surgery*, 44, 1231-1240.
- Kisseleva T (2017) The origin of fibrogenic myofibroblasts in fibrotic liver. *Hepatology*, 65, 1039-1043.
- Kleiner DE, Brum EM, Vukobratović M, Behling C, Comos MJ *et al.* (2005) Design and validation of a histological scoring system for non-alcoholic fatty liver disease. *Hepatology*, 41, 1313-1321.
- Komine M, Kawasako K, Okamoto M, Matsuda K, Hirayama K *et al.* (2008) Histological distinction and evaluation of biliary ductal dilatation and biliary cysts in pig liver. *Journal of Comparative Pathology*, 139, 202-207.
- Kubíková T, Kočová P, Brázdil J, Špaňáková J, Burker J *et al.* (2017) The composition and biochemical properties of human cryopreserved aortas, pulmonary trunks, and aortic and pulmonary cusps. *Annals of Anatomy*, 212, 17-26.

- L<Oe YH, Ha V, Chae C (20 IO) Expression of interferoc - alpha and Mx protein in d,e tiversofpigsexperimentally infected wiú l swine hepatitis E virus. *Journal o/Compatative Patloú,gy*, **142**, 187- 192.
- Lee KS, Santagostino SF, Li D, Ramjit A, Serrano K *tt al.* (2017) Cadieter-directed intraponal detivery of endo,d,elial ceU therapy for tiver regeneration: a feasibility s111dy in a large ruúmal model of cirrhosis. *Raúú>Ú>!{J*, **285**, 114- 123 .
- Leflcowitd> JH (2007) Liver biopsy assessment in dironic hepatitis. *Ardtiw of Mtdi(JJf lusMrch*, **38** , 634-643.
- Lepreux S, Desmoutiere A (2015) Human tiver myofibroblasts during development and <lise.a.ses wiú l a focus on portal (myo)fibroblasts. *Frontitrs in Pl!}'wlogy*, **6**, 1- 8.
- Lindor KD, Gershwin ME, Poupon R, Kaplan f, Bergasa NV *et al.* (2009) Primary bitiary cirrhosis. *He atology*, **50** , 291- 308 .
- Lossi L, D' Angelo L, De Girolamo P, Merigliú A (2016) **Anatomic.al feawres for an adequate choi.ce of expedmentalaiúmal model in biomedicine: li. Smallllaboratory rodents, rabbit, and pig. *Anna/s oj Anato"!)'*, **204** , 11- 28 .**
- Lua I, Li V, PappoeLS, Asalúna K (2015) M yofibroblastic conversion and regeneration ofmesoú l elial cells in peritoneal and tiver fibrosis. *Anurimn Journal of Pat!toÚ>!{J*, **185**, 3258- 3273 .
- Mad,ado MV, Mid,elotri GA, Xie G, de Almeida TP, Boursier *Jet al.* (20 15) Mouse models of diet-induced non-alcoholic steatohepatitis reproduce ú le het.eregenuity of d,e human disease. *PLoS One*, **10**, eOI2799 1.
- Mak KM, Chen LL, Lee TF (2013) Codistribution of collagen type IV and laminin in liver fibrosis ofelderly cadavers: immunolústochemical marker of perisinusoidal basenlent membrane formation. *Anaf.úmi(, (JI &túrd*, **296**, 953- 964.
- Mak KM, Chu E, Lau KHV, Kwong AJ (2012) Liver fibrosis in elderlycadavers: locatization ofcoUagen types **I,111, and IV, cx-s moúútmusleacún, andelasLic fiber.s. *Anaum,i,..l&txird*, **295**, 1159- 1167.**
- Marcos R, Correia-Gomes C (2015) Liver,ru d gender:are ú tere differences in fibrous Lissue before Lhe onseL of fibrosis? *Htpavlogy*, **61**, 1093- 1094.
- Marcos R, Monteiro RAF, Rod,a E (2012) The use of design-based stereology to evaluate volumes ,ru d numbers in ú t liver: a review wiú t practicalguidelines. *Journal of Anawmy*, **220** , 303 - 3 17 .
- Mattfeklt T, MaU G, Gharehbaghi H, Miiller P (1990) E.ltimatiQn of \$urface area and,Ingt h wid, the o,ri:n ta-tor. *Journal of Miéroseopy*, **159** , 301-3 17 .
- Mouton PR (2011) *Unbiasd Sureo/ogy: A Contise Guide*. Johns HopkinsUniversity Press, Baltimore, pp. 55- 57.
- Miihlfeld C, Nyengaard J R, MayhewT M (2010) A review of state-of-the-art stereology lor beuer quantitative 3D morphology in cardiac research. *Ca,di.tnJa\$1.Ula, Patúology*, **19** , 65- 82 .
- Nowarcky J, Knorr A, Hirdi-Dietrich C, Siegting A, Volk H-D *et al.* (2013) Inactivated Orfvirus (Parapo"- virus ovis) elicits anú fibroú c act.iviLy in modeb ofliver fibrosis. *Hepatoú,gy Research*, **43** , 535- 546.
- Nygárd JE, Mortensen KE, Hedegaard J, Conley LN, Bendixen C *et al.* (2015) Iissue remodeUing following resecLion of porcine liver. *Bi.oMM & suuth lnU:rnati.onal*, **201 5**, 1- 10 .
- P ru,asevid, MR, Meers GM, Linden MA, Bood, FW, Perfield J W *et al.* (2018) High-fut, lúgh -fructose, lúgh - d, olesterolfeeding ca usesevere NASH and cecal microbiota dysbiosis injuve1ú le Ossabawswine. *Ametitan] ou,nal oj Physiúú,gy. &dot:rino/ogy and Metabolism*, **314** , e78- e92 .
- Peterson TC, Neumeister M (1996) Effect Qfpentoxifyltine in rat and swine models ofhepaticfibrosis: roleoffibroproliferatíon in its mechanism. *I m.nu nophar]llitology*, **31**, 183- 193.
- Sakhuja P (2014) Pathologyofalcoholic tiver disease, can it be ditrerentiated from nonalcoholic steatohepatíLis? *World Journal of Gastroenurology*, **20** , 16474 - 16479 .
- Saxena R (20 li) *Prattit:al Hpati, Patlto/ogy: A Diagnostil: A(>proach*. Saunders, Plúladelplúá, pp. 203- 213.
- Scheuer PJ (1991) Classificationofdironicviral hepatitis: a need lor reassessment. *Journal of Hepatúgy*, **13**, 372- 374.
- St ruid ish RA, Cholongitas E, Dlíllon A, Burroughs AK, Dlíllon AP (2006) An appraisal ofthehistopat hological assessment ofliver fibrosis. *Gut*, **55**, 569- 578.
- Stasi C, Milani S (2016) Non-invasive assessment of liver fibrosis: between prediction/prevenú on of outcomes ,rud cost-efectiveness. *World Journal of Gastroenuroú,gy*, **22** , 17 11 - 1720 .
- Takal,ashi V, Fukusato T (2014) Histopat hology of non-alcoholict fatty liverdisease/nonalcoholictsteatú epatitis. *World Journal of Gastroenurology*, **20** , 155 39 - 155 48.
- TI,eise ND (2013) Histopat, ologyofalcoliolict tiver disease. *Clini,..l Liver Disease*, **2** , 64 - 6 7.
- Tonar Z, Kubíková T, Prior C, Demjén E, Liška V *tt al.* (2015) Segmental and age differences in d,e elastin network, collagen, and smoot.h muscle phenotype in ú twnica media ofú teporcine aorta. *Anrals of Anawmy*, **201** , 79- 90.
- Vrtková I (2015) Genetic admixture analysis in Prestice black-piedpigs. *ArchivesojAnimalBr.t.ding*, **58**, 115- 121.
- Wang L, He F-L, Liu F-Q, Yue Z0 , Zhao H-W (2015) Establishment ofa hepatic cirrhosis and porta! hyper-tension model by hepatic arterial perfusion wiú t 80% alcohol. *World]ournal ofGastroenuroú,gy*, **21** , 95#- 955 3.
- Watson AL, Carlson DF, Largaespada DA, Hackett PB, Fahrenkrug SC (2016) Engineered \$winemodel\$ of cancer. *F ontiers inGmttia*, **7**, 78.
- Working Subgroup (Englishversi,oc) for Cli,úcal Practice Guidelines for Primary Biliary Cirrhosis (2014) **Guidelines for the management of primary biliary cirrhosis. *Htpato/ogy Research*, **44** , 71- 90 .**
- YangJO, Abdelmalek MF, Pang H, Guy CD, Smith AD *et al.* (2014) Gender and menopause impactseverity of fibrosis antongpatients wiú t non-alcoholic steatohepatiris. *Hepatoú,gy*, **59**, 1406- 1414.
- Yi X, SongM, Yuan V, ZhangX, Chen W *eta/.* (2012) Hepaticstimulator subsLance alleviates toxin-induced and

- immune-mediated liver injury and fibrosis in rats. *Digit - tWe Dis MS&S and St: itnteS*, 57, 2079- 2087.**
- Yin M, Glaser KJ, Manduca A, Mounajjed T, Mailû H (2017) Distinguishing between hepatic inflammation and fibrosis with magnetic resonance elastography. *Radú,logy*, **28 4**, 694 - 705 .
- Zaitoun AAM, Awad S, Ukabam S, Makadisi S, Record C (2001) Quantitative assessment of fibrosis and steatosis in liver biopsies from patients with chronic hepatitis C. *Journal of Clinical Pathology*, **54**, +61- +65.
- Zaitoun AAM, Mailû H A, Record CO (1998) Stereology and morphometry of steatosis in human alcoholic (ALD) and non-alcoholic liver disease (NALD). *Acta Stereology*, **17**, +9- 58.
- Zhang JJ, Meng XK, Dong C, Qiao JL, Zhang RF *et al.* (2009) Development of a new animal model of liver cirrhosis in swine. *F. umptan SurgitAl Rr.stitdt*, **42**, 35- 39.
- Zhang Z, Zhurig F, Lu Y, Zheng S (2015) Update on implication of angiogenesis in liver fibrosis. *Hepatology Resumh*, **45**, 162- 178.
- Zhao YL, Zhu R-T, Sun Y-L (2016) Epithelial-mesenchymal transition in liver fibrosis. *BWm.t.ditAl &port.s*, **4**, 269 - 27+.
- Zhou L, Chen T, Zhang X, Yang Z, Tang H *et al.* (201+) Liver dynamic contrast-enhanced MRI for staging liver fibrosis in a piglet model. *Journal of Magnetic & sonante Imaging*, **39**, 872- 878.

[/aewed, Mard, 11/1 2018

Atu pted, May 25/1, 2018

Příloha VII:

PÁLEK, R., V. LIŠKA, L. EBERLOVÁ, H. MÍRKA, M. SVOBODA, S. HAVIAR, M. EMINGR, O. BRZOŇ, P. MIK a V. TŘEŠKA, 2018. Experimental processing of corrosion casts of large animal organs. *Rozhledy V Chirurgii: Mesicnik Ceskoslovenske Chirurgicke Spolecnosti*. 97(5), 222–228. ISSN 0035-9351. Bez IF.

Experimentální příprava korozivních preparátů orgánů velkého zvířete

R. Pálek¹, V. Liška¹, L. Eberlová¹, H. Mírka¹, M. Svoboda¹, S. Havíř^{6,7}, M. Eminger¹, O. Brzoň¹, P. Mik¹, V. Třeška¹

¹ Chirurgická klinika, Univerzita Karlova, Lékařská fakulta v Plzni, Fakultní nemocnice Plzeň

² Biomedicínské centrum, Lékařská fakulta Univerzity Karlovy v Plzni

³ Ústav anatomie, Lékařská fakulta Univerzity Karlovy v Plzni

⁴ Klinika zobrazovacích metod, Lékařská fakulta Univerzity Karlovy v Plzni

⁵ Centrum nových technologií a materiálů, Západočeská univerzita v Plzni

⁶ Katedra fyziky, Fakulta aplikovaných věd, Západočeská univerzita v Plzni

⁷ Nové technologie pro informační společnost (NTIS), Fakulta aplikovaných věd, Západočeská univerzita v Plzni

So uhrn

Úvod: Korozivní preparáty (KP) slouží k vizualizaci a hodnocení morfologie dutých struktur. KPs naplněným kapilárním retikulem umožňují za pomoci zobrazovacích metod získat data použitelná pro matematické modelování orgánové perfuze. Náročnost přípravy KP stoupá s objemem cévního řečiště. Proto byly touto metodou doposud zkoumány zejména malé živočišné druhy. Cílem této studie bylo optimalizovat protokoly přípravy korozivních preparátů různých orgánů prasedy domácího, a to vzhledem k dostupnosti těchto orgánů a významu prasedy domácího v experimentální medicíně.

Metoda: Byly použity orgány oátra, slezina, ledviny a tenké střevo zdravého prasedy domácího. Celkem 10 prasedy (6 samic), plemeno preltické ternostrakaté hmotnost 35–45 kg. Orgány byly vypreparovány do systémového řečiště by aplikován heparin a následně byl cévní systém orgánů vypláchnut buď in situ (oátra), nebo po vyjmutí z těla zvířete do vody. Slezina, tenké střevo a heparinovaným fyziologickým roztokem. Veškerá manipulace vyjmutými orgány probíhala pod vodní hladinou za účelem prevence embolizace vzduchu do cévního řečiště. Dalším krokem byla intraarteriální (u jater i intraportální) aplikace pryskyřice Biodur E20 (Heidelberg, Německo). Po ztuhnutí pryskyřice byly odstraněny okolní tkáně pomocí 15% roztoku KOH a poté vylavěny vodou. Objem preparátů byl uchováván v 70% denaturovaném alkoholu menšími vylavěnými. Hotové KP byly zkoumány pomocí stereomikroskopu, běžné výpotetní tomografie (CT) mikro-cr. skenovací elektronové mikroskopie (SEM) nebo vysokorozlišovacího digitálního mikroskopu.

Výsledky: Díky odběru orgánů za specifických podmínek, použití vhodné pryskyřice i metodiky nástřiku se podařilo získat kvalitní KP jater, ledvin, sleziny a tenkého střeva prasedy domácího. Možnost barvení pryskyřice zlepšila makroskopickou přehlednost preparátů. Bylo provedeno skenování pomocí běžného CT, které se ukázalo jako vhodná metoda pro zkoumání preparátů jater. Mikro-CT a vysokorozlišovací digitální mikroskopie pak přinesly obrazy nejdrobnějších struktur retikule zkoumaných orgánů. I když se SEM pro kontrolu kvality odlišuje ještě stále jeví jako zastupitelná, zdá se, že může být částečně nahrazena vysokorozlišovacím digitálním mikroskopem. Mikro-CT umožnilo získat data o prostorovém uspořádání retikule a data pro budoucí softwarové modelování orgánové perfuze zkoumaných orgánů. Vysoká kvalita získaných preparátů umožnila jejich využití i v evyuce anatomie člověka.

Závěr: Podařilo se optimalizovat protokol přípravy KP jater, ledvin, sleziny a tenkého střeva prasedy domácího. S použitím různých zobrazovacích modalit mohou být tyto KP využity pro získání dat o prostorové architektuře cévního řečiště. Tato data mohou být využita pro optické matematických modelů orgánové perfuze využitelných například pro optimalizaci orgánových resekcí.

klíčová slova: korozivní preparáty - kapilární retikule - Biodur E20 - prasedy domácí - animální model

Summary

Experimental processing of corrosion casts of large animal organs

R. Palek, V. Liška, L. Eberlova, H. Mírka, M. Svoboda, S. Havíř, M. Eminger, O. Brzoň, P. Mik, V. Třeška

Introduction: Corrosion casts (CCs) are used for the visualization and assessment of hollow structures. CCs with filled capillaries enable (with the help of imaging methods) to obtain data for mathematical organ perfusion modelling. As the processing is more difficult in case of organs with greater volume of the vasculature, mainly organs from small animals have been cast up to now. The aim of this study was to optimize the protocol of corrosion casting of different organs of pig. Porcine organs are relatively easily accessible and frequently used in experimental medicine.

Method: Organs from 10 healthy Prestice Black-Pied pigs (6 females, body weight 35–45 kg), were used in this study (liver, spleen, kidneys and small intestine). The organs were dissected. Heparin was administered into the systemic circulation and then the vascular bed of the organs was flushed with heparinized saline either in situ (liver) or after their removal (spleen, kidney, small intestine). All handling was done under the water surface to prevent air embolization. The next step was an intraarterial (in case of the liver also intraportally) administration of Biodur E20 (Heidelberg, Germany) resin. After hardening of the resin in the organ tissue was dissolved by 15% KOH and the specimen was rinsed with tap water. Voluminous casts were stored in 70% denatured alcohol, the smaller ones were lyophilized. The casts were assessed with a stereomicroscope, computed and micro-computed tomography (CT and microCT), a scanning electron microscope (SEM) and high-resolution digital microscope (HROM).

Results: High-quality CCs of the porcine liver, kidneys, spleen and small intestine were created owing to the sophisticated organ harvesting, the suitable resin and casting procedure. Macroscopic clarity was improved thanks to the possibility of resin dyeing. Scanning by CT was performed and showed to be a suitable method for the liver cast examination. MicroCT, SEM and HROM produced images of the most detailed structures of vascular bed. Despite the fact that SEM seems to be an irreplaceable method for CCs quality control, it seems that this modality could be partly replaced by HROM. MicroCT enabled to obtain data about three-dimensional layout of the vascular bed and data format the-

mathematical modelling of organ perfusion. With regard to the quality of the CCs, they could also be used to teach human anatomy.

Conclusions: The protocol of the corrosion casting of the porcine liver, kidneys, spleen and small intestine CCs was optimized. Thanks to different imaging methods, the CCs can be used as a source of data on three-dimensional architecture of the vascular bed. These data can be used for mathematical modeling of organ perfusion which can be helpful for example for optimization of organ resections.

Key words: corrosion casts – microvasculature – Biodur E20® – domestic pig – animal model

Rozhl Chir 2018;97:222–228

ÚVOD

Korozivní preparáty (KP) slouží k vizualizaci a hodnocení morfologie dutých struktur. Jejich příprava spočívá ve vyplnění prostor polymerizující látkou a v následném odleptání okolních tkání. Vzniklý preparát je tedy odlitkem dutiny (lumina). Historie KP sahá až do středověku. Obvykle je za objevitele a průkopníka této metodiky považován Leonardo da Vinci, který na začátku 16. století vyplňoval hovězí mozkové komory a srdeční dutiny voskem, po jeho ztuhnutí však okolní tkáně odstraňoval mechanicky [1,2]. Nejednalo se tedy přímo o korozi (proces definovaný jako samovolné, postupné rozrušení hmoty vlivem chemické reakce s okolím), z tohoto hlediska je historie KP mnohem starší. V tzv. prekorozivním období např. již Alessandra Giliani (1307–1326), italská vědkyně a anatomka, jako první naplnila velké cévy lidského těla barevnou tvrdnoucí látkou, aby usnadnila jejich sledování. První skutečný korozivní preparát připravil nejspíš až holandský anatom Govert Bidloo (1649–1713), jenž naplnil dýchací cesty člověka roztaveným kovem a po jeho ztuhnutí odstranil okolní tkáň varem [3]. V následujících stolecích se anatomové snažili vylepšit jak aplikovaná média, tak techniku samotné aplikace nebo odstranění okolních tkání tak, aby získali co nejpřesnější odlitky zkoumaných struktur [4].

KP nacházejí své využití zejména při studiu cévního řečiště jednak normálních a jednak patologicky změněných orgánů [5]. Pro hodnocení cévního stromu je nutná dobrá náplň kapilárního řečiště [6].

Ke zkoumání KP jsou využívány různé zobrazovací techniky. V 70. letech minulého století byly publikovány první práce využívající skenovací elektronovou mikroskopii (SEM) pro diagnostiku různých struktur kapilárního řečiště [7]. Jeho dobrá náplň byla umožněna nově syntetizovanými akrylovými a epoxidovými pryskyřicemi. Pro zkoumání KP je poměrně nově využívána metoda mikroCT. Zdá se, že se zavedením vysokorozlišovací tomografie (mikroCT) prožívají KP opět svoji renesanci [8,9,10]. Ačkoli je SEM pro kontrolu kvality odlitků stále nezastupitelná, při použití RTG kontrastních pryskyřic nabízí mikroCT v kombinaci s využitím v klinické praxi běžně používaných softwarů zcela nové možnosti 3D zobrazení s rozlišením struktur na úrovni 2D histologických řezů [11]. CT skeny je však možné použít i pro potřeby modelování perfuze nebo kvantifikaci jednotlivých parametrů mikrocirkulačního řečiště (míra větvení, úhel odstupu cév atd.) [10,12]. Jako velmi nadějná zobrazovací technika se pro studium cévní morfologie založené na KP jeví i vysokorozlišovací digitální mikroskopy, které díky mobilnímu objektivu a pohybu v Z ose umožňují 3D rekonstrukce s možností zvětšení až 2000x, a to v rozli-

šení odpovídajícím možnostem SEM. Avšak na rozdíl od SEM můžeme s digitálním mikroskopem odečítat povrchové struktury do hloubky až 1 cm bez nutnosti řezání preparátu nebo následné fixace či pokovování vzorku. Digitální fotografie umožňují reálný barevný obraz, instalovaný software pak možnost 2D i 3D měření.

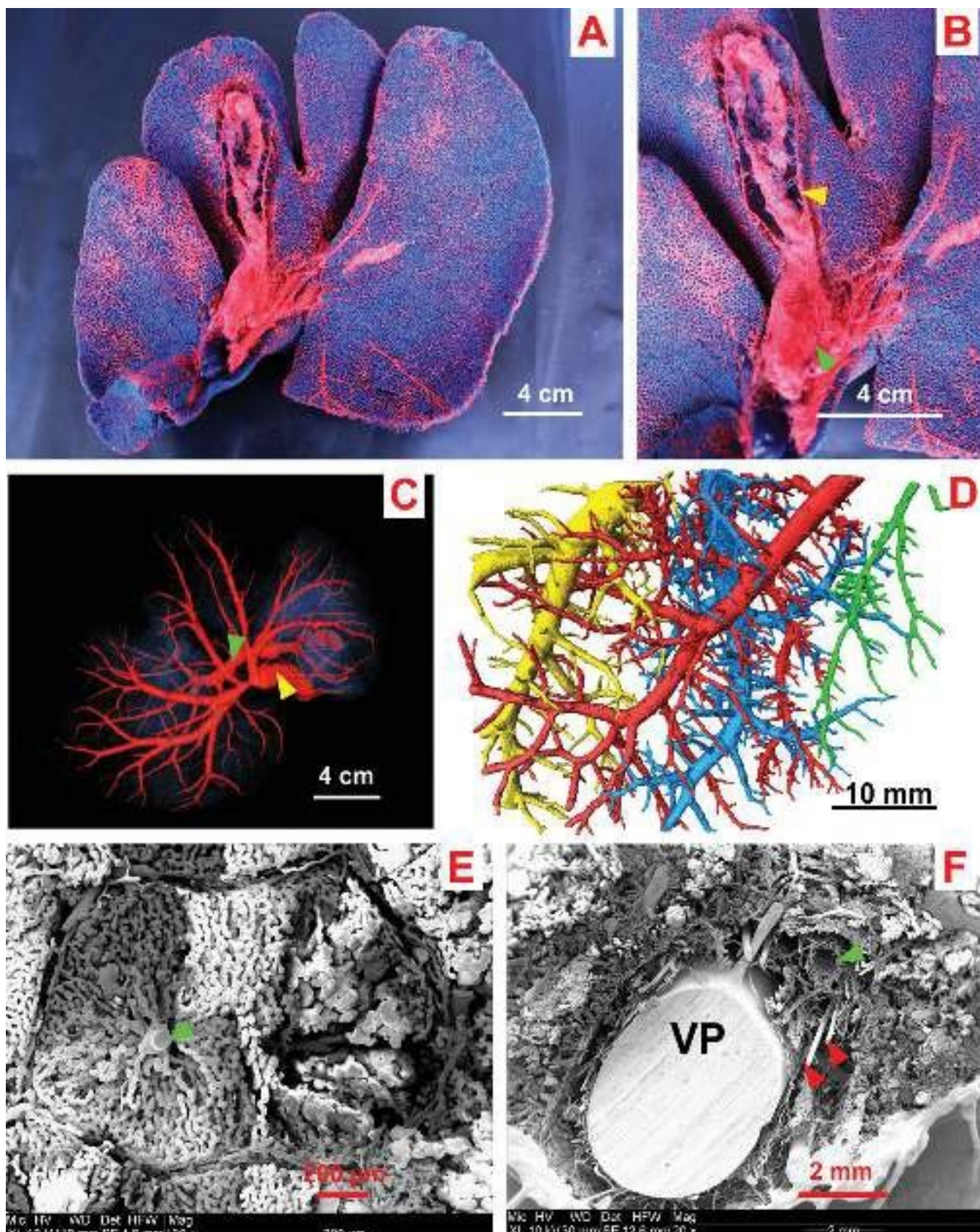
Pro dobrou náplň kapilárního řečiště je nutné odebrat orgán za specifických podmínek (systémová heparinizace, průplach řečiště izotonickým roztokem). Z toho důvodu jsou lidské orgány pro tento účel prakticky nedostupné. Výjimku tvoří jen orgány vyřazené z transplantace [8,13]. Cílem této studie bylo optimalizovat protokoly přípravy korozivních preparátů různých orgánů prasete domácího, a to vzhledem k dostupnosti těchto orgánů a významu prasete domácího v experimentální medicíně.

METODA

Studie byla provedena dle platné legislativy a s povolením Ministerstva zemědělství ČR. Byly dodrženy stávající předpisy a směrnice pro chov a experimentální využívání zvířat v souladu se zákonem č. 246/1992 upraveným vyhláškou č. 207/2004 s následným výkladem k vyhlášce č. 39/2009. Orgány byly získány z prasete domácího (plemeno přeštické černostrakaté prase), které je na Lékařské fakultě UK v Plzni využíváno jako animální model pro výzkumné účely [14,15,16,17]. Pracovalo se s 10 zdravými jedinci z jatečního chovu (6 samců, váha 35–45 kg).

Zvířata byla operována v celkové anestezii za použití mechanické ventilace. Orgány byly vypreparovány a ihned poté zvířeti aplikován heparin (100 IU/kg váhy). Následovalo propláchnutí cévního systému orgánu heparinovaným fyziologickým roztokem (5000 IU/1 l fyziologického roztoku). V případě jater byl proveden proplach *in situ* pomocí katétrů zavedených suprahepaticky do *vena cava caudalis* a do *arteria hepatica*. *Venaportae* zůstala volná pro odtok krve a fyziologického roztoku, infrahepatická část *vena cava caudalis* byla podvázána. V případě ostatních orgánů byl proplach proveden intraarteriálně po vynětí orgánu z těla zvířete. Žíly byly ponechány volné pro odtok. Obě ledviny byly ponechány jako jeden preparát a proplachování bylo provedeno intraaortálně s odtokem cestou *vena cava caudalis*. Po propláchnutí byly cévy vyjmutých orgánů zasvorkovány a orgány přeneseny a proplněny pryskyřicí pod vodní hladinou z důvodu prevence embolizace vzduchu do cévního řečiště.

Plnění cévního stromu pryskyřicí Biodur E20® (Heidelberg, Německo) bylo provedeno tepennou cestou (ledviny, slezina, střevo), u jater i cestou *vena portae*.



Obr. 1: Korozivní preparát cévního řečiště jater prasete domácího

A, B – Biodur E20® aplikován cestou *v. portae* (modrá) a cestou *a. hepatica* (červená); cévy žlučníku (žlutá šipka), *vasa vasorum v. portae* (zelená šipka). C – makroCT, VRT, syntopické zobrazení *v. portae* (zelená šipka) a *v. cava caudalis* (žlutá šipka). D – mikroCT, 3D rekonstrukce, preparát plněný pouze cestou *v. portae*. E – SEM, *lobulus venae centralis* (zelená šipka). F – SEM, preparát plněný cestou *vena portae* (VP) a *a. hepatica* (červené šipky); peribiliární arteriální pleteň (zelená šipka).

Fig. 1: Vascular corrosion cast of the domestic pig liver

A, B – Biodur E20® injected via the portal vein (blue arrow) and via the hepatic artery (red arrow); vessels of the gallbladder (yellow arrow), *vasa vasorum* of the portal vein (green arrow). C – macroCT, VRT, syntopic view of the portal (green arrow) and hepatic venous systems (yellow arrow). D – microCT, 3-D reconstruction, cast filled via the portal vein. E – SEM, liver lobule. Central vein (green arrow). F – SEM, cast fill via the portal vein (VP) and the hepatic artery (red arrows). Peribiliary plexus (green arrow).

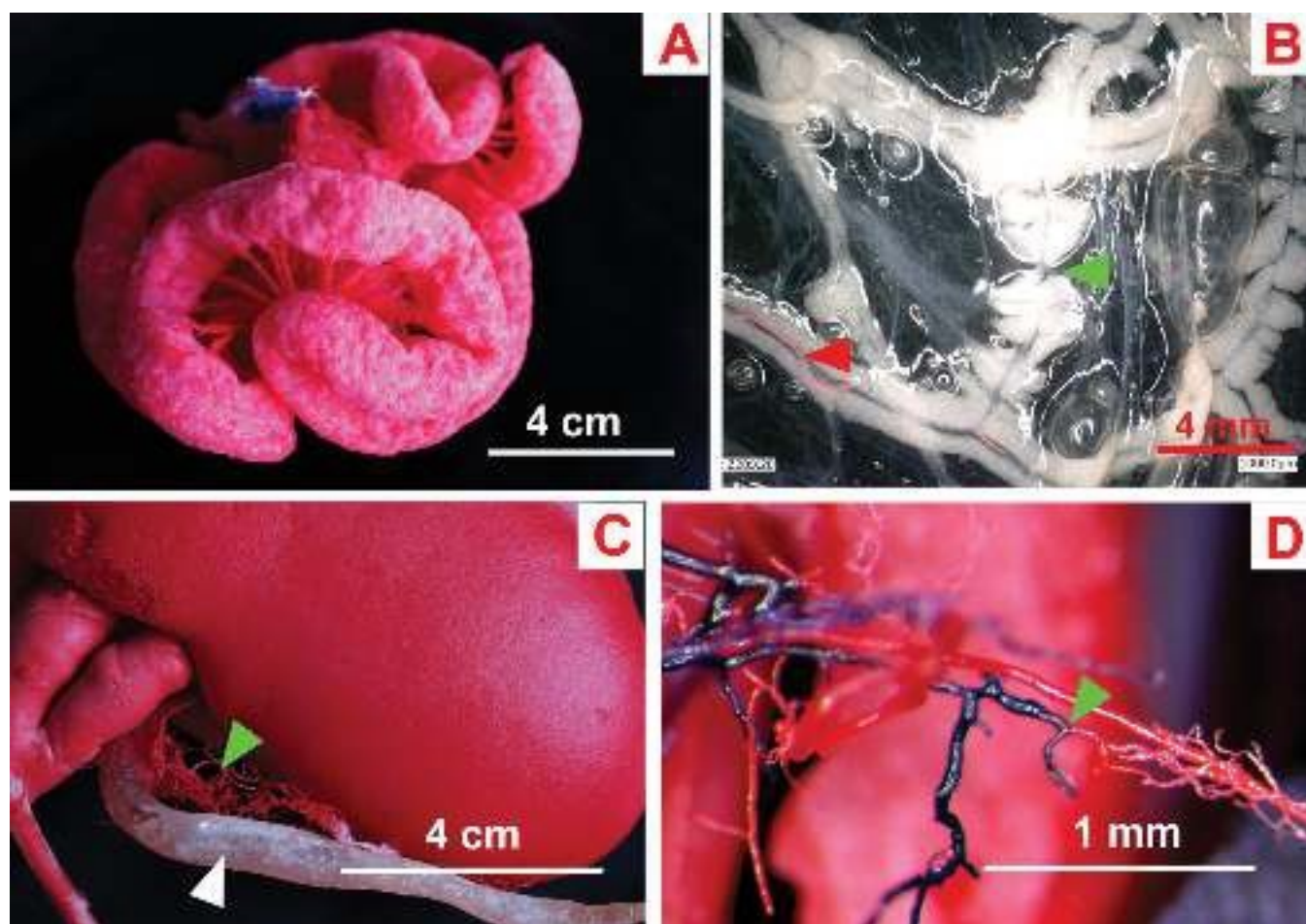
U některých preparátů jater byly navíc naplněny i žlučové cesty včetně žlučníku cestou *ductus choledochus*, v případě ledvin pak retrográdně močovod a ledvinová pánvička. Některé preparáty ledvin byly plněny jak cestou intraarteriální, tak intravenózní. Při aplikaci pryskyřice více cestami bylo vždy provedeno barvení pryskyřice k následnému usnadnění makroskopického rozlišení jednotlivých řečišť a struktur. Po aplikaci pryskyřice orgány zůstaly ve vodní lázni o pokojové teplotě. Po ukončení polymerizace pryskyřice (asi 24 hod.) byl orgán přemístěn do 15% roztoku KOH, jenž rozpustil organické tkáně. Hotové KP byly uchovány v 70% denaturovaném alkoholu, menší byly vysušeny mrazem.

Pro studium a ověření kvality hotových KP byly použity následující zobrazovací metody: pro přehledové vyšetření větších struktur běžné CT (Somatom Sensation 64, Siemens, Forchheim, Německo), pro detailnější zobrazení stereomikroskop (Olympus SZX7; Tokio, Japonsko), dále mikroCT (Xradia μ XCT 400, Pleasanton, CA, USA), SEM SU-70 (Hitachi, Japonsko) a digitální mikroskop Keyence VHX-6000 (Osaka, Japonsko). Při použití technik mikroCT, SEM a stereomikroskopu nelze vyšetřit preparáty velkých orgánů jako jeden celek. Preparáty tedy byly zamrazeny v destilované vodě a nařezány na pásové pile na menší díly o velikosti přibližně 1 cm³. Pro zkoumání

pomocí SEM bylo dále potřeba tyto nařezané kostky na 5 minut ponořit do 5% kyseliny mravenčí, opláchnout v destilované vodě, usušit na vzduchu a pokrýt zlatem. Až poté toto přípravě mohlo být provedeno vyšetření SEM.

VÝSLEDKY

Byla vypracována metodika přípravy KP různých orgánů prasete domácího (Obr. 1–3). Díky proplachu cévního řečiště orgánů při jejich odběru, prevenci vzduchové embolizace a díky použití pryskyřice s požadovanými vlastnostmi (přiměřená viskozita, dostatečný manipulační čas před ztuhnutím, nízká lámavost po ztuhnutí) se podařilo naplnit celé cévní řečiště včetně kapilár. Při aplikaci pryskyřice arteriální cestou došlo v případě ledvin, sleziny a střeva k naplnění celého řečiště skrz kapiláry až do žil. U jater došlo při aplikaci intraarteriální a intraportální k naplnění sinusoid a skrz *venae centrales* postupně *venae hepaticae* a *vena cava caudalis* (Obr. 1 A, B). Použitá pryskyřice Biodur E20 umožňuje zároveň zobrazení velkých struktur (vrátnicová žíla, jaterní tepny a žíly, ledvinové a slezinové tepny a žíly, žlučové cesty se žlučníkem) i mikrocirkulace (glomeruly, jaterní sinusoidy). Možnost barvení této

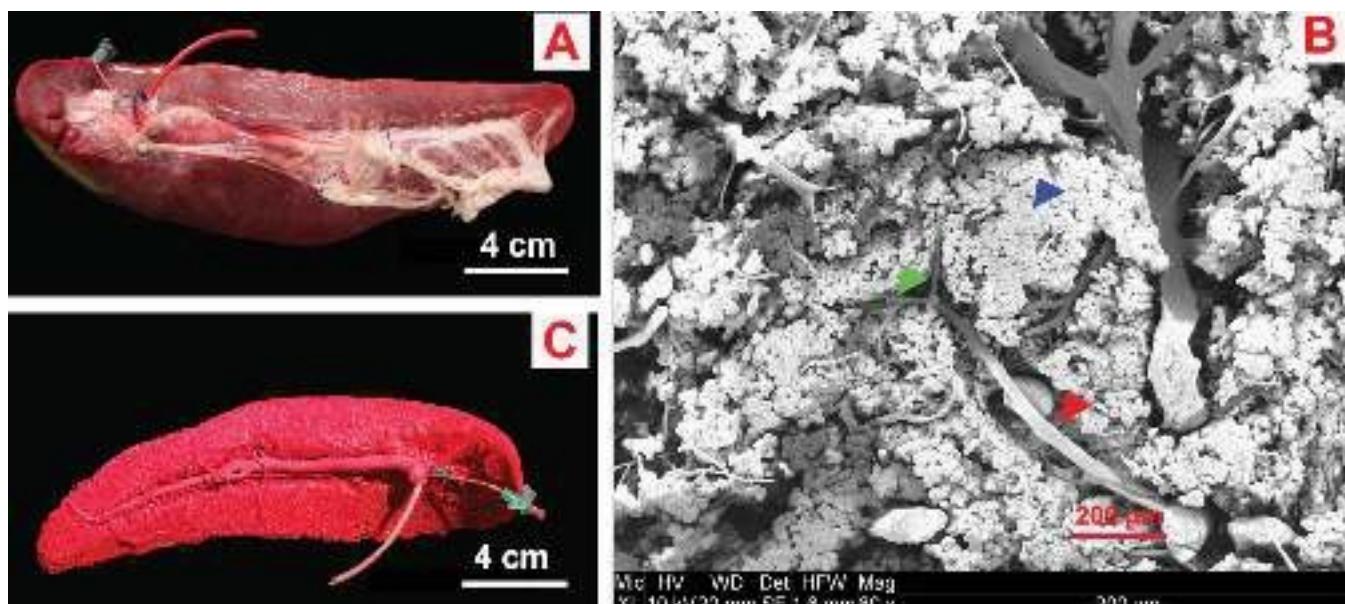


Obr. 2: Korozivní preparáty tenkého střeva (A, B) a ledviny (C, D) prasete domácího

Biodur E20® aplikován tepnou – A, B, C, tepnou a žilou – D. B – tepna mezenteria (červená šipka), mízní cévy (zelená šipka). C – přední stěna dolního pólu levé ledviny, *rami ureterici* (zelená šipka), močovod (bílá šipka). D – ledvina, arteriovenózní anastomóza.

Fig. 2: Vascular corrosion casts of the small intestine (A, B) and kidney (C, D), domestic pig

Biodur E20® injected only via artery – A, B, C, via artery and vein – D. B – artery of the mesentery (red arrow), lymphatic vessels (green arrow). C – anterior aspect of the lower pole, left kidney. Ureteric branches (green arrow), ureter (white arrow). D – kidney, arteriovenous anastomosis.



Obr. 3: Korozivní preparáty sleziny prasete domácího, použit Biodur E20®, plněno tepnou

A – preparát před korozí, C – po korozí. B – SEM; *a. centralis* (červená šipka), *a. penicillata* (zelená šipka), pryskyřice mimo cévní řečiště červené pulpy (modrá šipka).

Fig. 3: Vascular corrosion casts of the porcine spleen. Biodur E20®, artery filling

A – spleen before, C – after corrosion. B – SEM; central artery (red arrow), penicillate artery (green arrow), resin extravasation in the red pulp (blue arrow).

pryskyřice pak zlepšuje makroskopickou přehlednost připravovaných preparátů.

Díky dostatečné radioopacitě lze takto získané preparáty vyšetřovat pomocí CT. Běžné CT je však z důvodu velikosti orgánu a vyšetřovaných struktur použitelné pouze u jater (Obr. 1 C). Softwarové programy umožňují prostorové rekonstrukce větších cév a odlišení jednotlivých cévních řečišť. Autoři prezentují rekonstrukci pomocí *volume rendering technique (VRT) s partním řečištěm vena portae a vena cava caudalis* (Obr. 1 C). Díky běžnému CT mohou být vytipovány dobře naplněné části orgánů vhodné k detailnějšímu zobrazení. Podobně jako běžné CT, umožňuje i mikroCT provedení prostorových rekonstrukcí a měření včetně kvantifikací (Obr. 1 D) [10]. I přes technický pokrok se jeví SEM pro kontrolu kvality odlitku včetně diagnostiky různých oddílů cévního stromu jako nezastupitelná. Autoři představují obraz jaterního lalůčku včetně *vena centralis* a obraz peribiliární arteriální pleteně (Obr. 1 E, F). Na KP jater prasete je také demonstrována přítomnost pěti laloků na rozdíl od lidských jater (Obr. 1 A).

V případě tenkého střeva byly zobrazeny cévy mezenteria, došlo k naplnění cestou *a. mesenterica superior* a *arteriae rectae* až do mikrocirkulace vlastního střeva a dále pak k naplnění přes drobné žíly mezenteria do přítoků *vena mesenterica superior* (Obr. 2 A). Na preparátu střeva před samotnou korozí jsou patrné mizní cévy mezenteria (Obr. 2 B).

Dále autoři prezentují makroskopický obraz preparátu ledvin plněný jednak arteriální cestou a jednak skrz močovod. Patrné jsou cévy vyživující močovod (Obr. 2 C). Při plnění jak arteriálním, tak venózním řečištěm se podařilo zobrazit arteriovenózní anastomózu (Obr. 2 D).

V případě sleziny došlo také k naplnění mikrocirkulace, ovšem aplikovaná pryskyřice přestoupila do intersticia,

v němž vytvořila kvůli svým hydrofobním vlastnostem typické kulovité útvary, patrné na snímcích ze SEM (Obr. 3 B). Dále autoři představují makroskopický obraz celého preparátu sleziny před korozí a po ní (Obr. 3 A, C).

MikroCT umožnilo získání dat o prostorovém uspořádání mikrocirkulace a dat pro budoucí softwarové modelování orgánové perfuze zkoumaných orgánů. Vysoká kvalita získaných preparátů umožnila jejich využití i ve výuce anatomie člověka.

DISKUZE

Zhotovené preparáty umožnily demonstraci rozdílů mezi anatomii prasečích a lidských orgánů. Vzhledem k tomu, že byly použity orgány prasete pro studii s předpokládaným přesahem do lidské medicíny, je potřeba zmínit tyto odlišnosti mezi lidskými a prasečími orgány. Například játra prasete domácího mají makroskopicky obvykle pět laloků (*lobus lateralis dexter et sinister, lobus medialis dexter et sinister, lobus caudatus*). *Lobus quadratus* je variabilní. Cévní a žlučový strom je však lidským játrům bližší, utváří také osm segmentů, které jsou zhruba shodné s lidskými [18]. Játra prasete domácího jsou tak vhodným modelem pro nácvik chirurgických technik [19,20], studium regenerace [21,22] nebo pro matematické modelování [23]. Histologicky je u zdravých jater prasete popisováno vazivo ohraničující jednotlivé jaterní lalůčky, zatímco u člověka je toto vazivo patrné pouze za patologických stavů, jako jsou jaterní fibróza či cirhóza [24].

Ledviny prasete jsou podobné lidským svou velikostí, hmotností, počtem a stavbou nefronů včetně architektury mikrocirkulace [25,26]. Liší se však počtem segmentů. Zatímco lidské ledviny mají obvykle pět

segmentů, ledviny prasete mají pouze čtyři segmenty. *Arteria renalis* se u prasat větví před ledvinovou branikou na horní a dolní pólovou tepnu a poté na přední a zadní segmentové tepny [27].

Slezina prasete se liší svým tvarem od sleziny lidské. Je významně delší a užší, její mikrostruktura doposud nebyla detailně zkoumána.

Lidské orgány jsou také využívány pro přípravu cévních korozivních preparátů, v průběhu odběru je však řečiště již zpravidla vyplněno koaguly, a naplnění mikrocirkulace je tudíž obtížné [28,29], avšak ne nemožné [30], což může činit problémy zejména při pokusu o dokonalou náplň kapilár. Výjimku tvoří lidské orgány vyřazené z transplantace, jejichž řečiště je propláchnuto speciálními roztoky, a riziko trombotizace je tak eliminováno [8]. Získání takového orgánu je však možné jen ve výjimečných situacích. Je až zarážející, že u tak často používaného animálního modelu ještě chybějí základní morfologické údaje – např. množství vaziva v játrech zdravého prasete dosud nebylo kvantifikováno, ačkoli stupeň fibrotizace je klíčový pro hodnocení výsledku experimentu včetně jeho převodu do lidské medicíny [31].

U KP sleziny sice byla naplněna mikrocirkulace, ovšem došlo k extravazaci pryskyřice. Získané zobrazení mikrocirkulačního řečiště sleziny odpovídá otevřené cirkulaci, jež umožňuje přestup pryskyřice do intersticia. Tento nálezný je v souladu s prací Lametschwandtnera a kol. a ukazuje, že pro studium morfologie cévního řečiště sleziny prasete je nutné použití imunohistochemie nebo SEM z nativních vzorků [32].

Do budoucna je možné využití dat o cévním řečišti získaných pomocí KP a mikroCT k matematickému modelování perfuze jednotlivých orgánů. Tyto modely mohou mít význam například pro zkoumání vlivu izolované orgánové perfuze, ale i pro plánování a optimalizaci některých chirurgických výkonů, např. jaterních resekcí [33]. Pokud by bylo možné pomocí těchto perfuzních modelů predikovat jaterní regeneraci, mohla

by se zvýšit operabilita pacientů s jaterními malignitami. Nová zjištění mohou přinést i KP patologicky změněných orgánů. Již dnes je známo například využití KP jater pro výpočet smykového napětí na stěně vrátnicové žíly u myšího modelu portální hypertenze [34].

ZÁVĚR

Byla vypracována metodika přípravy KP různých orgánů prasete domácího. Za mimořádný úspěch lze označit optimalizaci protokolu pro přípravu KP jater prasete s ohledem na komplikované cévní řečiště a náročnost operačního protokolu. Předpokládáme možnost použití této metodiky i pro jiná velká zvířata včetně lidských jater. V této studii zhotovené preparáty mohou sloužit pro výuku anatomie a jejich výhoda spočívá v možnosti zkoumání postupně od makroskopických až po mikroskopické struktury v rámci jednoho preparátu. Je možné vytvořit trojrozměrné modely mikrocirkulace z dat získaných pomocí mikroCT. Získaná data o prostorovém uspořádání mikrocirkulačního řečiště pak mohou být přínosná pro matematické modely orgánové perfuze s významem pro chirurgické resekce a transplantační chirurgii.

Poděkování:

Tato studie byla podpořena programem UNCE/MED/006 „Centrum klinické a experimentální jaterní chirurgie“ Univerzity Karlovy, Národním programem udržitelnosti I (NPU I) č. LO1503 poskytovaným Ministerstvem školství, mládeže a tělovýchovy. Dále z prostředků Univerzity Karlovy v rámci Investičního programu 2016–18 a GAUK č. 1206417.

Konflikt zájmů

Autoři článku prohlašují, že nejsou v souvislosti se vznikem tohoto článku ve střetu zájmů a že tento článek nebyl publikován v žádném jiném časopise.

LITERATURA

- Hermiz DJ, O'Sullivan DJ, Lujan HL, et al. Constructivist learning of anatomy: gaining knowledge by creating anatomical casts. *Anat Sci Educ* 2011;4:98–104.
- De Sordi N, Bombardi C, Chiochetti R, et al. A new method of producing casts for anatomical studies. *Anat Sci Int* 2014;89:255–65.
- Davies A. The evolution of bronchial casts. *Med Hist* 1973;17:386–91.
- Haenssger K, Makanya AN, Djonov V. Casting materials and their application in research and teaching. *Microsc Microanal* 2014;20:493–513.
- Lametschwandtner A, Lametschwandtner U, Weiger T. Scanning electron microscopy of vascular corrosion casts – technique and applications: updated review. *Scanning Microsc* 1990;4:889–941.
- Aharinejad SH, Lametschwandtner A. *Microvascular corrosion casting in scanning electron microscopy*, first edition. Springer, Berlin-Heidelberg-Wien 1992.
- Murakami T. Application of the scanning electron microscope to the study of the fine distribution of the blood vessels. *Arch Histol Jpn* 1971;32:445–54.
- Debbaut C, Segers P, Cornillie P, et al. Analyzing the human liver vascular architecture by combining vascular corrosion casting and micro-CT scanning: a feasibility study. *J Anat* 2014;224:509–17.
- Pabst AM, Ackermann M, Wagner W, et al. Imaging angiogenesis: perspectives and opportunities in tumour research – a method display. *J Craniomaxillofac Surg* 2014;42:915–23.
- Jirik M, Tonar Z, Kralickova A, et al. Stereological quantification of microvessels using semiautomated evaluation of X-ray microtomography of hepatic vascular corrosion casts. *Int J Comput Assist Radiol Surg* 2016;11:1803–19.
- Eberlova L, Liska V, Mirka H, et al. Porcine liver vascular bed in Biodur E20 corrosion casts. *Folia Morphol* 2016;75:154–61.
- Debbaut C, Monbaliu DR, Segers P. Validation and calibration of an electrical analog model of human liver perfusion based on hypothermic machine perfusion experiments. *Int J Artif Organs* 2014;37:486–98.
- Peloso A, Petrosyan A, Da Sacco S, et al. Renal extracellular matrix scaffolds from discarded kidneys maintain glomerular morphometry and vascular resilience and retains critical growth factors. *Transplantation* 2015;99:1807–16.
- Vrtkova I. Genetic admixture analysis in Prestice Black-Pied pigs. *Arch Anim Breed* 2015;58:115–21.
- Bruha J, Vycital O, Tonar Z, et al. Monoclonal antibody against transforming growth factor Beta 1 does not influence liver regeneration after resection in large animal experiments. *In Vivo* 2015;29:327–40.
- Junatas KL, Tonar Z, Kubikova T, et al. Stereological analysis of size and density of hepatocytes in the porcine liver. *J Anat* 2017;230:575–88.
- Eberlova L, Liska V, Mirka H, et al. The use of porcine corrosion casts for teaching human anatomy. *Ann Anat* 2017;213:69–77.
- Couinaud C. Liver lobes and segments: notes on the anatomical architecture.

- re and surgery of the liver. *Presse Med* 1954;62:709–12.
19. Bedoya M, del Rio AM, Chiang J, et al. Microwave ablation energy delivery: influence of power pulsing on ablation results in an ex vivo and in vivo liver model. *Med Phys* 2014;41:123301.
 20. Okada N, Mizuta K, Oshima M, et al. A novel split liver protocol using the subnormothermic oxygenated circuit system in a porcine model of a marginal donor procedure. *Transplant Proc* 2015;47:419–26.
 21. Mortensen KE, Revhaug A, et al. Liver regeneration in surgical animal models - a historical perspective and clinical implications. *Eur Surg Res* 2011;46:1–18.
 22. Avritscher R, Abdelsalam ME, Javadi S, et al. Percutaneous intraportal application of adipose tissue-derived mesenchymal stem cells using a balloon occlusion catheter in a porcine model of liver fibrosis. *J Vasc Interv Radiol* 2013;24:1871–8.
 23. Fu YB, Chui CK. Modelling and simulation of porcine liver tissue indentation using finite element method and uniaxial stress-strain data. *J Biomech* 2014;47:2430–5.
 24. Besusparis J, Jokubauskiene S, Plancou-laine B, et al. Quantification accuracy of liver fibrosis by in vivo elastography and digital image analysis of liver biopsy histochemistry. *Anal Cell Pathol (Amst)* 2014. Available from: 10.1155/2014/317635.
 25. Rytand DA. The number and size of mammalian glomeruli as related to kidney and to body weight, with methods for their enumeration and measurement. *Am J Anat* 1938;62:507–20.
 26. Friis C. Postnatal development of the pig kidney: ultrastucure of the glomerulus and the proximal tubule. *J Anat* 1980;130(Pt 3):513–26.
 27. Evan AP, Connors BA, Lingeman JE, et al. Branching patterns of the renal artery of the pig. *Anat Rec* 1996;246:217–23.
 28. Rani N, Singh S, Dhar P, et al. Surgical importance of arterial segments of human kidneys: an angiography and corrosion cast study. *J Clin Diagn Res* 2014;8:1–3.
 29. Mazur M, Walocha K, Kuniewicz M, et al. Application of Duracryl plus for preparation of corrosion casts of venous coronary tree of human heart. *Folia Med Cracov* 2015;55:69–75.
 30. Bereza T, Tomaszewski KA, Lis GJ, et al. ‘Venous lakes’ – a corrosion cast scanning electron microscopy study of regular and myomatous human uterine blood vessels. *Folia Morphol (Warsz)* 2014;73:164–8.
 31. Avritscher R, Wright KC, Javadi S, et al. Development of a large animal model of cirrhosis and portal hypertension using hepatic transarterial embolization: a study in swine. *J Vasc Interv Radiol* 2011;22:1329–34.
 32. Lametschwandtner A, Radner C, Minnich B. Microvascularization of the spleen in larval and adult *Xenopus laevis*: Histomorphology and scanning electron microscopy of vascular corrosion casts. *J Morphol* 2016;277:1559–69.
 33. Svobodova M, Jirik M, Vcelak P, et al. Software LISA – virtual liver resection to accelerate and facilitate preoperative planning. *Rozhl Chir* 2016;94:485–90.
 34. Van Steenkiste C, Trachet B, Casteleyn C, et al. Vascular corrosion casting: analyzing wall shear stress in the portal vein and vascular abnormalities in portal hypertensive and cirrhotic rodents. *Lab Invest* 2010;90:1558–72.

MUDr. Richard Pálek
Chirurgická klinika, UK, LF v Plzni, FN Plzeň
alej Svobody 80
304 60 Plzeň
e-mail: palekr@fnplzen.cz